Structure, dynamics and phase behavior of concentrated electrolytes for applications in energy storage devices

Dissertation

zur Erlangung des akademischen Grades

DOCTOR RERUM NATURALIUM

(Dr. rer. nat.)

im Fach Physik

eingereicht an der

Mathematisch-Naturwissenschaftlichen Fakultät
der Humboldt-Universität zu Berlin

von

Herrn M.Sc. Chanbum Park

Gutachter: Prof. Dr. Joachim Dzubiella
Gutachter: Prof. Dr. Arnulf Latz
Gutachter: Prof. Dr. Philipp Adelhelm
Tag der Verteidigung: 14.10.2020

Präsident der Humboldt-Universität zu Berlin
Prof. Dr.-Ing. Dr. Sabine Kunst

Dekan der Mathematisch-Naturwissenschaftlichen Fakultät
Prof. Dr. Elmar Kulke

List of publications

This thesis (https://doi.org/10.18452/22389) contains work from the following original papers published in peer-reviewed journals:

(I) **Park, C.**, Kanduč, M., Chudoba, R., Ronneburg, A., Risse, S., Ballauff, M. and Dzubiella, J., "Molecular simulations of electrolyte structure and dynamics in lithium–sulfur battery solvents", *J. Power Sources*, 2018, **373**, pp. 70–78.[1]

(II) **Park, C.**, Ronneburg, A., Risse, S., Ballauff, M., Kanduč, M. and Dzubiella, J., "Structural and Transport Properties of Li/S Battery Electrolytes: Role of the Polysulfide Species", *The Journal of Physical Chemistry C*, 2019, **123** (16), pp. 10167–10177.[2]

(III) Dubouis, N., **Park, C.**, Deschamps, M., Abdelghani-Idrissi, S., Kanduč, M., Colin, A., Salanne, M., Dzubiella, J., Grimaud, A. and Rotenberg, B., "Chasing Aqueous Biphasic Systems from simple salts by exploring the LiTFSI/LiCl/H2O phase diagram", *ACS Central Science*, 2019, **5** (4), pp. 640–643.[3]

(IV) Coles, S. W., **Park, C.**, Nikam, R., Kanduč, M., Dzubiella, J. and Rotenberg, B., "Correlation Length in Concentrated Electrolytes: Insights from All-Atom Molecular Dynamics Simulations", *The Journal of Physical Chemistry B*, 2020, **124** (9), pp. 1778–1786.[4]

[1] Permission is not required.

[2] Reprinted with permission from *The Journal of Physical Chemistry C*, 2019, **123** (16), pp. 10167–10177, Copyright © (2019) American Chemical Society.

[3] Reprinted with permission from *ACS Central Science*, 2019, **5** (4), pp. 640–643, Copyright © (2019) American Chemical Society.

[4] Reprinted with permission from *The Journal of Physical Chemistry B*, 2020, **124** (9), pp. 1778–1786, Copyright © (2020) American Chemical Society.

Statement of author's contribution

Some parts of the thesis are contributed by other authors, as the thesis is based on joint works and collaborations. I hereby identify my and the other authors' contributions.

1. The entire research presented in this thesis and in publications (I), (II), (III) and (IV) have been conducted under the supervision of Prof. Dr. J. Dzubiella.

2. Chapter 3 of the thesis is based on publication (I). All simulations and figures were produced by myself. Experimental viscosity and conductivity measurements for system IVa in the work were conducted by A. Ronneburg and S. Risse. Molecular dynamics (MD) simulations were designed by M. Kanduč and J. Dzubiella. All authors contributed to writing the manuscript under the coordination of the corresponding authors.

3. Chapter 4 of the thesis is based on publication (II). All simulations and figures were produced by myself. MD simulations were designed by M. Kanduč and J. Dzubiella. Experimental density, viscosity and conductivity measurements were conducted by A. Ronneburg and S. Risse. All authors contributed to writing the manuscript under the coordination of the corresponding authors.

4. Chapter 5 of the thesis is based on publication (III). B. Rotenberg, J. Dzubiella, M. Kanduč and M. Salanne designed the MD simulations, which were performed and analyzed by myself. N. Dubouis and I produced the figures; all authors contributed to writing the manuscript under the coordination of the corresponding authors. N. Dubouis prepared the solutions, conducted the FTIR experiments, performed the electrochemical measurements and realized the phase diagram. A. Grimaud and N. Dubouis analyzed FTIR and electrochemical experimental results. S.A. Idrissi and N. Dubouis measured the viscosity and followed the evolution of the aqueous biphasic system by microscopy. These results were further analyzed by A. Colin. M. Deschamps conducted and analyzed NMR measurements.

5. Chapter 6 of the thesis is based on publication (IV). I carried out classical MD simulations for lithium bis(trifluoromethanesulfonyl)imide (LiTFSI) in 1,2-dimethoxyethane/1,3-dioxolane systems. Simulations of LiTFSI in aqueous systems were performed by S.

Coles, and R. Nikam carried out NaI and LiCl in aqueous systems. I and S. Coles conducted the analysis of the correlation length and the Einstein–Helfand relations. All co-authors have contributed to the discussion of the publication.

Abstract

Electrolytes can be found in numerous applications in daily life as well as in scientific research. The increases in demand for energy-storage systems, such as fuel cells, supercapacitors and batteries in which liquid electrolyte properties are critical for optimal function, draw critical attention to the physical and chemical properties of electrolytes. Those energy-storage devices contain intermediate or highly concentrated electrolytes where established theories, like the Debye-Hückel (DH) theory, are not applicable. Despite the efforts to describe the physical properties of intermediate or highly concentrated electrolytes, theoretical atomistic-level studies are still lacking.

This thesis is devoted to critically investigate the transport/structural properties and a phase behavior of concentrated liquid electrolytes and their application in energy-storage devices, using statistical mechanics and atomistic molecular dynamics (MD) simulations. Firstly, we investigate the structure-property relationship in concentrated electrolyte solutions in next-generation lithium-sulfur (Li/S) batteries, which have a high theoretical energy density of 2600 Wh kg^{-1} and an abundant supply of sulfur [1]. We construct an MD simulation model of representative state-of-the-art electrolyte systems for Li/S batteries constituted by different chain lengths of polysulfides, lithium bis(trifluoromethanesulfonyl)imide (LiTFSI) and $LiNO_3$ electrolytes in the mixtures of the organic solvents 1,2-dimethoxyethane and 1,3-dioxolane. We then investigate the conductivities, diffusion coefficients, solvation structures, and the clustering behavior of our system. We discuss how the transport properties are influenced by the structural properties, such as ionic pairing or clustering, and attempt to elucidate the intrinsic properties of polysulfides.

Secondly, phase separation may exist if the physio-chemical properties of liquid mixtures are very different. Recently, the coexistence phase of two aqueous solutions of different salts at high concentrations was found, called aqueous biphasic systems, which can have important implications for battery design and function. Their composition usually involves a concentrated inorganic salt and an ionic liquid. We explore a wide range of compositions at room temperature for highly concentrated aqueous electrolytes solutions that consist of LiCl and LiTFSI. Then, we attempt to answer the question of how "different" the components of the mixture in the aqueous solution should be for such a liquid-liquid phase separation to occur.

Lastly, charge screening is a fundamental phenomenon that governs the structure of liquid electrolytes in the bulk and at interfaces; therefore, it is critical for batteries and supercapacitors. From the DH theory, the screening length is expected to be extremely

small in highly concentrated electrolytes. Yet, recent experiments show unexpectedly high screening lengths in those. This intriguing phenomenon has prompted a new set of theoretical works. We investigate the screening lengths for various electrolytes from low to high concentrations. Our MD simulation results corroborate the general experimental trend of increasing decay length in high concentration electrolytes; however, the observed increase is significantly lower than that of experiments, albeit very similar to previous theoretical calculations of correlations in bulk electrolytes.

Zusammenfassung

Elektrolyte finden sich in zahlreichen Anwendungen im täglichen Leben sowie in der wissenschaftlichen Forschung wieder. Durch die steigende Nachfrage nach Energiespeichersystemen wie z.B. Brennstoffzellen, Superkondensatoren und Batterien, bei denen die Eigenschaften von flüssigen Elektrolyten für eine optimale Funktion entscheidend sind, wird die Erforschung der physikalischen und chemischen Eigenschaften von Elektrolyten immer wichtiger. Solche Energiespeicher enthalten mittel- bis hochkonzentrierte Elektrolyte, zu deren Beschreibung etablierte Theorien wie die Debye-Hückel (DH) Theorie nicht anwendbar sind. Bei allen Bemühungen, die physikalischen Eigenschaften solcher Elektrolyte theoretisch zu beschreiben, fehlt es noch sehr an theoretischen Studien auf atomarer Ebene.

Diese Arbeit widmet sich der Untersuchung der dynamischen und strukturellen Eigenschaften sowie des Phasenverhaltens konzentrierter flüssiger Elektrolyte und ihrer Anwendung in Energiespeichern mittels Methoden der statistischen Mechanik und mithilfe atomistischer Molekulardynamik (MD) Simulationen.

Zuerst untersuchen wir die Struktur-Eigenschafts-Beziehungen in konzentrierten Elektrolytlösungen wie sie in Lithium-Schwefel (Li/S) Batterien der nächsten Generation angewandt werden, die eine hohe theoretische Energiedichte von 2600 Wh/kg^{-1} aufweisen [1]. Wir erstellen hierfür ein MD Simulationsmodell repräsentativer state-of-the-art Elektrolyt-Systeme für Li/S-Batterien bestehend aus Polysulfiden, lithium bis(trifluoromethanesulfonyl)imide (LiTFSI) und $LiNO_3$ Elektrolyten mit jeweils unterschiedlichen Kettenlängen gemischt in organischen Lösungsmitteln aus 1,2-dimethoxyethane and 1,3-dioxolane. Anschließend untersuchen wir die Leitfähigkeiten, Diffusionskoeffizienten, Solvatationsstrukturen und das Clusterverhalten unserer Systeme. Wir diskutieren, wie die Transporteigenschaften durch die strukturellen Eigenschaften wie Ionenpaarung oder Clusterbildung beeinflusst werden, und versuchen, die intrinsischen Eigenschaften von Polysulfiden aufzuklären.

Als Zweites befassen wir uns mit der Phasenseparation, die auftritt, wenn sich die physikalisch-chemischen Eigenschaften flüssiger Gemische voneinander unterscheiden. Kürzlich wurden die Koexistenzphasen zweier wässriger Lösungen mit unterschiedlichen hochkonzentrierten Salzen gefunden, die als wässrige Zwei-Phasen-Systeme bezeichnet werden, was wichtige Auswirkungen auf das Design und die Funktion von Batterien haben könnte. Diese Systeme bestehen üblicherweise aus einem konzentrierten anorganischen Salz und einer ionischen Flüssigkeit. In dieser Arbeit untersuchen wir eine Vielfalt von hochkonzentrierten wässrigen Elektrolytlösungen, die aus unterschiedlichen Zusammensetzungen von LiCl und LiTFSI bestehen. Daraufhin beantworten wir die Frage, wie unterschiedlich die Komponenten in der wässrigen Lösung gemischt sein sollten, damit eine solche flüssig-flüssig-Phasentrennung stattfinden kann.

Als letztes untersuchen wir die Ladungsabschirmung, die ein grundlegendes Phänomen ist, das die Struktur von Elektrolyten im Bulk und an Grenzflächen bestimmt. Daher ist sie für Batterien und Superkondensatoren von entscheidender Bedeutung. Aus der

DH Theorie wird erwartet, dass die Abschirmlänge in hochkonzentrierten Elektrolyten extrem klein ist. Neuere Experimente zeigen jedoch ein unerwartetes Verhalten bei zunehmenden Abschirmlängen. Dieses faszinierende Phänomen hat zu vielen neuen theoretischen Arbeiten geführt. Wir haben in dieser Arbeit die Abschirmlängen für verschiedene Elektrolyte von niedrigen bis zu hohen Konzentrationen untersucht. Unsere MD Simulationsergebnisse bestätigen den allgemeinen experimentellen Trend einer zunehmenden Zerfallslänge in hochkonzentrierten Elektrolyten. Der berechnete Anstieg wird durch ein universelles Potenzgesetz der gleichen Form beschrieben wie es auch experimentell beobachtet wird. Der von uns berechnete Exponent ist jedoch niedriger als der experimentelle Wert, obwohl er sehr ähnlich zu den Ergebnissen aus früheren theoretischen Berechnungen von Korrelationen in Bulk Elektrolyten ist.

Contents

1 Introduction

The demand for high-performing batteries is expected to grow exponentially with more electric vehicles and renewable energy generation, such as wind and solar power [2]. The availability of low-cost, safe, and long-lasting batteries will secure sustainable and off-grid energy supplies and reduce the burning of fossil fuels. Currently, lithium-ion batteries are commonly used owing to their high capacity and cycle performance [3]. However, the practical energy density of lithium-ion batteries is approaching the theoretical energy density. In addition, there is an issue with the supply of the raw materials used in manufacturing of lithium-ion batteries, such as cobalt [4, 5].

To improve the current battery performance or develop a next-generation battery, an accurate model will give a deeper insight into its fundamental mechanisms. It will enable the interpretation of experimental data and find the critical process impacting the battery cycle. Yet, many batteries undergo complex chemical reactions at interfaces, volume expansion, ion/electron transport, and phase separation [6, 7, 8]. Namely, physical changes and chemical reactions in batteries includes the different length and time scales. Therefore, a multi-scale perspective might aid in a rational design of batteries.

Traditional continuum-level battery models employ the porous electrode theory [9]. These models apply the concepts of volume-averaged values in porous materials, namely porosity, average surface area per volume, and conductivity, where the electrolyte is usually assumed to be a diluted solution. This model describes ion distribution, fluxes and electrical currents in a battery cell. This framework has been used to model various electrochemistry devices, such as lithium-ion [10, 11, 12] and metal-air batteries [13], and fuel cells [14], playing a vital role in battery design, in particular. As the concentration increases, however, the structure and transport properties of liquid electrolytes may undergo more dramatic changes than a simple correction to a mean-field picture [15, 16, 17, 18, 19]. In practice, intermediate and highly concentrated electrolytes, as well as multivalent ions, are being actively investigated in battery research and de-

velopment nowadays [20, 21, 22, 23]. The inclusion of relevant multiple interactions, such as ion-solvent and ion-ion interactions and the shape of ions, is vital for accurate modeling of these batteries [19], but, for instance, steric and electrostatic correlations are not easily obtained experimentally and incorporated into a mean-field theory [24, 25, 26].

In this thesis, we employ atomistic molecular dynamics (MD) simulations to examine the transport/structural properties and the phase behavior of liquid electrolyte solutions that are currently used in energy-storage devices. In the first part, we investigate the transport/structural properties of a lithium-sulfur (Li/S) battery electrolyte, which is a promising next-generation battery devices. A major challenge inherent to Li/S batteries is the polysulfides (PS) shuttle effect [27, 28], originating from the migration of PS from the cathode materials toward the anode. On the molecular level, these issues originate from the structural and solubility behaviors of the intermediate PS species in the bulk and in the electrode confinement. Yet, a comprehensive understanding of the solvation phenomena and dynamical properties of PS is limited, such as the solvation structure of Li^+, ion-ion/ion-solvent interactions, and diffusion processes of ions. Thus, we develop an efficient and accurate force field for MD simulations and describe the static and transport properties of the Li/S battery electrolytes.

The interactions of ions and solvents in intermediate and highly concentrated solutions determine the properties of the liquid state. Ions can be dispersed, aggregated, or chemically/physically bound to each other, or they can precipitate out of the liquid [29]. The ionic correlations can drive a strong attraction between the ions and induce phase separation [30]. Recent observations of aqueous biphasic systems (ABS) formed from the concentrated mixtures of inorganic salts and ionic liquids [31, 32, 33] raise a fundamental question of how different the components of such mixtures should be for a liquid–liquid phase separation to occur. Therefore, we investigate the phase behavior of highly concentrated aqueous electrolyte solutions that consist of LiCl and lithium bis(trifluoromethanesulfonyl)imide (LiTFSI). We analyze the coexistence diagram, the mechanism driving the phase separation, arising from the different anion sizes and present possible applications for a dual-ion battery.

Lastly, charge screening is a fundamental phenomenon that governs the structure of liquid electrolytes in the bulk and at interfaces [34]. It, therefore, plays a crucial role in electrochemistry and phase stability. An essential interaction between ions immersed in a continuum solvent is already well described by the Debye-Hückel (DH) theory. The charge-charge correlations are characterized by the Debye screening length λ_{D},

$$\lambda_{\mathrm{D}} = \left(\frac{\varepsilon k_{\mathrm{B}} T}{\sum_{j=1}^{N} \rho_j q_j^2} \right)^{1/2} \tag{1.1}$$

with k_B the Boltzmann constant, T the temperature, ε the permittivity, and the sum runs over the charged species with number density ρ_j and charge q_j. The screening length is expected to be extremely small in highly concentrated electrolytes. However, recent surface force experiments reported increasing screening lengths with ion concentration in ionic liquids and simple salts [35, 36]. This phenomenon is counter-intuitive according to classical liquid theories. In contrast to diluted electrolytes, the description of concentrated electrolytes has not been explored in detail. Therefore, we explore how the screening length beyond the DH regime can be changed through analysis with atomistic simulations.

In the following, a brief introduction about Li/S batteries is presented, followed by the main results and discussion.

1.1 Lithium sulfur batteries

Lithium–ion batteries are the most common battery type today and used in various applications, such as portable devices, electric vehicles, stationary energy-storage systems, etc. Research on and the engineering of lithium/sodium-ion batteries continue to significantly improve the batteries' cycle life and practical energy density [27, 15, 37, 38]. However, the practical energy density is approaching its theoretical limits, which is about 100 $\sim$ 280 mAh g^{-1} [39].

An increasing demand for rechargeable batteries and the need for batteries manufactured from sustainable raw materials are pushing the development for rechargeable and environmental friendly batteries.

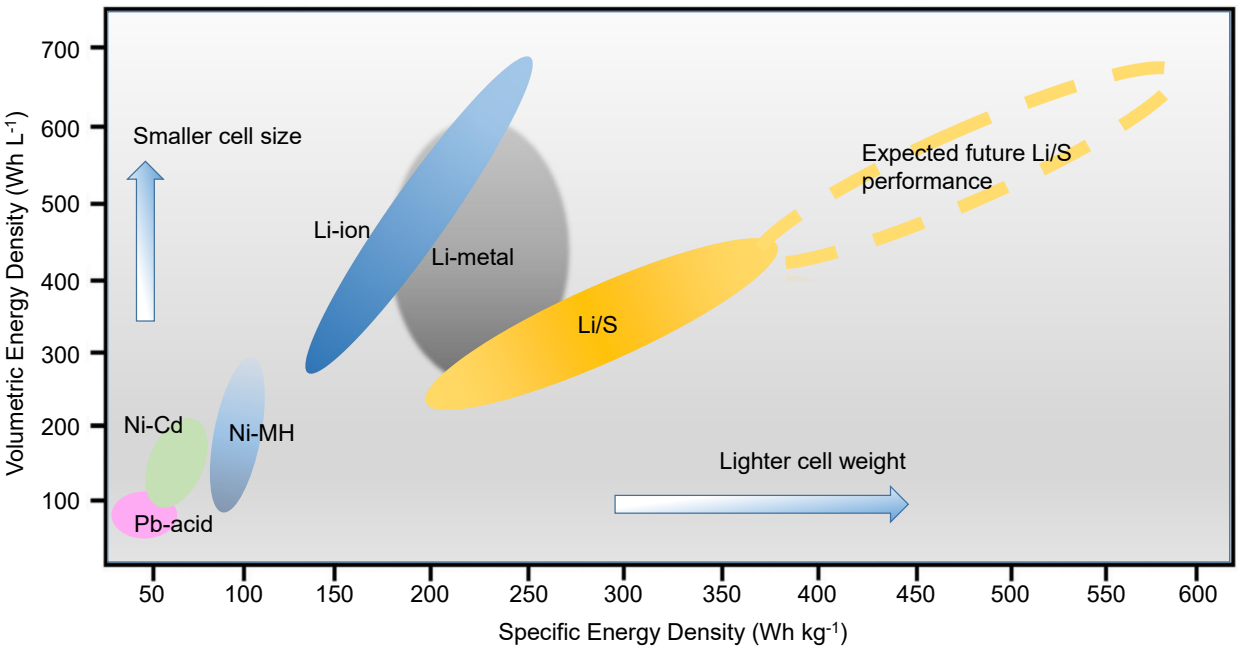

Figure 1.1: Ragone plot as a function of specific and volumetric energy densities (Information is obtained from Ref. [40]).

Li/S batteries are considered a promising next-generation battery chemistry due to their energy density of 2600 Wh kg^{-1} [1]. In addition, sulfur as a cathode material has many benefits, such as abundance, non-toxicity and low cost [41, 42].

The first Li/S system for energy storage was reported in 1962 [43]. In the late '60s

to ‘70s, high-temperature Li/S and Na/S batteries were investigated [44, 45, 46]. It was found that those high-operating temperature batteries suffer from significant corrosion problems, which are not yet solved [47]. Organic solvents, such as propylene carbonate, dimethyl sulfoxide and dimethylformalide were applied in 1968 [48]. Dioxolane based electrolytes were introduced in the late ‘80s. Electrolyte with dioxolane have conductivity one order of magnitude higher than tetrahydrofuran(THF)-toluene electrolytes [49, 50].

The structure of a Li/S battery is similar to that of lithium-ion batteries. A typical Li/S battery consists of an anode, separator, electrolyte, cathode, binder and current collector. Lithium metal is used as the anode and various polymer materials are used as the separator, like porous polypropylene. Organic solvents, such 1,2-dimethoxyethane (DME) and 1,3-dioxolane (DOL), are typical solvents for electrolytes [51]. Different types of lithium salts can be added to the electrolytes. The cathode consists of an electronically conducting host, such as porous carbon materials, metal sulfides, conducting polymers, etc. One common preparation method for a sulfur cathode with carbon materials is impregnating elemental sulfur into the porous carbon at a high temperature (∼115 °C). During discharge, Li^+ is oxidized from the anode and diffuses toward the cathode through the separator and the electrolytes, while electrons are traveling from the anode to the cathode via the external circuit.

Table 1.1: Proposed discharge mechanism with XRD experiments by Canas *et al.* [52]

$S_8(s) \longleftrightarrow S_8(l)$	solid/liquid
$2Li + S_8(l) \longleftrightarrow {S_8}^{2-} + 2\ Li^+$	liquid
$2Li + 3/4{S_8}^{2-} \longleftrightarrow {S_6}^{2-} + 2\ Li^+$	liquid
$2Li + 2/3{S_6}^{2-} \longleftrightarrow {S_4}^{2-} + 2\ Li^+$	liquid
$2Li + {S_4}^{2-} \longleftrightarrow 2{S_2}^{2-} + 2\ Li^+$	liquid/solid
$2Li + 1/2{S_2}^{2-} \longleftrightarrow S^{2-} + 2\ Li^+$	liquid/solid
$2Li + S^{2-} \longleftrightarrow Li_2S(s)$	solid

The subsequent chemical reaction from elemental sulfur to Li_2S experiences multiple

steps during the disproportionation of PS. One proposed discharge mechanism of sulfur from S_8 to Li_2S is shown in Table 1.1 [52]. The discharge/charge mechanism is complex and is still a subject of debate [27]. Generally, a crown-like S_8 ring is initially reduced with Li^+, forming highly soluble intermediate PS, Li_2S_x ($4 \leq x \leq 8$), the high plateau around 2.4 V in the discharge curve is characterized by the reduction of long PS Li_2S_x ($x = 8$ or 6) (also see Fig 1.2). At the low plateau *ca.* 2.1 V, the intermediate chain disproportionation occurs. At the final stage, around *ca.* 2.0 V, Li_2S and Li_2S_2 are formed and precipitation of those two species develops.

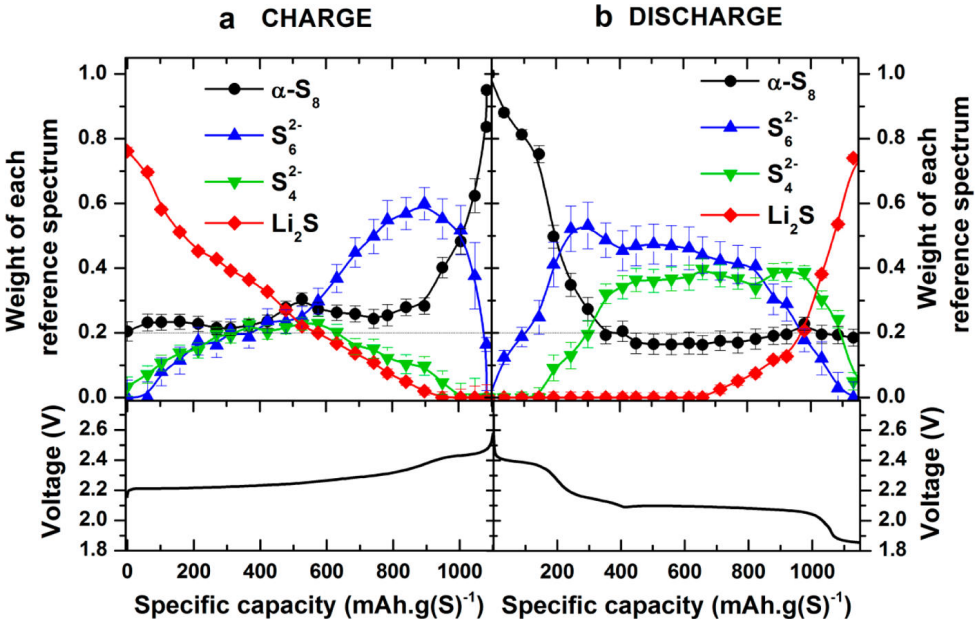

Figure 1.2: Evolution of sulfur k-edge XANES upon electrochemical cycling based on linear combination analysis at C/10. Reprinted with permission [53]. Copyright 2013 American Chemical Society.

The challenges to develop high-performing Li/S batteries are a short cycle life, high self-discharge, electrolyte/lithium metal depositions, heating at the end of the charge, the expansion and shrinkage of the cathode electrode and the PS shuttle effect [54]. On the anode side, the lithium metal anode tends to react with the electrolyte, lithium salts and PS, forming a solid-electrolyte interface (SEI) layer. This SEI layer can be beneficial for blocking the chemical reactions between a lithium metal electrode and PS; yet, the SEI layer can evolve or is degraded during cycling, generating active sites to stimulate dendrite growth [55]. Sulfur S_8, Li_2S_2 and Li_2S are insoluble in liquid electrolytes, while the intermediate PS (Li_2S_x, $4 \leq x \leq 8$) are highly soluble. The

intermediate PS species migrate and chemically react with the anode, forming an irreversible and insulating solid phase on the metallic lithium surface. This phenomenon in Li/S batteries is called the PS shuttle effect. It is known that the PS shuttle is considered to be one of major underlying phenomenon causing the short cycle life, self-discharge and heating [41].

In order to address this issue, various solutions, such as a heterogeneous doping on graphene, metal oxide/polymer matrix for a cathode materials and modification of separators have been suggested. One popular material for cathodes is carbon. Carbon is a good conductor and micro and meso structures can be obtained via different synthesis routes. Various types of carbon are used in Li/S batteries, such as graphene, carbon nanofibers, carbon nanotubes, conductive carbon black and graphene–CNT hybrid composites [56, 57, 58, 59, 60]. Those materials have been exploited to encapsulate PS physically, such as confining sulfur into mesoporous carbon or into hallow carbon nanofibers [56, 57, 58, 61]. Xu *et al.* [58] used micro porous carbon to encapsulate short-chain sulfur species. They showed that it prevents penetration of the solvent into the micro pores. The PS shuttle effect was suppressed and it gave almost 100% coulombic efficiency over 4200 cycles. A microporous–mesoporous hierarchical carbon composite also has the advantage that it can confine sulfur and has a large volume to hold more sulfur. At the same time, high electronic and ionic transference are facilitated [61, 62].

Graphene oxide or a nitrogen-doped graphene composite have been fabricated to trap sulfur into a cathode [63, 64]. Oxygen or nitrogen atoms on graphene serve as a binder with PS. Manganese dioxide nanosheets are reported to be a good binder for sulfur molecules [65]. Polymer electrodes are also synthesized to hold PS via chemical bondings [66, 67, 68]. Yet, many of these attempts negatively influence energy or power density or are not sufficient in practical use [41].

Nano-sized metal oxides are also used as a cathode material in Li/S batteries. It provides a high specific surface area and strong adsorption sites for PS. The metal oxides participate in a discharge–charge reaction within a certain voltage range [42]. TiO_2 [69], SnO_2 [70], V_2O_5 [71], Mxene nanosheets [72], $LiFePO_4$ [73], and MnO_2 [74]

are used as the metal oxide materials.

Sulfurized-conductive polymers also have many benefits, such as, improved electrical conductivity, stable structure and suppressed dissolution of PS. Conductive polymers that have been studied in Li/S batteries are poly(3,4-ethylenedioxy- thiophene) (PEDOT) [75], polyaniline nanotubes (PANINT) [66], polyacrylonitrile (PAN) [76], polyaniline (PANi) [77], polythiophene (PTh) [78], and polypyrrole (PPy) [79].

Besides the cathode materials, research on separators is also being carried out to reduce the shuttle effect. An ion-selective membrane [80], a PS doped polyethylene oxide-based gel membrane [81], or a size- and ion-selective membrane with intrinsic micro-porosity [82] have been suggested. Recent developments on solid-state polymer electrolytes offer a new strategy to suppress the PS shuttle effect [83].

Theoretically, Mikhaylik and Akridge [84] first proposed a cell model in 2004 with a continuum approach. They focused on the PS shuttle effect and related this with charge-discharge efficiency, discharge capacity and self-heating. Yet, this model could not explain the influence of electrolyte concentrations, viscosity, PS mobility on the shuttle effect. In 2008, White *et al.* [85] developed a more sophisticated model. They adapted the porous electrode theory pioneered by John Newman and collaborators [9] to include the porosity of the electrode and separator. The model employed the Nernst-Planck equation to describe the self-diffusion and migration of multiple species. They assumed that the electrolyte is dilute. The model can calculate the volume fraction of precipitate during the discharge, thereby the porosity of the cathode varies with the volume of the precipitation. Bessler *et al.* [86, 87] described the shuttle effect as the migration of S_8^{2-} from the cathode to the anode, at the same time, S_4^{2-} toward the anode. The diffusion of two species causes the "infinite charging" behavior with a low-rate charge. They also captured capacity fading during cycling caused by the loss of active materials and the decrease of the active surface area on the anode during cycling. Danner *et al.* [88] introduced a detailed 1+1D continuum model of sulfur/carbon composite cathodes. With the model, they explained that the difficulty of trapping sulfur in the cathode is induced by the concentration gradient between dilute bulk electrolyte and highly concentrated particles in the cathode. Marinescu

et al. suggested a zero dimensional model [89]. This model includes the PS shuttle, electrochemical reactions and precipitation or dissolution of Li_2S. The model is able to capture important features of the discharge and charge voltage curves. Furthermore, a multi-scale description of the composite C/S cathode model [90], model incorporating the effects of the Li_2S particle sizes [91, 92], equivalent circuit network model [93], meso-scale models [94, 95] have been suggested.

At an atomistic level, density functional theory (DFT) calculations suggested that [96] PS chains in the electrolyte agglomerate with Li^+ into clusters, such as $(Li_2S_x)_n$ (with $x = 4, \ldots, 8$ and $n \geq 1$). The clusters of Li_2S_4 are regarded as the last PS intermediates before the formation of Li_2S_2/Li_2S insoluble aggregates during the discharge process [97]. Classical MD simulations by Rajput *et al*. [98] reported that introducing $TFSI^-$ ions, which compete with PS for Li^+, weakens the PS – Li^+ clustering networks, resulting in a higher solubility of PS. However, the diffusion coefficients in that study differ from those measured by the pulse-field gradient nuclear magnetic resonance (PFG-NMR) methods by more than one order of magnitude [98].

Meanwhile, atomistic level studies [99, 98, 97] imply the difficulty of modeling Li/S battery solutions because of highly complex, multi-component PS solutions. Therefore, efficient and sufficiently accurate MD simulations are thus in urgent need to answer elusive questions, such as how Li^+ interacts with PS chains with different length, how the reaction mechanism pathway can be altered by choices of solvents and ions that affect the stability of the intermediate PS species, solubility, and morphologies of Li_2S_2/ Li_2S, the effect of the ionic correlation on diffusion of ions or ionic conductivity, the role of lithium salt, etc. Hence, it is thus of utmost importance to develop an efficient and sufficiently accurate MD simulation model, which can shed light on a deeper understanding at the atomistic level into the structural and transport properties. In addition, those detailed transport parameters of the electrolytes can underpin the future development of continuum models.

1.2 Thesis outline

In chapter 2, we begin with an introduction about the fundamental theories used in this work, namely, principles of MD simulations, the electronic continuum correction (ECC) model and analysis with statistical physics approaches.

After that, in chapter 3, we present an atomistic MD simulation model of representative state-of-the-art electrolyte-solvent systems used in metal-sulfur or metal-air batteries that constituted LiTFSI and $LiNO_3$ electrolytes in mixtures of the organic solvents DME and DOL [20]. This chapter includes a benchmark study by comparing structural and dynamic features with various available experimental reference systems. With that, we demonstrate their applicability for a wide range of electrolyte–solvent compositions.

In chapter 4, we incorporate PS of different chain lengths into our atomistic model developed above. The strong correlations and complex of PS make use of the conventional force fields difficult. We present the development of a working model for Li/S solutions, which includes Li_2S_4, Li_2S_6 and Li_2S_8 in applied electrolyte solutions of LiTFSI in DME and DOL mixtures. We examine the intrinsic properties of the PS and attempt to elucidate the structure-property relation in Li/S battery electrolytes.

In chapter 5, using a combination of experimental techniques and molecular simulations, we investigate the liquid-liquid phase separation in ABSs, which consist of aqueous liquid phases of LiTFSI and LiCl salt. We show the coexistence diagram and the mechanism driving the phase separation in ABSs, arising from the different anion sizes. With the understanding and control of ABS, we propose new avenues for aqueous-based battery systems.

In chapter 6, we study the correlation length in highly concentrated electrolytes, for instance, from simple salts in aqueous electrolytes to complex but real battery electrolytes. We compare the screening lengths evaluated from MD simulations and theoretical predictions as well as experimental values.

Lastly, we conclude this thesis with a summary and outlook in chapter 7.

2 Basic principles and methods

2.1 Molecular dynamics simulations

The atomistic behavior of liquids, solids, and dense gases can be simulated by atomistic MD simulations as well as a Monte Carlo method. MD simulations in this thesis were simulated with the GROMACS molecular dynamics simulation package (version 5.1.4) [100]. The governing dynamics are briefly described below.

2.1.1 Equation of motion

The dynamics of atom i inside a simulation box with mass m_i is given by solving Newton's equations of motion with finite difference method [100],

$$m_i \ddot{\mathbf{r}}_i = \mathbf{F}_i, \tag{2.1}$$

where $\mathbf{r}_i$ is the position of atom i. The forces $\mathbf{F}_i$ on atom i, are usually derived from a potential energy $\mathcal{U}$

$$\mathbf{F}_i = -\frac{\mathrm{d}\mathcal{U}}{\mathrm{d}\mathbf{r}_i}. \tag{2.2}$$

The potential energy consists of non-bonded and bonded interactions:

$$\begin{aligned}\mathcal{U} = &\sum_i \sum_j \left\{ 4\varepsilon_{ij} \left[\left(\frac{\sigma_{ij}}{r_{ij}} \right)^{12} - \left(\frac{\sigma_{ij}}{r_{ij}} \right)^{6} \right] + \frac{1}{4\pi\varepsilon_0\varepsilon_r} \frac{q_i q_j}{r_{ij}} \right\} \\ &+ \frac{1}{2} \sum_{\text{bonds}} K^b \left(r - r_{\text{eq}} \right)^2 + \frac{1}{2} \sum_{\text{angles}} K^\theta \left(\theta - \theta_{\text{eq}} \right)^2 \\ &+ \sum_{\text{dihedrals}} \left\{ \frac{K_1^\phi}{2} \Big[1 + \cos\left(\phi\right) \Big] + \frac{K_2^\phi}{2} \Big[1 - \cos\left(2\phi\right) \Big] + \frac{K_3^\phi}{2} \Big[1 + \cos\left(3\phi\right) \Big] \right\}.\end{aligned} \tag{2.3}$$

The non-bonded interactions are described by Lennard-Jones (LJ), the first term on the right-hand side (RHS) in Eq 2.3, and the Coulomb potentials, the second term on

the RHS in Eq 2.3. In general, the interaction can be of any form, but, in our case, it is assumed to be pairwise additive. σ and ϵ in the LJ parameters represent the van der Waals radius and the potential well depth, respectively. q_i, q_j, ϵ_0 and ϵ_r are the partial charges of atom i and j, vacuum permittivity, and relative permittivity, respectively.

To describe the non-bonded interactions between different species, i and j, geometric averages are used for σ_{ij} and ϵ_{ij}:

$$\begin{aligned} \sigma_{ij} &= (\sigma_{ii}\sigma_{jj})^{1/2} \\ \epsilon_{ij} &= (\epsilon_{ii}\epsilon_{jj})^{1/2}. \end{aligned} \tag{2.4}$$

The bonded potentials employ harmonic potentials to demonstrate the intramolecular bond and angular interactions, the third and fourth terms on the RHS in Eq 2.3, respectively. The bond stretching between the covalent bond i and j are described by a harmonic potential with a force constant K^b. The bond-angle vibrations between i, j, and k are also described by a harmonic potential with a force constant K^θ on the angle θ. The dihedral interaction is a fourth-body 1–4 interaction, demonstrated by the coefficients in Fourier series $K^\phi_{1,2 \text{ and } 3}$, and the dihedral angle ϕ, which represents the angle between the ijk and the jkl planes. The total torsional energy is the sum of each dihedral angle ϕ_{ijkl}.

Periodic boundary conditions were employed to mimic the bulk and macroscopic properties of the system and eliminate surfaces from simulations. For efficient computation purpose, the interactions are truncated at a separation $r_c \leq \frac{1}{2}L$ where r_c is the cut-off radius and L is the length of the simulation box. When a truncation sphere is employed in MD simulations, the interaction greater than r_c is ignored. This method is not suitable when the interaction forces are long ranged, such as ionic systems. Coulombic interactions in ionic systems can be treated with the Ewald summation [101, 102], in which an infinite lattice sum is carried out for long-ranged and slowly convergent interactions in the Fourier space.

In practice, the initial potentials and forces are computed with a set of initial positions and velocities (optional) of all atoms. The forces include the non-bonded and bonded interactions. Restraining or external forces are taken into account if it exists.

With the forces (Eq. 2.2), the positions and velocities are advanced by solving Eq. 2.1 numerically.

2.1.2 The leapfrog integrator

In order to advance MD simulation, Newton's equations of motion, Eq. 2.1 is integrated with the leapfrog integrator to update positions and velocities of all atoms [103]. Forces $\mathbf{F}_i(t)$ are computed as $\mathbf{F}_i = -\frac{\partial \mathcal{U}}{\partial r_i}$ including bonded/non-bonded interactions and restrains or external forces (if those are applied). The positions and velocities for the next time step, $t + \Delta t$ are computed as

$$\mathbf{v}_i\left(t + \frac{1}{2}\Delta t\right) = \mathbf{v}_i\left(t - \frac{1}{2}\Delta t\right) + \frac{\Delta t}{m_i}\mathbf{F}_i(t) \tag{2.5}$$

$$\mathbf{r}_i(t + \Delta t) = \mathbf{r}_i(t) + \Delta t \cdot \mathbf{v}_i\left(t + \frac{1}{2}\Delta t\right), \tag{2.6}$$

where $\mathbf{v}_i\left(t - \frac{1}{2}\Delta t\right)$ is the velocity at the previous time step. The new velocity and the position at time $t + \Delta t$ is also updated with the velocity at the previous time step and the current force and position.

2.1.3 Advanced simulation techniques

2.1.3.1 Constant temperature simulations

Direct implementation of MD equations described above produces the NVE ensemble (constant number, volume and energy). So as to control the temperature of a system, Berendsen [104], Andersen [105], Nosè-Hoover [106, 107] or a velocity rescaling [108] scheme can be coupled with the system.

The Berendsen algorithm is weakly coupled to an external heat bath with the target temperature T_0,

$$\frac{\mathrm{d}T}{\mathrm{d}t} = \frac{T_0 - T}{\tau}, \tag{2.7}$$

where T and τ are the temperature of the system and a time constant, respectively. The difference between T_0 and T decays exponentially with τ. Hence, the Berendsen thermostat relaxes the system with the target temperature quickly. It is a suitable algorithm for equilibrium. Yet, the Berendsen thermostat restrains the fluctuations of the kinetic energy; thus, the ensemble average will be not appropriate.

The velocity rescaling thermostat is similar to the Berendsen thermostat, but the velocity rescaling thermostat multiplies velocities every step by a factor of $\lambda = \sqrt{\frac{T_0}{T}}$. The velocity rescaling thermostat has an additional stochastic term that ensures a correct kinetic energy distribution. Therefore, this thermostat generates a correct canonical ensemble.

Nosè–Hoover temperature coupling also produces a correct canonical ensemble and it includes an extended thermal reservoir and a friction term in the equation of motion of particles in Hamiltonian. Equation 2.1 is modified as

$$\frac{\mathrm{d}^2\mathbf{r}_i}{\mathrm{d}t^2} = \frac{\mathbf{F}_i}{m_i} - \frac{p_\xi}{Q}\frac{\mathrm{d}\mathbf{r}_i}{\mathrm{d}t}, \tag{2.8}$$

where Q is the coupling constant to a heat bath and p_ξ is the equation of motion of the heat bath. The equation of motion for the heat bath parameter ξ is related to the target temperature T_0 as

$$\frac{\mathrm{d}p_\xi}{\mathrm{d}t} = (T - T_0). \tag{2.9}$$

Unlike the Berendsen thermostat, the Nosè–Hoover thermostat relaxes the system in a oscillatory way which means that the relaxation for the system to reach equilibrium requires 4 to 5 times greater than the Berendsen thermostat. Thus, in practice, the Nosè–Hoover thermostat is implemented after the system is relaxed with a weak coupling thermostat.

2.1.3.2 Constant pressure simulations

In a similar manner to the Berendsen thermostat, the Berendsen pressure [104] coupling algorithm couples the system with a first-order kinetic relaxation of the pressure as

$$\frac{d\mathbf{P}}{\mathrm{d}t} = \frac{\mathbf{P}_0 - \mathbf{P}}{\tau_p}, \tag{2.10}$$

where τ_p is a pressure time constant. The coordinates and box vectors are rescaled every step with a matrix μ

$$\mu_{ij} = \delta_{ij} - \frac{n_{\mathrm{PC}}\Delta t}{3\tau_p}\beta_{ij}(\mathbf{P}_{0ij} - \mathbf{P}_{ij}(t)), \tag{2.11}$$

where β is the isothermal compressibility of the system and n_{PC} is the coupling step.

The Berendsen pressure coupling (which is a weak pressure coupling) does not generate the true NPT ensemble. In principle, the Parrinello-Rahman pressure coupling [109] produces the correct NPT ensemble with the matrix equation of motion

$$\frac{\mathrm{d}\mathbf{b}^2}{\mathrm{d}t^2} = V\mathbf{W}^{-1}\mathrm{b}'^{-1}(\mathbf{P} - \mathbf{P}_{\mathrm{ref}}), \tag{2.12}$$

where V is the volume of the box, $\mathbf{P}$ and $\mathbf{P}_{\mathrm{ref}}$ are the matrices of the current and reference pressure, respectively. $\mathbf{W}$ is a matrix parameter that defines the strength of the coupling,

$$\left(\mathbf{W}^{-1}\right)_{ij} = \frac{4\pi^2\beta_{ij}}{3\tau_p^2 L}, \tag{2.13}$$

Similar to the Nosè-Hover coupling, the equation of motion for atoms are coupled with the Parrinello-Rahman modification,

$$\frac{\mathrm{d}^2\mathbf{r}_i}{\mathrm{d}t^2} = \frac{\mathbf{F}_i}{m_i} - \mathcal{M}\frac{\mathrm{d}\mathbf{r}_i}{\mathrm{d}t}, \tag{2.14}$$

$$\mathcal{M} = \mathbf{b}^{-1}\left(\mathbf{b}\frac{\mathrm{d}\mathbf{b}'}{\mathrm{d}t} + \frac{\mathrm{d}\mathbf{b}}{\mathrm{d}t}\mathbf{b}'\right)\mathbf{b}'^{-1}. \tag{2.15}$$

In addition, the pressure time constant τ_p is not equivalent to the relaxation time in the Berendsen pressure coupling algorithm. It is usual that the pressure time constant

for the Parrinello-Rahman coupling is 4 to 5 times greater than that of the Berendsen pressure coupling.

2.2 Electronic continuum correction

After the MD method was developed in the late '50s [110], MD simulations have been improved significantly and become an integral tool in physics, physical chemistry, biology, etc. Nowadays, MD simulations are performed on the nanosecond to the millisecond time scale and include more than a million atoms [111]. The governing dynamics of MD simulations rely on the empirical potentials, namely, force fields. Widely used force fields are, AMBER [112], CHARMM [113], GROMOS [114] and OPLS [115]. These force fields are employed to calculate forces and energies based on configurations. The electrostatic interactions in those classical force fields are modeled as fixed partial charges of atoms, usually centered on atoms. In this case, those force fields are categorized as nonpolarizable models [116]. Despite this simple treatment for the partial charges, the nonpolarizable models successfully produce reasonable results [117].

However, it is known that those simple nonpolarizable force fields give inaccurate ion–electrolytes, ion–ion interactions, pK_a or solvation free energies in some systems where electronic polarizability effects are non-trivial [118, 119, 120, 116, 116], for instance low or nonpolar solvents (ethers or alkanes) [121, 122], the interior of a biological membrane or low dielectric protein environment [123]. The solution to avoid those problems related with the fixed charges, is polarizable force fields in which the electron density is redistributed in response to variations in the local electric field [124, 125, 126, 127, 128, 129, 130].

A trade-off for accuracy with polarizable force fields is to compute self-consistently the polarization at each polarization site every simulation step. This limits the simulation time scale for polarizable force fields and it would be critical for some systems where sufficient sampling is important [131]. The consistent solutions for balancing intra- vs. intermolecular polarizations are still under development [132, 131]. For the reason, the simplest classical Drude oscillator model is not easily applicable for many systems, such as energy-storage solutions or biological systems [126, 127, 128, 130, 129].

It is without question that computationally efficient and simple nonpolarizable force fields are preferred as long as those force fields produce adequate results. Likewise,

there are many attempts to incorporate polarization effects into nonpolarizable force fields. Gee *et al.* and Weerasinghe *et al.* [133, 134] modified the ϵ in the LJ parameters to reproduce the experimental Kirkwood–Buff integrals. It is claimed that this approach, which roughly takes polarization into account, increases the cation–water interaction. Similarly, Fyta and Netz [135] reported that the drawback of nonpolarizable force fields can be compensated by the rescaling of the cation-anion LJ interactions. They showed that a modification of LJ interactions reproduces reduced ion clustering solution activities, which are comparable with experimental data. Despite the modification of LJ parameters corrects the polarization effects implicitly, it requires a substantial number of simulations to optimize force field parameters and the optimized parameters might be valid for the target systems [136]. Moreover, in low polar media, those strategies of LJ parameter optimization do not reproduce adequate physical properties, such as enthalpies of solvation, density, and heat of vaporization. Alternatively, Leontyev and Stuchebrukhov proposed ECC theory in which the partial charges are rescaled by the high-frequency (electronic) dielectric constant. This model describes a system as point charges are moving in an electronic continuum which screens the point charges as a result of polarization. The underlying concept is following. With the assumption of the linear response theory, the electronic polarization can be pictured as the response of electrons of the medium molecules. Hence, the total polarization of the medium can be contributed by an external field and the configurations of the medium molecules. The velocity of electrons is much faster than that of nuclei, they can configure themselves spontaneously as the nuclei changes configuration in the response to the external field. In other words, the total polarization is contributed from "inertial" polarization, which originates in the configuration of nuclei atoms and "inertialess" polarization, which is based on the fast electronic motion [137]. The terms "inertial" and "inertialless" are originated from the non-equilibrium solvation theory [137]. Hence, the electronic polarization by the medium molecules screens the ions in the system, the effective ion-ion and ion-solvent interactions in nonpolarizable force fields are corrected by rescaling the partial charges of ions with a high-frequency dielectric constant.

For example, the Coulomb interaction between two ions in water is screened by the

dipole fluctuations of water molecules (water dielectric permittivity) and the electronic contribution (high-frequency permittivity). In order to realize the screening effect from the electric contribution in nonpolarizable force fields, the formal charge can be rescaled by $1/\epsilon_{\text{el}}$ where ϵ_{el} is the high frequency dielectric constant (related to the refractive index as n^2) of the solvent. Then, the rescaled charge constitutes the Hamiltonian corresponding to the polarizable force field. The section below, we recall ECC model proposed by Leontyev and Stuchebrukhov [137, 131].

2.2.1 From polarizable force field to electric continuum

The ECC model describes a system with point charges moving in a homogeneous electronic continuum of the dielectric constant ϵ_{el} [137]. The homogeneous electronic continuum can effectively screen the electrostatic interactions between charges. The interactions are scaled by the factor $1/\sqrt{\epsilon_{\text{el}}}$.

Then, the energy W of a system can be expressed as [137]

$$W(r_1, \ldots, r_N) = \frac{1}{2}\sum_{i\neq j}^{N}\frac{q_i q_j}{r_{ij}} + \frac{1}{2}\sum_{i,j=1}^{N}\mathbf{d}_i\mathbf{K}(i,j)\mathbf{d}_j - \sum_{i=1}^{N}\mathbf{E}'(\mathbf{r}_i)\mathbf{d}_i + \sum_{i=1}^{N}W_{i0}, \quad (2.16)$$

where q and d are the partial atomic charges and the point dipoles, respectively. The electric field from other charges and dipoles induce the dipoles. The dipole-dipole interaction, the second term on the RHS of Eq. 2.16, is computed with the matrix $\mathbf{K}$ in which the diagonal elements are inverse polarizabilities $1/\alpha$. Here, the polarizabilities α is assumed to be the same for all charges. The third term on the RHS of Eq. 2.16 represents the interaction between the dipoles and the electric fields. The point dipole at $\mathbf{r}_i$ interacts with the electric field of other point charges $\mathbf{E}'(\mathbf{r}_i)$, which does not involve the electric field of the point charge at $\mathbf{r}_i$ (indicated by the prime). The last term is not necessary for the dynamics of the coordinates $\mathbf{r}_i$, meanwhile it is considered when the free energy of solvation energy is calculated. This constant is the sum of W_{i0} $= q_i^2/2r_i$, where r_i are the radii of the charge i.

The electronic polarizability of atoms is featured by the polarizable dipoles. Their motions are subject to an external field. The electric field $\mathbf{E}'(\mathbf{r}_i)$ is induced by point

atomic charges which are attached to the nuclei and changing their position simultaneously with the motion of the nuclei. Hence, the polarization of dipoles can be regarded as in equilibrium for all time. The equilibrium dipole moment $\bar{\mathbf{d}}_i$ is expressed as

$$\bar{\mathbf{d}}_i = \alpha\Big(\mathbf{E}'(\mathbf{r}_i) - \sum_{j\neq i}^{N} \mathbf{K}(i,j)\bar{\mathbf{d}}_j\Big). \tag{2.17}$$

The equilibrium dipole $\bar{\mathbf{d}}_i$ is the difference between the electric field $\mathbf{E}'(\mathbf{r})$, the field of other then charge q_i (the first term in the parenthesis), and the electric field of other dipoles $\mathbf{d}_j$ (the second term in the parenthesis). All equilibrium dipoles are subject to each other self-consistently as well as the position of the nuclei. When we plug Eq. 2.17 into the Eq. 2.16, it reads,

$$\begin{aligned} W(r_1,\ldots,r_N) = \frac{1}{2}\sum_{i\neq j}^{N}\frac{q_i q_j}{r_{ij}} + \frac{1}{2}\sum_{i,j=1}^{N}\alpha\Big(\mathbf{E}'(\mathbf{r}_i) - \sum_{j\neq i}^{N}\mathbf{K}(i,j)\bar{\mathbf{d}}_j\Big)\mathbf{K}(i,j)\mathbf{d}_j \\ - \sum_{i=1}^{N}\mathbf{E}'(\mathbf{r}_i)\alpha\Big(\mathbf{E}'(\mathbf{r}_i) - \sum_{j\neq i}^{N}\mathbf{K}(i,j)\bar{\mathbf{d}}_j\Big) + \sum_{i=1}^{N} W_{i0}. \end{aligned} \tag{2.18}$$

Then, Eq 2.18 becomes

$$W(r_1,\ldots,r_N) = \frac{1}{2}\sum_{i\neq j}^{N}\frac{q_i q_j}{r_{ij}} - \frac{1}{2}\sum_{i,j=1}^{N}\mathbf{E}'(\mathbf{r}_i)\alpha\Big(\mathbf{E}'(\mathbf{r}_i) - \sum_{j\neq i}^{N}\mathbf{K}(i,j)\bar{\mathbf{d}}_j\Big) + \sum_{i=1}^{N} W_{i0}. \tag{2.19}$$

Subsequently,

$$W(r_1,\ldots,r_N) = \frac{1}{2}\sum_{i\neq j}^{N}\frac{q_i q_j}{r_{ij}} - \frac{1}{2}\sum_{i=1}^{N}\mathbf{E}'(\mathbf{r}_i)\bar{\mathbf{d}}_i + \sum_{i=1}^{N} W_{i0}. \tag{2.20}$$

The second term on the RHS of Eq. 2.20 is the energy of the dipoles, which is analogous to electronic polarization energy. The dipole polarization can be expressed in terms of the polarized continuum as

$$\bar{\mathbf{d}}_i = \int_{Vai} \mathbf{P}'(\mathbf{r})\mathrm{d}\tau, \tag{2.21}$$

where $\mathbf{P}'(\mathbf{r})$, V_{ai} and τ are the polarization density, the volume of the i^{th} atom and an infinitesimal volume element, respectively. The prime of the polarization density is the polarization at $\mathbf{r}$ induced by other atoms and proportional to the local external

field $\mathbf{E}^{'}(\mathbf{r})$,

$$\mathbf{P}'(\mathbf{r}) = \frac{1}{4\pi}\frac{\epsilon_{\mathrm{el}}-1}{\epsilon_{\mathrm{el}}}\mathbf{E}'(\mathbf{r}). \tag{2.22}$$

The second term on the RHS of Eq. 2.20 is expressed as

$$W_{\mathrm{el}}(r_1,\ldots,r_N) = -\frac{1}{8\pi}\Big(\frac{\epsilon_{\mathrm{el}}-1}{\epsilon_{\mathrm{el}}}\Big)\sum_{i=1}^{N}\int_{V,ai}\mathbf{E}'^2(\mathbf{r}_i)\mathrm{d}\tau. \tag{2.23}$$

After additional steps, we express the equation above in terms of the discrete charge distribution of j and convert the double summation into the single summation,

$$W_{\mathrm{el}}(r_1,\ldots,r_N) = -\Big(\frac{\epsilon_{\mathrm{el}}-1}{\epsilon_{\mathrm{el}}}\Big)\Big(\frac{1}{2}\sum_{i\neq j}^{N}\frac{q_iq_j}{r_{i,j}} + \sum_{i=1}^{N}W_{i,0}\Big). \tag{2.24}$$

We now insert equation above into Eq. 2.16, and thus obtain the total energy with the scaling factor $1/\epsilon_{\mathrm{el}}$ as

$$W(r_1,\ldots,r_N) = \frac{1}{\epsilon_{\mathrm{el}}}\Big(\frac{1}{2}\sum_{i\neq j}^{N}\frac{q_iq_j}{r_{ij}} + \sum_{i=1}^{N}W_{i0}\Big). \tag{2.25}$$

Equation 2.25 implies that all interaction energies are scaled by the factor $1/\epsilon_{\mathrm{el}}$. The polarizable point charges q in the system are substituted by nonpolarizable point charges q^{eff} with the scaling factor, $q^{\mathrm{eff}} = q/\sqrt{\epsilon_{\mathrm{el}}}$, subsequently, it produces the effective energy

$$\frac{q_i^{\mathrm{eff}}q_j^{\mathrm{eff}}}{r_{ij}} = \frac{1}{\epsilon_{\mathrm{el}}}\frac{q_iq_j}{r_{ij}}, \tag{2.26}$$

which corresponds to the first term in Eq. 2.25. Namely, the total energy with polarizable charges and dipoles can be approximated by the effective charges with the scaling factor. We will apply this framework to concentrated liquid electrolytes and their application in energy-storage devices.

2.3 Statistical physics of liquids and analysis

2.3.1 Asymptotic decay of correlations

A liquid is a very dynamical system and the atomic positions are constantly changing. The atomic and molecular structure of liquids seems random, but unlike gas they are condensed and held together by cohesive forces. Consequently, atoms in a liquid are strongly correlated in position and momentum. The structure of a liquid cannot be suitably described by the positions of atoms, but rather in terms of their correlations. The decay of correlations between particle positions and how electric fields are screened are of fundamental importance in liquid state physics as well as electrochemical devices. Correlations are characterized by a decay length (analogously to a screening length) [138, 29] over which microscopic variables are correlated. To discuss the decay of correlations, we begin with the n-point particle-density correlation function, which is defined as,

$$\rho^{(n)}(\mathbf{r}^n) = \frac{N!}{(N-n)!}\frac{1}{Z_N}\int \exp(-\beta U_N) d\mathbf{r}^{N-n}, \tag{2.27}$$

where N, U_N and Z_N are the total number of particles, the total potential energy and the configuration integral, $Z_N = \int \exp(-\beta U_N) d\mathbf{r}^N$, respectively. The single particle density can be expressed as

$$\rho^{(1)}(\mathbf{r}_1) = \Big\langle \sum_i^N \delta(\mathbf{r}_1 - \mathbf{r}_i) \Big\rangle, \tag{2.28}$$

which is equal to the average density at a point $\mathbf{r}$ (or density profile) $\langle \rho(\mathbf{r}) \rangle = \rho^{(1)}(\mathbf{r}_1)$. The angular brackets indicate an ensemble average. In the case $n = 2$, the pair density $\rho^{(2)}(\mathbf{r}_1, \mathbf{r}_2)$ reads

$$\rho^{(2)}(\mathbf{r}_1, \mathbf{r}_2) = \Big\langle \sum_i^N \sum_{j \neq i}^N \delta(\mathbf{r}_1 - \mathbf{r}_i)\delta(\mathbf{r}_2 - \mathbf{r}_j) \Big\rangle. \tag{2.29}$$

A useful mathematical tool to examine the correlations is a general n-particle correlation function $g^{(n)}(\mathbf{r}^n)$. For homogeneous systems in equilibrium, it can be expressed in

terms of the n-particle density $\rho^{(n)}(\mathbf{r}^n)$ as follows:

$$g^{(n)}(\mathbf{r}^n) = \frac{\rho^{(n)}(\mathbf{r}^n)}{\rho^n}, \tag{2.30}$$

where ρ is the number density. Likewise, the the pair distribution $g^{(2)}(\mathbf{r}_1, \mathbf{r}_2)$ can be written as,

$$g^{(2)}(\mathbf{r}_1, \mathbf{r}_2) = \frac{1}{\rho^2}\Big\langle \sum_{i}^{N} \sum_{j \neq i}^{N} \delta(\mathbf{r}_1 - \mathbf{r}_i)\delta(\mathbf{r}_2 - \mathbf{r}_j)\Big\rangle. \tag{2.31}$$

If the systems is isotropic, the pair distribution $g^{(2)}(\mathbf{r}, \mathbf{r}')$ depends only on the separation, $r_{12} = |\mathbf{r} - \mathbf{r}'|$. The correlation function then turns into the radial distribution function and simply written as $g(r)$. The radial distribution function describes the variation of density as a function of the distance from a reference particle. As the analysis of the decay of the density profile in the asymptotic regime is subject to the properties of bulk liquid [139], it is convenient to introduce the total correlation, $h(r)$ $= g(r) - 1$, between particles 1 and 2 [140]:

$$h(r_{12}) = c(r_{12}) + \rho \int d\mathbf{r}_3 c(r_{13})h(r_{23}), \tag{2.32}$$

where $c(r)$ is the direct correlation function. This equation is the Ornstein-Zernike (OZ), which can be interpreted as the total correlation between particles 1 and 2 is influenced by the direct correlation c_{12} and also indirect correlations. Subsequently, the OZ equation can be solved recursively, which leads to

$$h(r_{12}) = c(r_{12}) + \rho \int d\mathbf{r}_3 c(r_{13})c(r_{23}) + \rho^2 \int d\mathbf{r}_3 d\mathbf{r}_4 c(r_{13})c(r_{24})c(r_{34}) + \mathcal{O}(c^4). \tag{2.33}$$

If the liquid is isotropic, we can rewrite the OZ equation as

$$h(r) = c(r) + \rho \int d\mathbf{r}' c(|\mathbf{r} - \mathbf{r}'|)h(r'). \tag{2.34}$$

By taking the Fourier transform of Eq. 2.34, we obtain the relation between $\hat{h}(q)$ and $\hat{c}(q)$ [141]

$$\hat{h}(q) = \frac{\hat{c}(q)}{1 - \rho\hat{c}(q)}. \tag{2.35}$$

The total correlation function $h(r)$ can be expressed as an inverse Fourier transform of $\hat{h}(q)$ [141, 140]

$$rh(r) = \frac{1}{4\pi^2 i}\int_{-\infty}^{\infty} dqq\exp(iqr)\frac{\hat{c}(q)}{1-\rho\hat{c}(q)}. \tag{2.36}$$

$\hat{h}(q)$ exhibits poles in conjugate pairs $q = q^{(n)} = \pm q_1^{(n)} + iq_2^{(n)}$, which is given by the complex solutions of the equation

$$1 - \rho\hat{c}(q) = 0. \tag{2.37}$$

The conjugate pairs are determined by the solutions of two equations [141, 140]

$$q_2^{(n)} = 4\pi\rho\int_0^{\infty} drrc(r)\sinh(q_2^{(n)}r)\cos(q_1^{(n)}r) \tag{2.38}$$

and

$$q_1^{(n)} = 4\pi\rho\int_0^{\infty} drrc(r)\cosh(q_2^{(n)}r)\sin(q_1^{(n)}r). \tag{2.39}$$

The imaginary pole $q_2^{(n)}$ is obtained from Eq. 2.38 by choosing $q_1^{(n)} \equiv 0$ [141].

Using the residue theorem [141, 140], the RHS in Eq 2.36 can be calculated with contour integration by considering an infinite radius semicircle in the upper half-plane. If R_n is the residue of $q\hat{c}(q)/[1-\rho\hat{c}(q)]$ at the nth pole, $q = q^{(n)}$, the integral is reduced to the sum of the residues [141, 140],

$$rh(r) = \frac{1}{2\pi}\sum_n R_n\exp(q^{(n)}r) = \frac{1}{2\pi}\sum_n R_n\exp(iq_1^{(n)}r)\exp(-iq_2^{(n)}r) \tag{2.40}$$

A pole determines the decay modes of $rh(r)$. If a singe pole lies on the imaginary part $q_2^{(n)}$ and $q_1^{(n)}$=0, it gives a pure exponential decay. On the other hand, if $q_2^{(n)} = 0$, the real part $q_1^{(n)}$ gives rise to oscillations [141, 140]. In case, a conjugate pair exist, $rh(r)$ decays in a damped oscillatory way. In principle, there might be an infinite number of poles, the contour can be formulated with a proper limiting condition. The exponential terms in Eq 2.40 ensure that in the long range $rh(r)$ is dominated by the pole or poles nearest the real axis. For example, if the nearest pole is purely imaginary, the decay

of $h(r)$ is given by [141, 140]

$$\lim_{r\to\infty} h(r) = \frac{\mathrm{A}}{r}\exp\left(-q_2^{(n)}r\right) \tag{2.41}$$

where A is a coefficient and $q_2^{(r)}$ equivalent to the decay length λ. In the other case, a conjugate pair is close to the real axis and the asymptotic behavior shows a damped oscillatory behavior,

$$\lim_{r\to\infty} h(r) = \frac{\mathrm{A}}{r}\exp\left(-rq_2^{(n)}\right)\cos\left(q_1^{(n)}+\varphi\right), \tag{2.42}$$

where $q_1^{(n)}$ corresponds to $2\pi r/l$, which is the decay oscillation frequency. The total correlation should decay at long range according to Eq. 2.41 or Eq. 2.42. Combinations of such functions may also exist. Therefore, these equations illustrate the decay length and the oscillation frequency in liquid electrolytes. In chapter 6, we proceed to investigate the decay lengths in highly concentrated liquid electrolytes by fitting those equations to simulation data.

2.3.2 Dielectric constant calculation: using the Einstein–Helfand relation

In chapter 5, we evaluate the permittivity in the simulations in two ways: (i) approximately but as typically done by considering only the rotational (dipolar) contribution to the polarization fluctuations, and (ii) accurately by additionally taking into account the translational contribution of the ions, via the Einstein-Helfand method. We recall here the most important steps presented *e.g.* in Ref [142] for ionic liquids.

The dielectric constant ϵ contribution from the average of the dipole moment fluctuation is given by

$$\epsilon = 1 + \frac{1}{3Vk_{\mathrm{B}}T\epsilon_0}(\langle\mathbf{M}^2\rangle - \langle\mathbf{M}\rangle^2) \tag{2.43}$$

In case, ECC model is employed, the total effective dielectric constant is expressed as

$$\epsilon_{\mathrm{eff}} = \epsilon_\infty\epsilon. \tag{2.44}$$

A possibility arises in splitting up $\mathbf{M} = \mathbf{M}_J + \mathbf{M}_D$ into a translational and rotational parts. The translational part is expressed as $\mathbf{M}_J = \sum q_i \mathbf{r}_{i,\mathrm{com}}$ and the rotational part is $\mathbf{M}_D = \sum \mu_{i,\mathrm{com}}$ where $\mu_{i,\mathrm{com}} = \sum_\alpha q_{i,\alpha}(\mathbf{r}_{i,\alpha} - \mathbf{r}_{i,\mathrm{com}})$ where α is atoms in the molecular i and com stands for center of mass.

$$\begin{aligned}\epsilon &= 1 + \frac{1}{3Vk_\mathrm{B}T\epsilon_0}\Big(\langle \mathbf{M}_D^2\rangle - \langle \mathbf{M}_D\rangle^2 + \langle \mathbf{M}_J^2\rangle - \langle \mathbf{M}_J\rangle^2 + 2(\langle \mathbf{M}_D\mathbf{M}_J\rangle - \langle \mathbf{M}_D\rangle\langle \mathbf{M}_J\rangle)\Big) \\ &= 1 + \frac{1}{3Vk_\mathrm{B}T\epsilon_0}\Big(\langle \mathbf{M}_D^2\rangle + \langle \mathbf{M}_J^2\rangle + 2\langle \mathbf{M}_D\mathbf{M}_J\rangle\Big).\end{aligned} \tag{2.45}$$

We have further used the fact that in thermodynamic equilibrium without external fields $\langle \mathbf{M}_J\rangle = \langle \mathbf{M}_D\rangle = 0$. The electrical current is the derivative of the translational dipole moment with respect to time, $\mathbf{J}(t) = (d/dt)\mathbf{M}_J$. Therefore we can transform the previous equation into

$$\langle \mathbf{M}_D\mathbf{M}_J\rangle = -\int_0^\infty \langle \mathbf{M}_D(0)\mathbf{J}(t)\rangle dt. \tag{2.46}$$

Using this relation, Eq. 2.45 can be transformed to

$$\epsilon = 1 + \frac{1}{3Vk_\mathrm{B}T\epsilon_0}\Big(\langle \mathbf{M}_D^2\rangle + \langle \mathbf{M}_J^2\rangle - 2\int_0^\infty \langle \mathbf{M}_D(0)\mathbf{J}(t)\rangle\Big). \tag{2.47}$$

In order to compute ϵ in Eq. 2.47, $\langle \mathbf{M}_D^2\rangle$ can be calculated by direct averaging over the MD simulations, while $\langle \mathbf{M}_J^2\rangle$ is obtained with the Einstein-Helfand method,

$$\langle [\mathbf{M}_J(t'+t) - \mathbf{M}_J(t')]^2\rangle = 6Vk_\mathrm{B}T\kappa t + 2\langle \mathbf{M}_J^2\rangle. \tag{2.48}$$

where κ is the ionic conductivity. In order to estimate the mean square displacement (MSD) of the translational part of the dipole moment $\langle \mathbf{M}_J^2\rangle$ in chapter 5, we employed two trajectories (100 and 50 ns) in each concentration. An example of the mean square displacement of $\mathbf{M}_J$ is shown for 1 M LiCl (aq) in Fig. 2.1.

The intercept is obtained for each simulation from a fit in the linear regime (indicated by a gray area in Fig. 2.1) and the final value is taken as the average over trajectories. In order to perform this calculation on the systems of LiTFSI(aq) in chapter 6, it is

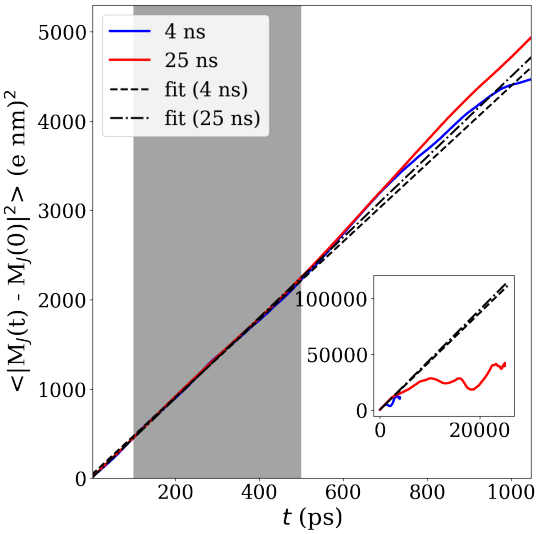

Figure 2.1: MSD of the translational part of the dipole moment in 1M LiCl (aq) using Eq. 2.48. For each system in chapter 6, two trajectories are used to determine the linear regime. Insets show larger range of the MSD data. The dashed and dash-dotted lines are the linear fit (within the filled gray regime) for the red and blue lines, respectively.

necessary to have snapshots of a very high sample frequency (with positions sampled every 10 steps, or 10 fs) to obtain a reliable dielectric constant. To facilitate data storage, a new set of simulations was performed for each concentration with smaller boxes, where the edge length was 4 nm. These simulations had a length of 2-4 ns with the simulations extended as long as necessary to extract the intercept of the MSD with a relative error of less than 5% as calculated from the variance of the intercept of a linear fit using the least squares method.

2.3.3 Diffusion coefficients

The self-diffusion coefficients of ions and molecules are computed via the MSD relation,

$$D_{\mathrm{MD}} = \lim_{\Delta t \to \infty} \frac{\left\langle r^2(\Delta t) \right\rangle}{6\Delta t}. \tag{2.49}$$

In addition, the finite-size effects of the simulation box are corrected by extrapolating measured D_{MD} values at different box sizes L to $L \to \infty$ (*cf* Fig. A.1 in Appendix).

2.3.4 Conductivity, transference numbers and ion pairing

Conductivities of the solutions in our simulations are computed from Ohm's law

$$\mathbf{J} = \kappa \mathbf{E}, \tag{2.50}$$

where $\mathbf{E}$ is an applied electric field and $\mathbf{J} = \sum_i \mathbf{J}_i = \sum_i \kappa_i \mathbf{E}$ is the resulting total current density. This relation defines partial ionic conductivities κ_i for each individual ionic species. The conductivities κ_i are evaluated from the linear slope of $\mathbf{J}$ versus $\mathbf{E}$ in the linear-response regime.

With the ratio between the individual current density $\mathbf{J}_i$ (or conductivity) and the total current density $\mathbf{J}$, the transference number of the ion i is defined as [143]

$$t_i = \frac{\mathbf{J}_i}{\mathbf{J}} = \frac{\kappa_i}{\kappa}, \tag{2.51}$$

In addition, the degree of ion uncorrelated motion is expressed as,

$$\alpha = \frac{\kappa}{\kappa_{id}}. \tag{2.52}$$

The ideal ionic conductivity κ_{id} in the limit of low concentrations is given by the Nernst–Einstein (NE) equation,

$$\kappa^{\mathrm{id}} = \frac{e^2}{k_{\mathrm{B}} T} \sum_i z_i^2 c_i D_i, \tag{2.53}$$

where z_i stands for the ion valency of species i and c_i and D_i for the ion concentration and diffusion coefficient of species i, respectively.

2.3.5 Clustering

In chapter 4, we define a cluster of PS ions as a group of those PS ions whose at least one of the terminal S atoms is separated from a terminal S atom of any other PS ion in the cluster by less than $r_0 = 0.53$ nm. The cutoff value r_0 is chosen as the first minimum after the main peak of the RDF of terminal S atoms and thus corresponds to the distance between two terminal S atoms that have a bridging Li^+ ion in between.

By ensemble averaging of clusters in the simulations, we obtain an equilibrium cluster size distribution $P(N)$, where N is the number of PS ions in a cluster. The statistical uncertainties are calculated with the block averaging procedure.

2.3.6 Coordination number

The coordination number $N_{i,j}$ of the molecule of type i that is surrounded by molecules of type j is computed from the RDF as [140]

$$N_{i,j} = 4\pi c_j \int_0^{R_\mathrm{M}} g_{ij}(r)\, r^2 \,\mathrm{d}r, \tag{2.54}$$

where R_M is the distance of the first minimum after the first peak in the RDF and c_j is the bulk concentration of molecules of the type j.

2.3.7 Viscosity

To evaluate the viscosity in our simulations, we use the Green-Kubo relation [144] and the transverse current correlation function [145, 100, 144]. The shear viscosity using the Green-Kubo relation is

$$\eta^\mathrm{GK} = \lim_{t\to\infty} \frac{1}{2} \frac{V}{k_\mathrm{B}T} \frac{\mathrm{d}}{\mathrm{d}t} \left\langle \left(\int_{t_0}^{t_0+t} P_{xz}(t')\mathrm{d}t' \right)^2 \right\rangle_{t_0} \tag{2.55}$$

where the integration time is performed over the shear stress $P_{xz}(t)$.

The second approach that we use to obtain the shear viscosity η_∞ is transverse current correlation function [145, 100, 144], using the transverse momentum fields (transverse-current autocorrelation function). Here, a total 16 transverse-current autocorrelation functions corresponding to different k-vectors are considered, resulting in 16 values of η. The values of η are fitted to $\eta(k) = \eta_\infty(1 - ak^2)$, yielding the shear viscosity, η_∞. a is a fitting parameter.

In cases of binary solvent mixtures, we compare the results for the viscosity to the values obtained via well-established semi-empirical analytical mixing rules by Fort and Moore [146] for the experimentally expected viscosity. There, the viscosity η_mix of a

mixture is calculated from the viscosities of the pure components $\eta_{\infty,1}$ and $\eta_{\infty,2}$ as

$$\eta_{\mathrm{mix}}(\phi_1, \phi_2) = \eta_{\infty,1}^{\phi_1} \eta_{\infty,2}^{\phi_2}. \tag{2.56}$$

The volume fractions ϕ_1 and ϕ_2 of each of the components, $\phi_i = V_i/(V_1 + V_2)$, are obtained from the partial volumes V_i calculated as $V_i = m_i/\rho_i^0$ with ρ_i^0 being the mass density of the pure component.

3 Electrolyte structure and dynamics in battery solvents

3.1 Introduction

Li/S batteries are discussed as a cost efficient key technology for future applications in portable electronic devices, electromobility, and as a backup storage system for the reliable use of renewable energies [147, 148, 149, 54]. The actual performance delivered by Li/S batteries is proving to be severely limited in many cases, which is directly related to the role of the electrolyte [51, 150, 151, 152, 153, 154, 155]. Ultimately, the successful development of the Li/S battery requires careful coordination of the choice of electrolyte with the specific nature of the cathode material. In particular, the optimal electrolyte has to fulfill several boundary conditions, as such to maximize charge carrier conductivity and high ionic dissociation but also to guarantee lithium ion dissolution and stabilization of the lithium anode [18].

Recent developments have empirically demonstrated that LiTFSI in 1:1 mixtures of the organic solvents DME and DOL are found to be a suitable electrolyte solution for Li/S batteries, satisfying many of the requirements [150]. For fundamental structural insights on a molecular level and rational guidance of experimental developments, efficient and accurate molecular simulations are of significant importance. For example, they can demonstrate how the details of local solvation structures or ion pairing affinities can be linked to transport properties, such as diffusion and conductivity, *i.e.*, they establish *structure-property* relationships. In particular, they elucidate the effects of organic solvents on the lithium ion solvation and transport in ionic liquid electrolytes [156], *i.e.*, the solvate structures of LiTFSI electrolytes [157, 158] as well as the influence of cations on lithium ion coordination and transport [159]. However, despite their importance for modern Li/S battery development, the simulation studies of the structural properties of the lithium salts in mixtures of DME/DOL solvents are

scant [98]. Of particular interest is, for instance, an accurate structural characterization of the local lithium solvation structure, which is decisive for ion permeation and capacitance build-up within the commonly used porous organic electrode materials. Once a good basic electrolyte model is available, further extensions can successively built up on this (*e.g.*, by including the sulfur component, electrode materials, etc.) and combinatorial solvent/electrolyte optimization and the establishment of quantitative structure-property-function relationships of Li/S battery systems come into closer reach.

We construct an MD computer simulation model of representative state-of-the-art electrolyte–solvent systems used in metal-sulfur or metal-air batteries constituted by LiTFSI and $LiNO_3$ electrolytes in mixtures of the organic solvents DME and DOL. We benchmark and verify our simulations by comparing structural and dynamic features with various available experimental reference systems and demonstrate their applicability for a wide range of electrolyte–solvent compositions. Therefore, in this chapter, we finally calculate and discuss the detailed composition of the first lithium solvation shell, the temperature dependence of lithium diffusion, as well as the electrolyte conductivities and lithium transference numbers.

3.1.1 Simulated systems

We simulate eight different solution 'systems' denoted in the following as systems I, IIa, IIb, IIc, IIIa, IIIb, IVa, and IVb with the particular number of ions and molecules in the simulation box summarized in Table 3.1. The system I does not include ions and consists only of a reference binary mixture of DME and DOL of varying composition. We express the organic solvent composition as the molar fraction x of DOL in the solvent,

$$x = \frac{N_{\mathrm{DOL}}}{N_{\mathrm{DOL}} + N_{\mathrm{DME}}} \tag{3.1}$$

where N_{DOL} and N_{DME} correspond to the number of DOL and DME molecules, respectively. In the system class II we additionally include one Li^+ (IIa), or one Li^+-NO_3^-

pair (IIb), or one Li^+-$TFSI^-$ pair (IIc) to investigate diffusion and structural properties in the high dilution limit of electrolyte, also for various ratios $x = 0$ to 1. Systems IIIa and IIIb relate to an experimental study where diffusion coefficients and conductivity were accurately measured [160] and consists of 25 Li^+-$TFSI^-$ ion pairs in either 500 DME or 500 DOL solvent molecules, respectively. The molar ratio between salt and solvent is thus 1:20 in this system. Finally, systems IVa and IVb represent experimental state-of-the-art compositions for a few modern batteries under development and consider concentrated electrolyte mixtures of Li^+, NO_3^-, and $TFSI^-$ at molar concentrations, prepared from Institute for Electrochemical Energy Storage (IEES) at Helmholtz-Zentrum Berlin (HZB). IVb has a similar ionic strength as IVa but contains no nitrate ions.

Table 3.1: Numbers of ions and solvent molecules (*i.e.*, the composition) in the investigated simulation systems. System I does not contain ions and the molar ratio $x = N_{\mathrm{DOL}}/(N_{\mathrm{DOL}} + N_{\mathrm{DME}})$ of DME/DOL is varied between 0 and 1 with a total number of 508 solvent molecules. System class II has only one Li^+ ion (IIa) or one ion pair (IIb and IIc) for various DME/DOL ratios. System class III features a 1:20 LiTFSI molar ratio in either DME (IIIa) or DOL (IIIb). System IVa and b are representative experimental state-of-the-art systems [150, 161] for Li/S batteries with a molar composition of (a) 0.66 M $LiNO_3$, 0.33 M LiTFSI, 4.94 M DME, and 6.03 M DOL and (b) 0.88 M LiTFSI, 4.64 M DME, and 5.67 M DOL [16].

System	Li^+	NO_3^-	$TFSI^-$	solvent (DME / DOL)
I	-	-	-	0..508 / 0..508
IIa	1	-	-	0..508 / 0..508
IIb	1	1	-	0..508 / 0..508
IIc	1	-	1	0..508 / 0..508
IIIa	25	-	25	500 / 0
IIIb	25	-	25	0 / 500
IVa	90	60	30	450/550
IVb	85	0	85	450/550

3.1.2 Force fields

Due to the multi-component nature and the many degrees of freedom in our rather low dielectric systems, the parametrization of the model to reproduce a wide range

of properties is notoriously difficult. Systematic deviations to experiments of some of the properties are the rule other than exception but may be improvable in future with further application and extension of the model. However, we will demonstrate, despite the high complexity of these liquids, that a wide range of important equilibrium and transport properties on different scales are well reproduced (within a satisfactory error range) by our specific parametrization. In our parametrization strategy, first we have scrutinized the properties of pure solvents of DME and DOL using various force fields and compared them with experimental benchmarks in terms of density, dielectric constant, and viscosity. The properties of DOL were assessed with three different force fields: AMBER [112], the Transferable Potentials for Phase Equilibria united-atom force field (TraPPE) [162], and the OPLS-AA [115]. For DME, only AMBER and OPLS-AA force fields were applicable. For DME, instead of the standard dihedrals in the latter two force-fields, we implemented the optimized dihedral parameters as suggested by Anderson *et al.* [163] based on the comparison with experimental measurements of the molecular conformation populations. The torsional degrees of freedom lead to the occurrence of many different equilibrium conformers and thus significantly affect the instantaneous dipole moment as discussed below in Results section. Table A.1 in Appendix, we summarize the MD simulations results for the solvents from all tested force fields.

The Coulomb interactions of ions are treated by the ECC method (see Section 2.2) [164, 137, 165, 166, 167, 168, 131], which takes the electronic polarizability into account implicitly. In this approach, formal ionic charges q_i in the interaction Hamiltonian are replaced by effective, rescaled values q_i^{eff},

$$q_i^{\text{eff}} = \frac{q_i}{\sqrt{\epsilon_\infty}}, \tag{3.2}$$

where $\epsilon_\infty = 1.93$ is the high-frequency dielectric permittivity of the bare solvent.

Here, ϵ_∞ is the high-frequency contribution to the solvent permittivity stemming from electronic fluctuations in the solvent molecules [169]. It can be related to the refractive index n as $\epsilon_\infty = n^2$. From the refractive indices n of 1.3781 for DME and 1.3992 for DOL [169], respectively, we obtain an effective charge of a monovalent ion of 0.73 in

DME and 0.71 in DOL using Eq 3.2. We further assume that the effective charge in a mixture of DME and DOL is given simply via a linear interpolation between the effective charges in the pure DME and the pure DOL solutions. We apply Eq 3.2 to all the partial charges of the three considered ions in our study, Li^+, $NO_3{}^-$, and $TFSI^-$. Available $TFSI^-$ and $NO_3{}^-$ force-fields parameters are taken from Refs. [170, 171].

On the case of Li^+, we have tested various established LJ parameters and compared them with experimentally available diffusion coefficients of dilute LiTFSI electrolyte in pure DME and DOL solvents (later defined as system III) [160]. While we found that the spread among the performance of the various force fields for the lithium ion is small, *i.e.*, within 15% for the diffusion coefficient, the best overall performance in combination with the opted anionic force-fields was exhibited by the lithium force field by Dang *et al.* [172]. Hence the latter has been finally chosen for all our investigated systems with rescaled charges as defined above (see Table A.2 and A.3 in Appendix).

3.2 Results

3.2.1 System I: Pure solvent (DME/DOL) mixtures

The density and dielectric constant of the DME/DOL mixtures as a function of the molar composition x are shown in Fig 3.1(a) and (b), respectively. The density of the pure DME (*i.e.*, $x = 0$) obtained from MD is $853\,\mathrm{kg\,m^{-3}}$, which very well agrees with the experimental value of $861\,\mathrm{kg\,m^{-3}}$ [173]. Also the density of the pure DOL (*i.e.*, $x = 1$) from MD, $1047\,\mathrm{kg\,m^{-3}}$, is in good agreement with the experimental one, $1059\,\mathrm{kg\,m^{-3}}$ [174]. The density of the mixture increases monotonically with the molar fraction x of DOL. Turning to the dielectric constant in panel (b) we find satisfactory agreement for the pure DOL solvent at $x = 1$, where the simulated value is about 16% smaller than in experiments. The MD value for pure DME ($x = 0$) is less satisfying and with 10.6 compared to the experimental 7.1 almost 50% too large. However, after having examined and thoroughly scrutinized various force field combinations, we found this deviation still to be minimal under the constraint that the density as well as the

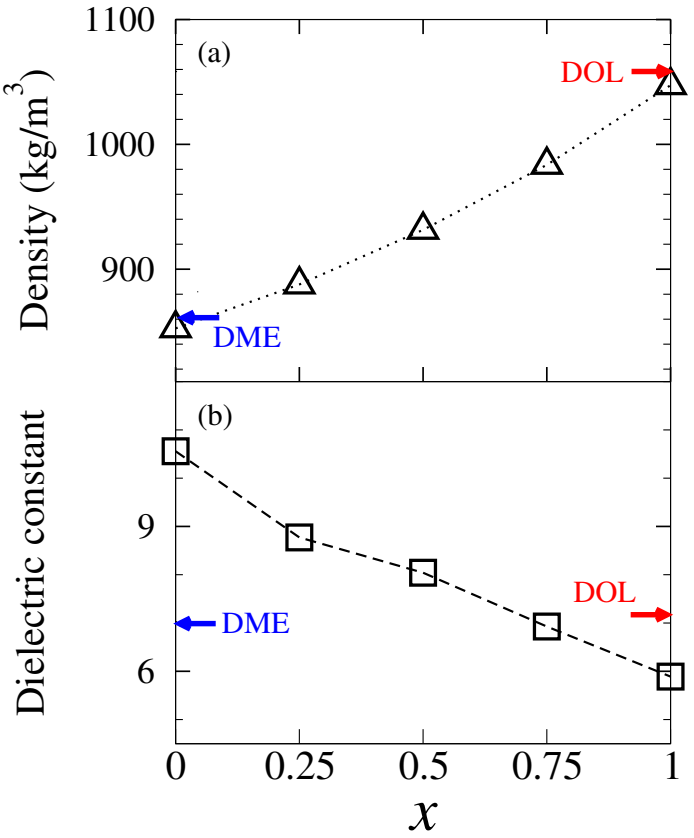

Figure 3.1: (a) Density of the DME/DOL mixture (System I) versus the molar composition $x = N_{\mathrm{DOL}}/(N_{\mathrm{DOL}} + N_{\mathrm{DME}})$ from our MD simulations (triangular symbols). (b) Dielectric constant (square symbols) from the MD, Eq. 2.44, for the same systems as in (a). The colored arrows indicate the experimental reference values of pure DME [173] and pure DOL [174], respectively.

viscosity (shown below) reproduce well the experimental reality. The occurrence of several, quite different equilibrium conformers for DME renders the precise reproduction of the mean dielectric constant difficult.

The viscosity of the DME/DOL mixtures from our simulations is presented in Fig 3.2(a). There, we also plot experimentally measured viscosities or pure solvents and apply the analytical mixing rule Eq. 2.56 for the mixtures. We see that the simulations for pure DME and DOL systems yield viscosities of 0.43 mPa s and 0.56 mPa s, respectively, which compare well with the experimental ones of 0.42 mPa s and 0.58 mPa s [174, 173], as well as with the expected interpolation behavior, Eq. 2.56. As another important transport property we have calculated the self-diffusion coefficients of the solvent molecules in the mixture, cf. panel (b) of the same figure. The simulations, corrected for finite-size effects (Figs. A.1 in Appendix), underestimate the experimental refer-

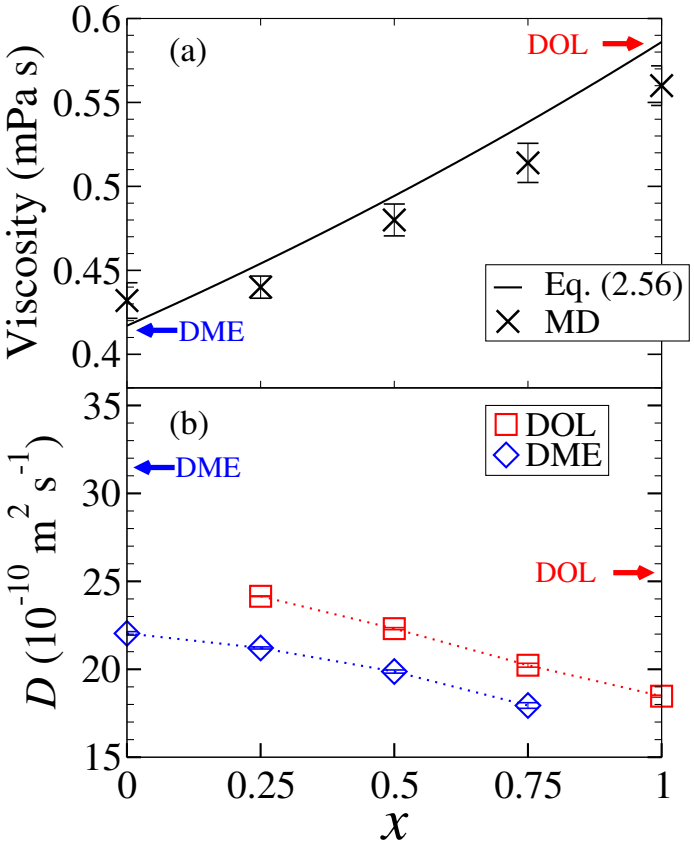

Figure 3.2: (a) Shear viscosity $\eta(x)$ of the binary DME/DOL mixtures versus composition x. Crosses indicate the results obtained from the MD simulations and the solid line represents the viscosity of the binary mixture from Eq. (2.56, which interpolates the experimental limits of pure DME [173] and pure DOL [174], indicated by arrows. (b) Self-diffusion coefficients of DME molecules (diamonds) and DOL molecules (squares) in the DME/DOL mixture as a function of the DOL molar fraction x. The experimental reference values of DME and DOL [160] are indicated by a blue and a red arrow, respectively.

ences values by 27% (DME) and 32% (DOL). The interpolation between the limits $x = 0$ and $x = 1$ transits monotonously.

In essence, we can conclude that transport properties are well captured within the MD model, while the self-diffusion is by about 30% too low. For a full quantitative comparison to experimental diffusion data, hence a scaling factor of about 4/3 may need to be introduced. However, overall we find satisfying behavior of our solvent force field in the sense that it can reproduce reasonably well several experimentally important equilibrium thermodynamic and transport properties for the full molar ratio range $x = 0$ to $x = 1$ at the same time.

3.2.2 Systems IIa, IIb, and IIc: single ions or ion pairs in mixed DME/DOL solvents

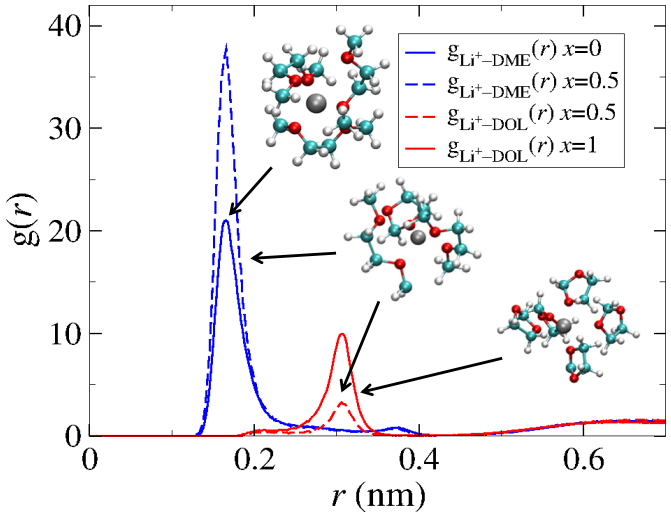

Figure 3.3: Center-of-mass RDF between Li^+ and solvent molecules for system IIa; The $g_{Li^+–DME}(r)$ and $g_{Li^+–DOL}(r)$ are shown for the limiting cases $x = 0$ (DME only) and $x = 1$ (DOL only) and for the intermediate ratio $x = 0.5$.

Now we consider highly dilute electrolyte solutions, where we investigate the solvation structure and diffusion of a single Li^+ ion (Sys. IIa), Li^+-NO_3^- (IIb), and Li^+-$TFSI^-$ (IIc) ion pairs in the solvent mixture of system I. In order to discuss the solvation structure, we plot in Fig 3.3 the center-of-mass RDF between the Li^+ and solvent molecules in system IIa: The $g_{Li^+–DME}(r)$ and $g_{Li^+–DOL}(r)$ are shown for the limiting cases $x = 0$ (DME only) and $x = 1$ (DOL only) and for the intermediate ratio $x = 0.5$. The DME distribution peaks at about 0.16 nm and is thus closer to the Li^+ than DOL molecules, whose distribution peaks at about 0.3 nm. Such a close approach of DME is consistent with experimental data where the Li^+-DME coordination leads to *cis* (the C-O bonds) and a *gauche* configurations in DME molecules in a bidentate binding configuration [175, 176]. This is absent for DOL, cf. also the representative simulation snapshots in Fig 3.3. Thus, the coordination of DME in the bidentate to Li^+ retains a relatively stable solvation structure even at the symmetric solvent ratio $x = 0.5$.

The consequence is an interesting coordination behavior along the mixing coordinate x as presented in Fig 3.4(a) for system IIa: let us start at the right hand side of the

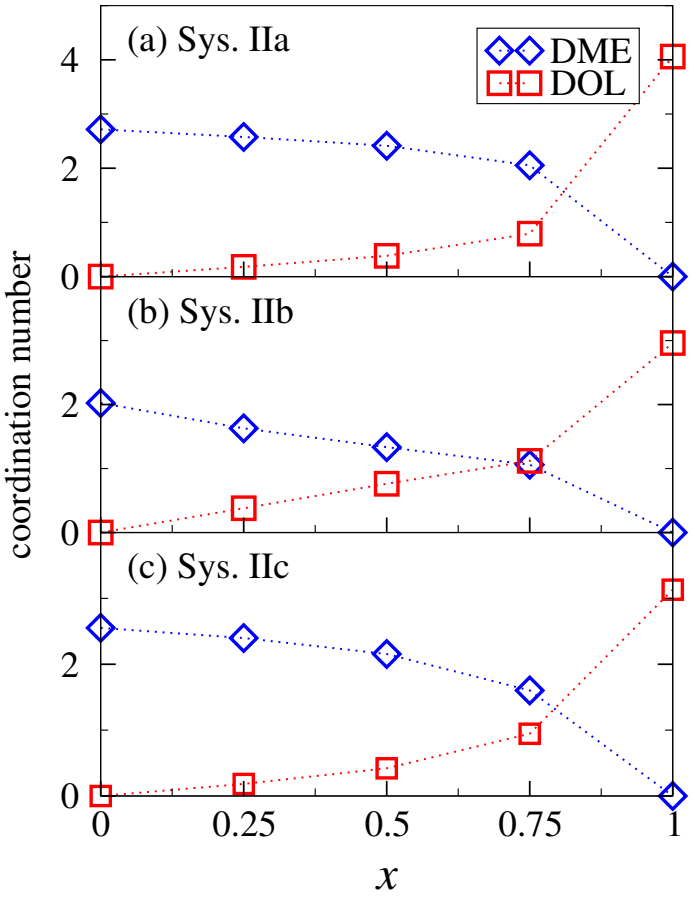

Figure 3.4: Coordination number of Li^+ of DME (blue diamonds) and DOL (red squares) molecules as a function of molar fraction x in the systems IIa, IIb, and IIIc. The dotted connecting lines are plotted as guides to the eye.

plot at $x = 1$, where DOL coordinates the cation with a coordination number of 4. Adding DME to the solution very quickly substantially changes the DOL coordination; already at around $x \simeq 0.8$ the coordination of DME and DOL equalize (at about 1.8). At a symmetric concentration ($x = 0.5$) the DME is then in large excess with a coordination close to the limiting coordination of about 2.7 of the pure DME ($x = 0$). We note that an analogous 'solvent-exchange' behavior has been observed previously already in DME/propylene carbonate mixtures [177], pointing to the special excess solvation properties of DME in general for its mixtures with other solvents.

For systems IIb and IIc, where also an additional anion is present, corresponding to concentration around 20 mM of the electrolyte, the cation coordination number decreases, but qualitatively retaining the behavior with varying the composition x,

see Fig 3.4(b) and (c). The reason is a strong ion pairing but which is anion-specific. The relatively small NO_3^- counterion binds very tightly to the Li^+ cation (see also the discussion later for the concentrated system IV). The strongly associated Li^+-NO_3^- ion pairs in pure DME indeed have been categorized previously already as a 'contact ion pair' (CIP) or even 'aggregate' solvation structure [176]. In this case the coordination by the organic solvent is consequently reduced by 1 in the whole x-range. The larger $TFSI^-$ anion, however, consistent with the category of a dissociated salt forming 'solvent-separated ion pairs' (SSIPs) in pure DME [176], only manages to replace a bigger weaker bound DOL molecule, but not DME molecules. Consequently, the DME coordination around Li^+ close to $x = 0$ remains almost unaffected by the presence of the $TFSI^-$ ion.

The SSIP solvate structure of LiTFSI ion pairs in DME can also be empirically explained with the Gutmann donor number (DN) [178, 179]. which corresponds to the negative binding enthalpy of a given molecule to a certain reference (Lewis) acid. Assuming Li^+ to behave as such a Lewis acid, the DN provides an estimate for the binding affinities of other molecules to Li^+. DME has the DN number of 20, while $TFSI^-$ the value of 5. Hence, much weaker association strength of Li^+-$TFSI^-$, as indicated by the smaller DN number, leads to the solvation shell of Li^+ dominated by DME (with higher DN). Our results are in line with the reported ionic strength in aprotic solvents in general, where the $TFSI^-$ has much smaller association strength than NO_3^- [176].

The self-diffusion coefficients of the molecular constituents in all systems of class II are presented in Fig 3.5. In these dilute systems (molar ratio 1:508) the diffusion properties of the pure organic solvent mixtures of DME and DOL are hardly affected. The Li^+ diffusion coefficient is between $13 \times 10^{-10}\,m^2\,s^{-1}$ at $x = 0$ and $9 \times 10^{-10}\,m^2\,s^{-1}$ at $x = 1$ in system IIa, *i.e.*, decreasing with increasing DOL concentration. This effect can be attributed to the larger width of the solvation shell in the higher coordinated DOL solvent. An inclusion of the counterion has small but visible effects and depends on anion type. For NO_3^- a strong ion pair is created, which evidently changes the Li^+ diffusion only very slightly although a joint diffusion of the cation–anion pair is apparently established. In the presence of a larger $TFSI^-$ anion, the Li^+ cation

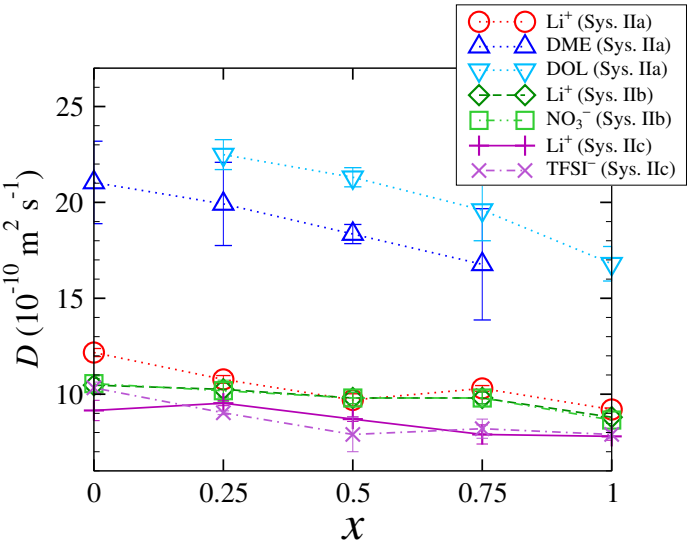

Figure 3.5: Diffusion coefficients of Li^+, NO_3^-, $TFSI^-$, DME, and DOL in Sys. IIa, IIb and IIc as a function of the DOL molar fraction x.

diffusion is slowed down more, probably related to a larger size of the formed ion pair, although only existent as an SSIP cluster.

3.2.3 Sys. IIIa and IIIb: 1:20 electrolyte to solvent ratio

Now we investigate the systems with the molar ratio of 1:20 LiTSFI:DME or LiTSFI:DOL, for which accurate experimental data for the conductivity, lithium transference, ionic dissociation degree, and diffusion coefficients are available [160]. Other physical properties, such as density, dielectric constant, viscosity, and solvent coordination are also calculated and summarized in Table 3.2 together with the experimental diffusion data. As we see, the total conductivity, lithium transference, as well as ionic degree of association are quite well reproduced. In the case of the self-diffusion of DME and DOL the computed diffusivity is lower, which is expected as the pure solvent diffusion is already by a factor 3/4 too low, see section 3.2.1. The diffusion coefficients of the Li^+ and $TFSI^-$ ions from the MD also consistently reproduce the experimental trends [160] in both systems IIIa and IIIb but are also overall slightly too low (again by about a factor 3/4). In general, it is observed that the diffusivity in system IIIa is faster than that of IIIb. It can be attributed to the lower viscosity of DME with respect to DOL. Com-

Table 3.2: Density, dielectric constant, viscosity, Li^+ coordination, conductivity and diffusion coefficients of systems IIIa (1:20 LiTFSI salt in pure DME), IIIb (1:20 LiTFSI salt in pure DOL), IVa [0.66 M $LiNO_3$ and 0.33 M LiTFSI in DME:DOL (45:55 molar ratio)] and IVb [0.88 M LiTFSI in DME:DOL (45:55 molar ratio)]. Systems IIIa and IIIb are conducted at $T = 304$ K, whereas IVa and IVb at 298 K. Experimental measurements of conductivity in this work is carried out with 0.6 M $LiNO_3$ and 0.3 M LiTFSI in a DME and DOL (1:1 wt%) mixture at room temperature.

	Sys. IIIa		Sys. IIIb		Sys. IVa		Sys. IVb	
	MD	Exp. [160]	MD	Exp. [160]	MD	Exp. (this work)	MD	Exp.
Density ($kg\,m^{-3}$)	934.1(2)		1147.0(1)		1030.0(1)	1103	1091.2(1.1)	1125[a]
Dielectric constant ϵ	8.8		5.7		7.6		6.6	
Viscosity (mPa s)	0.57(5)		0.74(5)		0.77(1)	0.88	0.85(3)	1.56[b], 1.25[c]
Coordination number of Li^+	2.45		3.04		3.2		3.2	
Conductivity ($S\,m^{-1}$)	0.73(3)	0.89	0.27(3)	0.31	0.36(4)	0.59(3)	0.82(3)	1.47[a], 1.32[b], 1.1[c]
Dissociation degree α	0.28	0.31	0.1	0.1	0.12		0.3	
Li^+ transference t_{Li^+}	0.4	0.47	0.5	0.51	0.61		0.38	
D_{Li^+} ($10^{-10}\,m^2\,s^{-1}$)	7.2(1.1)	7.7	5.1(4)	6.4	4.0(3)		4.7(3)	4.3[d]
D_{TFSI^-} ($10^{-10}\,m^2\,s^{-1}$)	7.8(1.3)	8.8	4.5(7)	6.2	5.0(1.0)		3.8(1.0)	4.8[d]
$D_{NO_3^-}$ ($10^{-10}\,m^2\,s^{-1}$)					3.9(3)			
D_{DME} ($10^{-10}\,m^2\,s^{-1}$)	16.4(1.3)	22.0			9.9(1.0)		8.2(1.0)	7.7[d]
D_{DOL} ($10^{-10}\,m^2\,s^{-1}$)			12.9(4)	17.0	13.1(1.0)		10.0(1.0)	11.4[d]

[a]Ref. [16]; [b]Ref. [180]; [c]Ref. [181]; [d]Ref. [98].

pared with the simulations results of the highly diluted electrolyte in systems II (1:500 ion–solvent ratio), the diffusivities in systems III are all found about 20% (DME) to 35% (DOL) lower due to the higher viscosity by the same relative amount.

The coordination solvent numbers for Li^+ in systems IIIa and IIIb are 2.45 and 3.04, respectively (see Table 3.2). The corresponding RDFs (see Figs. A.2 in Appendix)

indicate, analogously to systems II, that the DME molecule solvates Li^+ much stronger than DOL. The distance between Li^+ and the centers-of-mass of DME and Li^+ and DOL are 0.16 and 0.30 nm, respectively, which is in accord with $g_{Li^+–DME}(r)$ and $g_{Li^+–DOL}(r)$ for $x = 0$ and $x = 1$ in the molar ratio of 1:500 in Sec 3.2.2, respectively. The $g_{TFSI^-–DME}(r)$ and $g_{TFSI^-–DOL}(r)$ (see Figs. A.3 in Appendix) show the first peaks at 0.67 nm and 0.65 nm, respectively, which are relatively low, similarly as in the much more dilute systems II. This implies that the affinities between $TFSI^-$ and DME or DOL are relatively small and do not strongly depend on the salt concentration.

3.2.4 Systems IVa and IVb: Li/S battery electrolyte solution

Systems IVa and IVb consider practical Li/S battery electrolyte solutions with about 0.99 M salt concentration in a 45/55 molar ratio DME/DOL solvent. The individual molar concentrations are 0.66 M $LiNO_3$, 0.33 M LiTFSI, 4.94 M DME, and 6.03 M DOL in system IVa and nitrate-free with 0.88 M LiTFSI, 4.64 M DME, and 5.67 M DOL in system IVb. Table 3.2 shows the comparison between system IVa, IVb and experimental results for the density and viscosity, dielectric constant, conductivity and diffusion coefficients, as well as the MD results for the nitrate-free system. The MD simulations are able to reproduce well the available experimental values, further verifying the quality of our implemented force field. The MD model reproduces very well all the diffusion coefficients in system IVb (with deviations below 20%). Moreover, it yields the conductivity of $0.36\,S\,m^{-1}$, which is around 40% lower than the experimental value of $0.59\,S\,m^{-1}$, but correctly catches the trend of decrease in conductivity due to introduction of NO_3^- ions (compare systems IVa, IVb; interpolating experimental conductivity measurements at different $LiNO_3$ molar concentrations are available in Table A.4 in Appendix).

The value of the transference number of the Li^+ in system IVa is about 0.6. The relatively low dissociation number ($\alpha \simeq 0.12$) together with the large ratio between ionic and solvent diffusion (cf. Table 3.2) implies that strong ion pairing takes place. Namely, the affinity between Li^+-NO_3^- ion pairs (CIP) in system IVa is large, resulting

in correlated diffusion, meanwhile, Li^+-$TFSI^-$ ions in system IVb are well separated by solvents and contribute to higher conductivity than system IVa. Since the MD conductivities are significantly too low, even after possible correction with the diffusion scaling factor of 4/3, it seems that ion pairing is a bit overestimated in our simulations. The conductivity from experimental measurements also show a decrease as $LiNO_3$ molar concentration increases (Table A.4 in Appendix). This all are clear signatures of the fact that ionic conductivity is affected by not only ionic strength but also ion-specific pairing.

We are now in the position to interpret and predict interesting properties of these state-of-the-art battery electrolytes and how they depend, for example, on the solvent composition or temperature. Furthermore, we can also have a deeper microscopic insight into structural details, *e.g.*, the detailed composition of the first solvation shell of lithium. Hence, in the following, we concentrate exemplarily on the self-diffusion coefficient of the molecules and their temperature dependence and discuss structural features of the first Li^+ solvation shell in system IVa.

Table 3.3: Fitting parameters $\ln D_0$ and ΔE_a according to the Arrhenius law for the self-diffusion coefficients in system IVa.

Molecules	$\ln D_0$	ΔE_a ($kJ\,mol^{-1}$)
Li^+	6.3(3)	12.1(1)
NO_3^-	6.0(3)	11.3(1)
$TFSI^-$	7.4(3)	14.5(2)
DME	7.5(3)	12.8(1)
DOL	7.7(3)	12.8(1)

Table 3.2 (bottom) also summarizes the results for the individual self-diffusion coefficients in system IVa. Compared with the dilute electrolyte systems II and III, the diffusion coefficients of both ions and solvent are substantially decreased. Overall this is a consequence of the higher viscosity of system IVa and ion pairing. The temperature-dependence of ionic diffusion is presented in Fig 3.6, which shows an Arrhenius plot

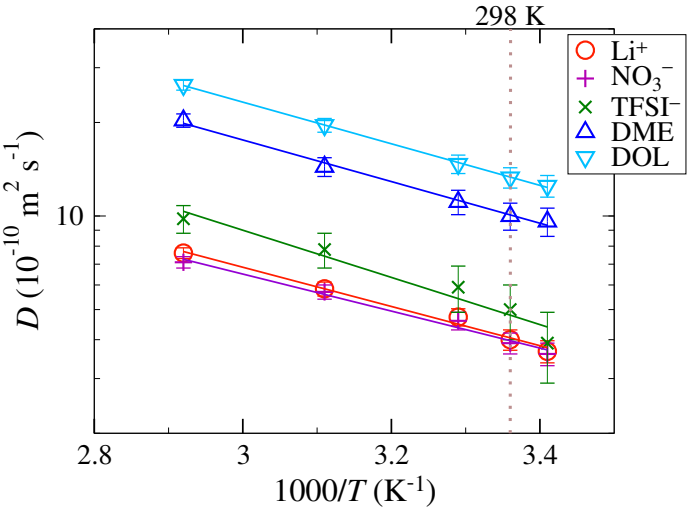

Figure 3.6: Diffusion coefficients of ions and solvent molecules in system IVa as a function of inverse temperature in a log-lin representation. They all obey the Arrhenius behavior given by Eq. 3.3. The vertical dotted line indicates $T = 298$ K.

for the diffusion coefficients according to the standard law

$$D(T) = D_0 \exp\left(-\frac{\Delta E_\mathrm{a}}{k_\mathrm{B} T}\right), \tag{3.3}$$

where ΔE_a is the activation energy for diffusion. The individual fitting parameters $\ln D_0$ and ΔE_a are summarized in Table 3.3. As can be seen, the diffusion (*i.e.*, ionic mobilities in these experimentally relevant systems) can increase almost by a factor 2 or 3 when going from room temperature to relatively hot operating temperatures close to the solvent boiling temperatures (358 K for DME and 347 K for DOL).

We finally turn to the structural description of system IVa. A snapshot of a representative configuration in the first solvation shell of Li^+ is exemplified in Fig 3.7(a). The RDFs between the center-of-mass of the individual anions and solvent molecules around a Li^+ ion are presented in Fig 3.7(b) in a log-lin representation. A distinct solvent composition and layering within the first solvation shell is exhibited. At closest distance is the DME solvent at about 0.165 nm, followed by a large nitrate peak at about 0.25-0.3 nm and the DOL at about 0.3 nm. The large $TFSI^-$ has its center-of-mass a bit more outwards, peaking at about 0.42 nm. The first solvation shell according to these distributions has a radius of about 0.5 nm (see also Figs A.4 in Appendix). This running coordination number of the molecules around the Li^+ ion is displayed

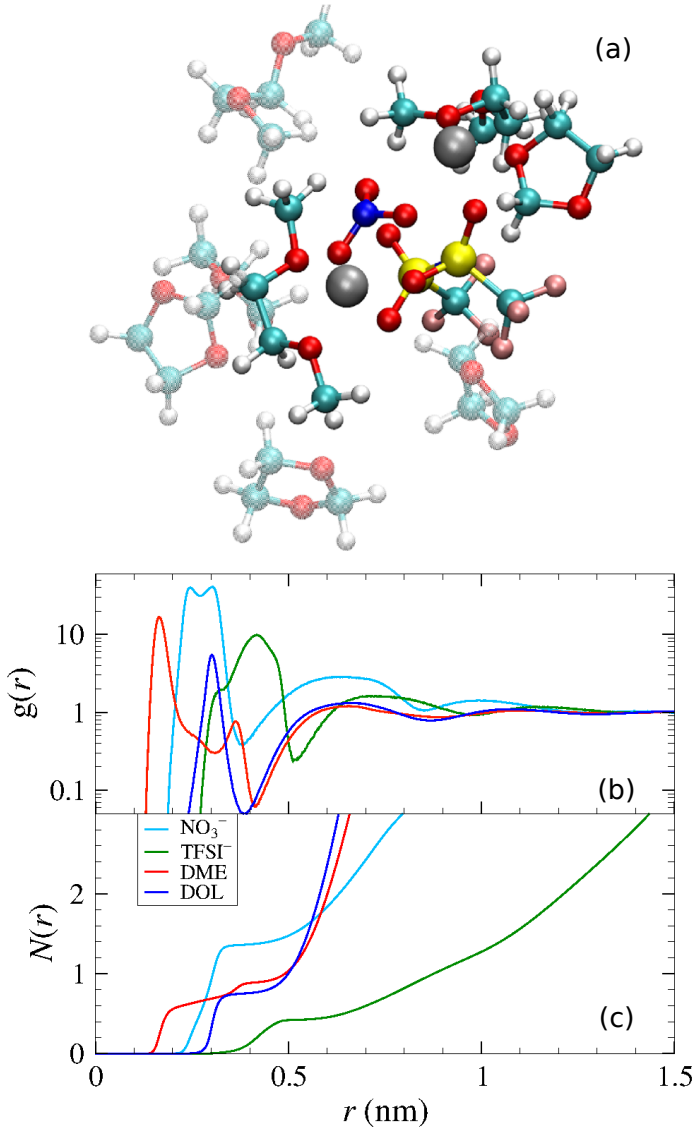

Figure 3.7: (a) Simulation snapshot of molecules surrounding Li^+ ions (gray spheres) in their first solvation shell in system IVa. (b) Center-of-mass RDF $g(r)$ and (c) the coordination number $N(r)$ of ions and solvent molecules around a single Li^+ ion as a function of distance r in system IVa. Note the log-lin presentation in panel (b).

in panel (c) of the same figure. The coordination numbers in the first solvation shell (*i.e.*, within $\simeq 0.5\,\mathrm{nm}$) are about 1.1 for DME, 0.7 for DOL, 1.3 for NO_3^-, and 0.1 for $TFSI^-$, on average. Altogether this makes 3.2 molecules in the first solvation shell. Most qualitative structural features of system IVa thus resemble those of the dilute systems discussed before (see also Figs A.4 in Appendix) which, for instance, show a similar structure of RDFs between system IIa and IVa.

3.3 Summary and concluding remarks

In this chapter, we constructed an efficient molecular model for state-of-the-art battery electrolytes used in metal-sulfur or metal-air batteries and solvents that reproduces a variety of experimentally observable structural and dynamical features. We verified it at hand of various reference systems, in particular in those limits where neat experimental data was available. For example, the density, dielectric constant, viscosity, and diffusion coefficient of solvent mixtures DME/DOL are satisfactorily reproduced for all molar ratios. The Li^+ solvation structure and pair association with NO_3^- and $TFSI^-$ anions in DME was found consistent with experimental data. The ion mobility and conductivity in 1:20 salt–solvent systems as well agreed with experimental measurements. Finally, the physical properties, such as Li^+ solvation environment and diffusivity of the full state-of-the-art Li/S battery electrolytes were in detail investigated and gave unprecedented structural insight in the composition of the important first lithium solvation shell. Apart from the fundamental insights provided, our model will thus serve as a basis for efficient future calculations of electrolyte structure, conductivity, capacity, etc. for various electrolyte solvent compositions in porous electrode confinements and interfaces and with that as a guidance for the development of modern Li/S batteries and related systems.

4 Structural and transport properties of the Polysulfide Species

4.1 Introduction

In previous chapter, we devised the force field for the electrolyte and successfully demonstrated the detailed composition of the first lithium solvation shell and the transport properties, such as diffusion, conductivity and transference numbers. In this chapter, we make a step further towards more realistic solutions and include the most relevant PS chain lengths of 4, 6, and 8 sulfur atoms [182] into the model to elucidate the intrinsic properties of PS.

PS shuttling, which is the major bottlenecks of the Li/S battery development, is caused by intermediate PS species (Li_2S_x, x=4∼8) because they are soluble in the electrolyte. The stability or the reaction mechanism pathway of the intermediate species can be altered by the type of solvent, added electrolyte [183, 19, 184, 185], current density, and temperature [186]. It is thus of utmost importance to obtain deeper understanding into the structural and transport properties of these highly complex, multi-component PS solutions.

We develop a working model for PS of different chain lengths in electrolyte solutions of LiTFSI in DME and DOL. We investigate conductivities, diffusion coefficients, solvation structures, and clustering behavior, and verify our simulation model with experimental measurements available in the literature and newly performed by our experimental collaborators from IEES at HZB.

4.1.1 Force fields

The solvent in our atomistic model is a 1:1 molar mixture of DME and DOL, which contains different amounts of Li^+ and $TFSI^-$ as well as three different kinds of PS ions:

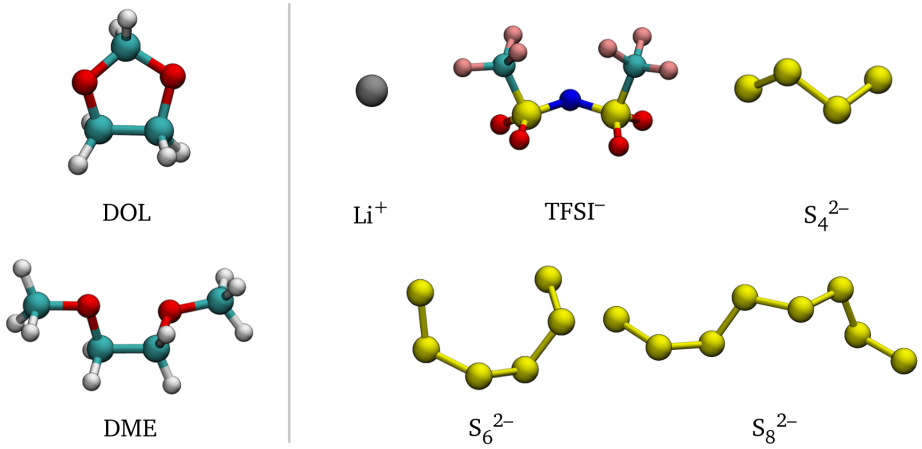

Figure 4.1: Solvent molecules DOL and DME and ions Li^+, $TFSI^-$, and PS with chain lengths $x = 4$, 6, and 8 considered in this study.

S_4^{2-}, S_6^{2-}, S_8^{2-} (see Fig 4.1). The Coulomb interactions of ions are treated by the ECC method in Eq 3.2.

We devote special attention to the parametrization of the PS ions. The bonded parameters for PS ions are taken from the recent work by Rajput *et al.* [98] In order to obtain the partial charges, we performed quantum mechanical calculations using the electrostatic potential surface method implemented in the GAUSSIAN09 package [187] with the B3LYP functional at the aug-cc-pvdz basis set level. The resulting (unscaled) and the corresponding effective (rescaled via Eq 3.2) partial charges of sulfur atoms in PS are summarized in Table 4.1.

Table 4.1: Formal (q_i) and effective (q_i^{eff}, computed via Eq 3.2) partial charges of terminal and internal S atoms in the PS chains. e is the elementary charge.

	Terminal S		Internal S	
	q_i / e	q_i^{eff} / e	q_i / e	q_i^{eff} / e
S_4^{2-}	−0.7702	−0.5546	−0.2298	−0.1655
S_6^{2-}	−0.6537	−0.4707	−0.1731	−0.1247
S_8^{2-}	−0.6223	−0.4481	−0.1259	−0.0907

Different LJ parameters for S atoms have been tested using various force fields: OPLS-AA [115], AMBER99 [188], CHARMM [189], ENCAD [190], ECEPP [191], UFF [192]

and DREIDING [193] (see Table A.5 in Appendix). As it turns out, the LJ interaction size σ_{S-Li^+} between a terminal S atom and Li^+ is a critical parameter that determines the degree of aggregation and clustering propensities, as well as conductivity of PS ions. Therefore, we tuned the LJ parameter manually to $\sigma_{S-Li^+} = 0.275$ nm in order to reproduce experimental conductivity values. The procedure and the details are provided in Figures A.5 and A.6 in Appendix.

4.2 Results

4.2.1 Density and dielectric constant

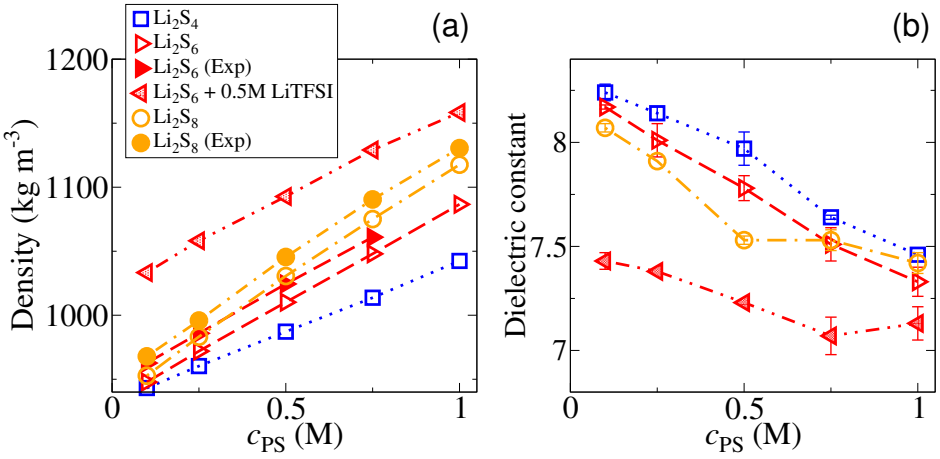

Figure 4.2: (a) Density and (b) dielectric constant as a function of the polysulfide concentration in DME/DOL (1:1) solvent in MD simulations. The experimental measurements for Li_2S_6 and Li_2S_8 are depicted by solid triangles and circles in panel (a).

We start our analysis by calculating the density of various PS in DME/DOL solutions, results of which are plotted in Fig 4.2a. Universally, the density is an increasing function of the Li_2S_x concentration for all PS types. This rise and the magnitude is in good accordance with our experimental measurements for Li_2S_6 and Li_2S_8 (solid triangles and circles, respectively, in Fig 4.2a). Note that in our simulations we only consider one-component (i.e., monodisperse) PS solutions. In reality, however, the monodispersity cannot be reached due to the disproportionation reactions of PS, but the majority of the PS should appear in the length as prepared [194].

The dielectric constant as a function of Li_2S_x concentration is shown in Fig 4.2b. It decreases with ion concentration, as is also the case in other electrolytes [195, 196, 197, 198]. This decrement of the dielectric constant is caused by a local dielectric saturation. Namely, solvent molecules tend to strongly orient and anchor around an ion and do not contribute to the dielectric constant. As more ions are present in the solution, larger fraction of solvent molecules are part of the solvation shells of the ions and thus larger is the local dielectric saturation. The dielectric decrement is slightly larger for longer PS chains. The addition of 0.5M LiTFSI into the Li_2S_6 solution decreases the dielectric constant considerably, which can be also explained by the local dielectric saturation due to added ions into the solution.

4.2.2 Solvation structure and radial distribution functions (RDFs)

In the following, we take a look at the solvation structure of Li^+ ions. Figure 4.3 shows RDFs of various molecules and Li^+ ions in DME/DOL [panels (a–c)] and in DME/DOL with 1M LiTFSI [panels (d–f)]. The top two panels (a, d) show the distribution of terminal S atoms (S_{ter}) of PSs. The very high first peak in all the cases indicates a strong binding affinity between Li^+ and PS ions and can be attributed to the electrostatic attraction between Li^+ and ${S_x}^{2-}$. Moreover, the height of the peak, and with that the binding strength, are diminishing with the length of the PS ions (when going from ${S_4}^{2-}$ to ${S_8}^{2-}$). These trends are consistent with a recent classical MD simulation study [98]. This can be explained by stronger charge localization (of the net valency -2) at terminal ends of shorter PS ions [199]. As seen in Table 4.1, shorter chains have higher partial charges at the termini, thus facilitating the attraction with Li^+. Furthermore, the geometry of the PS chains also plays a role in the solvation shell. Snapshots in Figures 4.4a, c, e show that short PS chains (e.g., ${S_4}^{2-}$) are able to tightly wrap around a Li^+ ion. Conversely, longer PS chains (e.g., Li_2S_6 and Li_2S_8) do not pack so tightly around the Li^+.

The different binding strengths result into different compositions of the Li^+ solvation shell, which can be described by coordination numbers in Fig 4.5. Namely, shorter PS

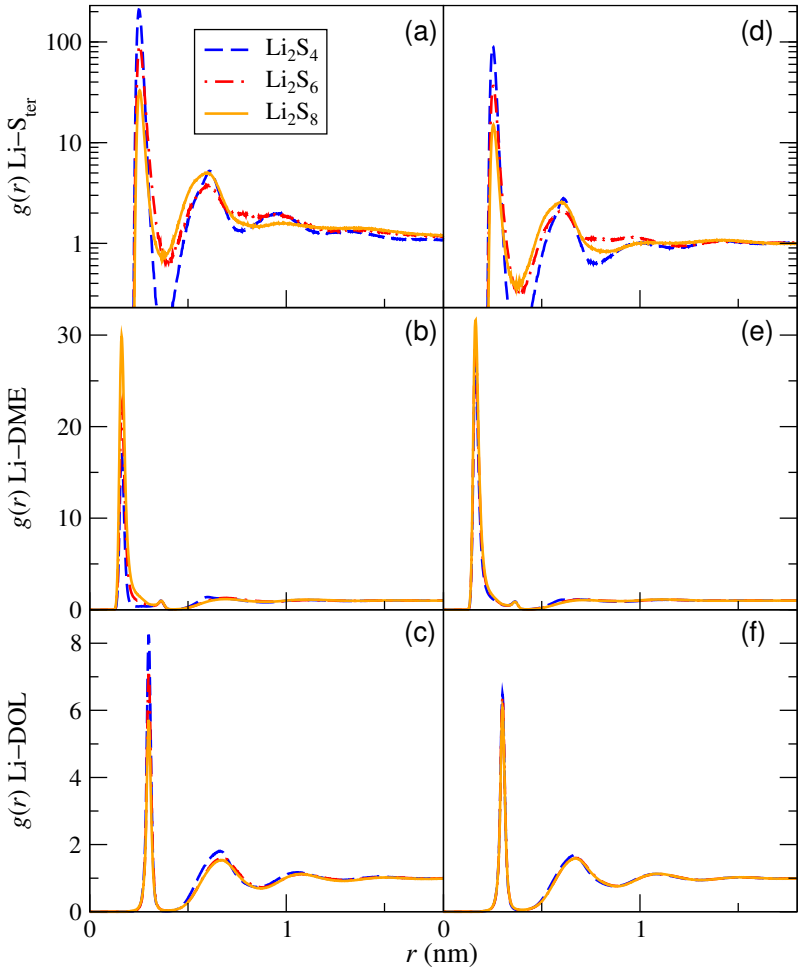

Figure 4.3: Radial distribution functions (at 0.25 M Li_2S_x) between Li^+ and (a, d) terminal S (S_{ter}) in S_x^{2-} (x = 4, 6, and 8), (b, e) DME and (c, f) DOL in DME/DOL (a–c) and in DME/DOL with 1M LiTFSI (d–f).

chains drive out other molecular species from the first hydration shell of Li^+ [panels (a–d)]. Due to this PS packing in the first solvation shell of Li^+, fewer DME or DOL molecules can populate the surrounding of Li^+ in the presence of Li_2S_4 than in the cases of Li_2S_6 or Li_2S_8 (lower peak in $g_{Li^+–DME}(r)$ in the case of Li_2S_4 than in Li_2S_8 in Fig 4.3b). The DME coordination number of Li^+ in Fig. 4.5 increases from Li_2S_4 to Li_2S_8. *Ab-initio* MD simulations by Kamphaus [199] also showed similar trends. This densely packed solvation structure by S_4^{2-} gives less chance for Li^+ in the solvation shell to contact with solvent molecules. It restricts the Li^+ exchange between S_4^{2-} and solvent molecules, resulting in lower solubility [200, 199].

Now we investigate the effects of LiTFSI in the solution. Figure 4.3d shows that the

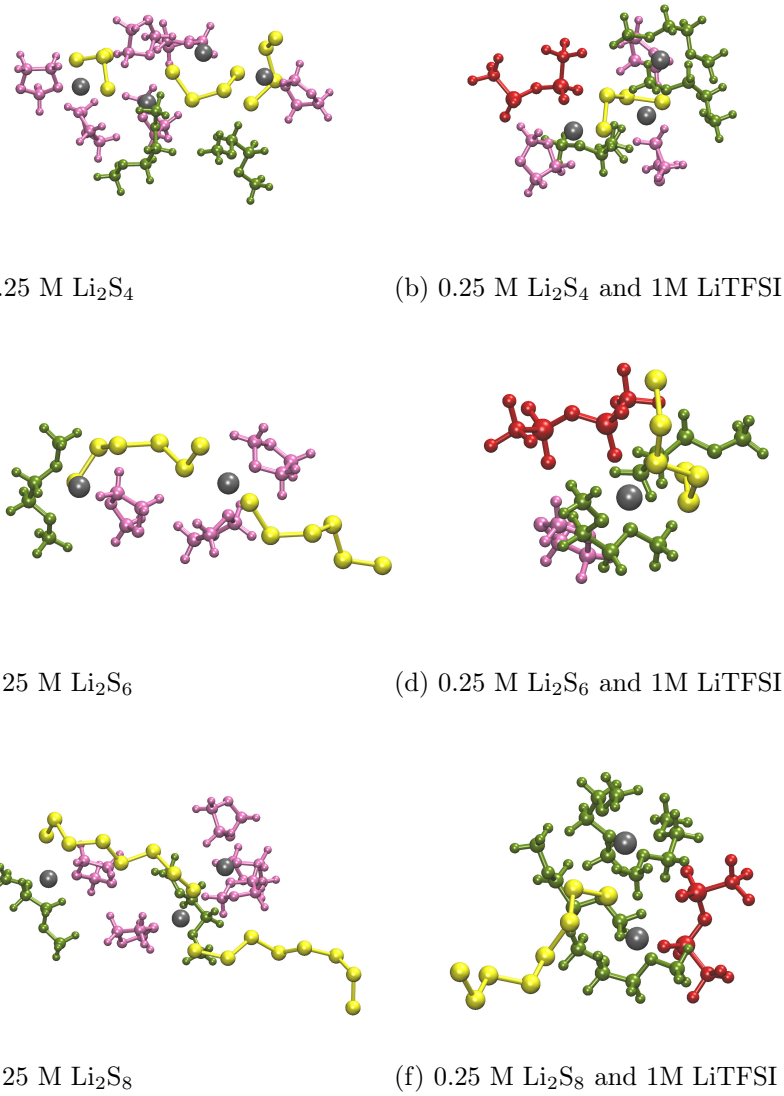

(a) 0.25 M Li_2S_4

(b) 0.25 M Li_2S_4 and 1M LiTFSI

(c) 0.25 M Li_2S_6

(d) 0.25 M Li_2S_6 and 1M LiTFSI

(e) 0.25 M Li_2S_8

(f) 0.25 M Li_2S_8 and 1M LiTFSI

Figure 4.4: Snapshots of Li^+ solvation shell in DME/DOL and different amounts of ions. Color code: Li^+ (gray), $S_x{}^{2-}$ (yellow), $TFSI^-$ (red), DME (green), DOL (pink).

magnitudes of the main peaks in $g_{Li^+-S_x{}^{2-}}(r)$ decrease after 1 M of LiTFSI is added (cf. panel a), as also consistent with previous studies [98] (also see $g_{Li^+-TFSI^-}(r)$ in Fig A.7. An important insight can be gained from the Li^+ coordination number around a PS molecule shown in Fig 4.5e. Evidently, the number of Li^+ ions around S termini does not change upon introducing LiTFSI into the system. This means that LiTFSI does neither weaken the Li^+–PS bonds nor do additional Li^+ ions from LiTFSI bind to PS. Thus the decrease in the RDF peaks (4.3d) and the different solvation shell composition

(Fig 4.5d) arrive on the expense of the added Li^+ ions.

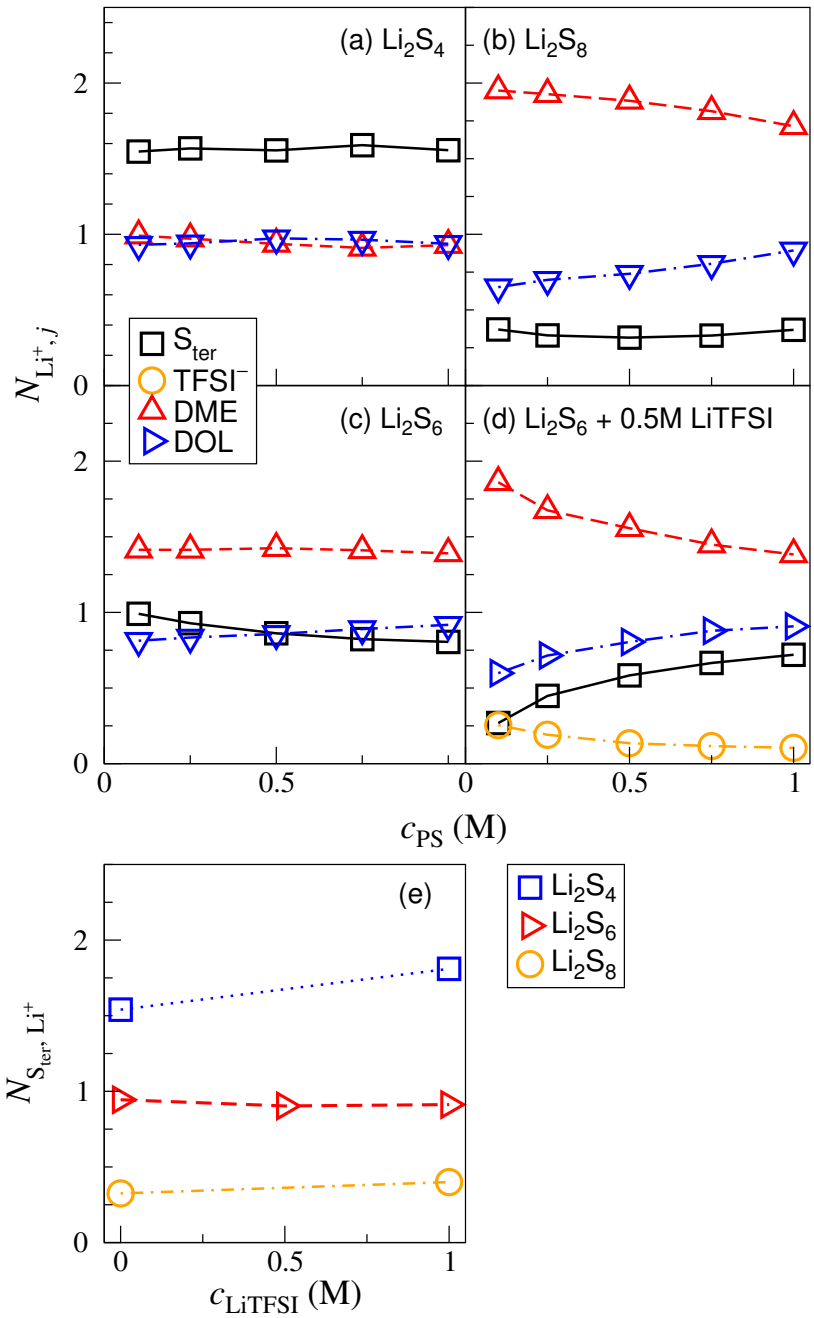

Figure 4.5: (a–d) Coordination numbers of molecules j around the Li^+ ion ($N_{Li^+,j}$) as a function of the polysulfide concentration (see legend). (e) Li^+ coordination number around S_{ter} (N_{S_{ter},Li^+}) as a function of LiTFSI concentration.

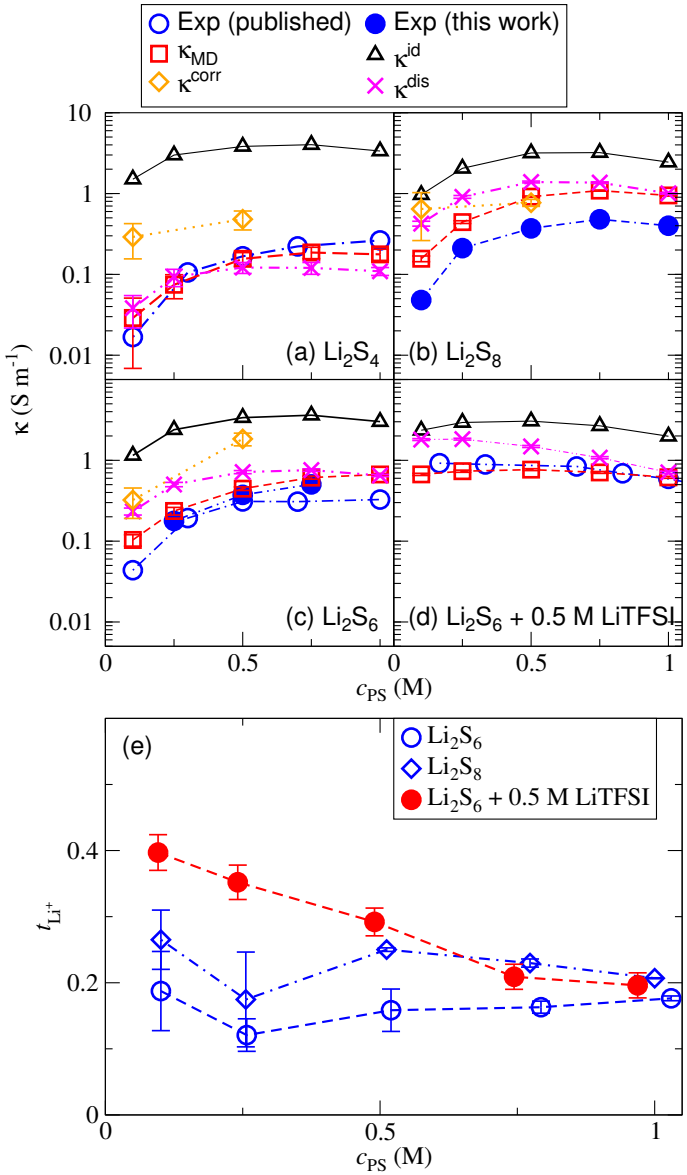

Figure 4.6: (a–d) Conductivities from MD simulations (squares, triangle left and right), experimental measurements (circles) and the ideal ionic conductivity assuming Eq 4.1 (triangles up) as a function of the polysulfide concentration. (a) Li_2S_4; exp. by Safari *et al.* [16], (DME/DOL) (b) Li_2S_8; exp. by us (DME/DOL), (c) Li_2S_6; exp. by Safari *et al.* [16] (empty circles) and by us (filled circles) (DME/DOL). (d) Li_2S_6 + 0.5 M LiTFSI; exp. by Fan *et al.* [20] (0.5 M LiTFSI DME/DOL). Diamonds in panels (a), (b) and (c) are κ^{corr} using Eq 4.2. Crosses in panels (a), (b), (c) and (d) are κ^{dis} using Eq 4.3. (e) Estimated Li^+ transference number from MD for different Li_2S_x concentrations (with/without LiTFSI).

4.2.3 Conductivity

In Fig 4.6 we show the ionic conductivity from the MD simulations and experimental measurements (ours, by Safari *et al.* [16], and by Fan *et al.* [20]) for PS concentrations in the range of 0.1–1M. As seen, the experimental trends of the four studied systems

(LiS_4, LiS_6, LiS_8, and LiS_6+0.5M LiTFSI) are well captured by the simulations. In cases of Li_2S_6 and Li_2S_8, the conductivities are by a factor of three higher than in experiments. Nevertheless, we regard the results satisfactory as these quantities are extremely sensitive to the molecular interactions and thus prone to large errors, sometimes of more than an order of magnitude. The conductivities from the simulations for the ternary electrolytes of Li_2S_6 + LiTFSI are also congruent with experiments, capturing even the saturation and the decrease in the conductivity with increasing PS concentration above 0.5 M.

Ideal ionic conductivity in the limit of low concentrations is given by the Nernst–Einstein (NE) equation

$$\kappa^{\mathrm{id}} = \frac{e^2}{k_{\mathrm{B}}T} \sum_i z_i^2 c_i D_i, \tag{4.1}$$

where z_i stands for the ion valency and c_i for the ion concentration of species i. Using the diffusivities D_i obtained from the simulations, we calculate the ideal conductivities in Fig 4.6 (triangles). Clearly, the values are an order of magnitude too high, which we attribute to substantial ionic pairing [20, 201]. Namely, Eq 4.1 is a limiting law and thus neglects ion–ion correlations.

In a first-order correction to the ideal conductivity, the correlations can be perturbatively taken into account, which leads to [202]

$$\kappa^{\mathrm{corr}} = \kappa^{\mathrm{id}} + \frac{2e^2}{3\eta} \sum_{i,j} z_i z_j c_i c_j \int_0^\infty h_{ij}(r) r \mathrm{d}r \tag{4.2}$$

where η is the solvent viscosity. Here, the ion–ion correlation effects are expressed via $h_{ij}(r) = g_{ij}(r) - 1$. Equation 4.2 thus constitutes a useful structure–transport relationship, applicable at least for not too dense solutions. Taking $h_{ij}(r)$ from our simulations, we plot the correlation-corrected values κ^{corr} as diamond symbols in Fig 4.6. Evidently, the negative effect of ionic pairing is qualitatively captured by the correlation term and the values approach closer the MD results. Among all the contributing ion pairs to the second term in Eq 4.2, the most of contribution comes from the Li^+–$S_x{}^{2-}$ pair (see $\int_0^\infty h_{ij}(r) r \mathrm{d}r$ values in Table A.6 in Appendix). This means that the strong binding between the latter two ions is the main culprit for the observed low conductivity. Still,

the correlation correction given by Eq 4.2 cannot provide a fair quantitative agreement with the measured values and hence we conclude that even at lower concentrations already correlations beyond the pair level are important, *e.g.*, from clustering effects, see further below.

Thus, in the limit of very strong ion pairing, where most of the ions are associated into neutral ion pairs and clusters, we can expect that only the dissociated ions contribute to the conductivity. In this simplified picture, we replace ionic concentrations c_i in the NE equation (4.1) by the concentrations of dissociated ions, $\omega_i c_i$,

$$\kappa^{\mathrm{dis}} = \frac{e^2}{k_{\mathrm{B}}T} \sum_i z_i^2 \omega_i c_i D_i, \tag{4.3}$$

where ω_i stands for the fraction of dissociated ions of type i. For simplicity of our treatment, we assume that only Li^+ and PS ions are involved in pairing, whereas $TFSI^-$ ions are completely dissociated, $\omega_{TFSI^-} = 1$, as they only weakly bind with Li^+. Li^+ and PS species are subject to the following equilibrium

$$Li_2S_x \rightleftharpoons Li^+ + (LiS_x)^-. \tag{4.4}$$

We assume that further dissociation into $2\,Li^+ + S_x{}^{2-}$ is much less probable and we neglect it.

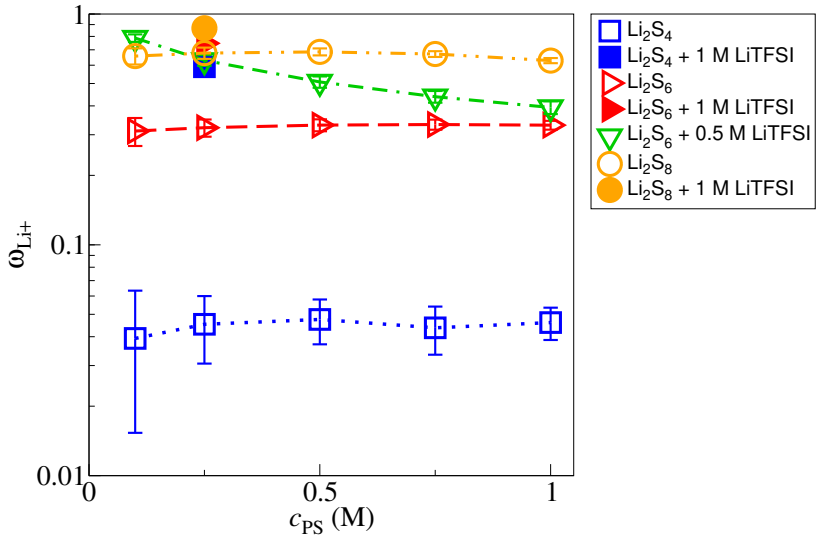

Figure 4.7: Fraction of dissociated Li^+ ions as a function of the polysulfide concentration in different solutions. It is defined as the fraction of the Li^+ population without PS ions in their hydration shells.

Figure 4.7 shows the fraction of dissociated Li^+ in various solutions, defined as the population of those Li^+ ions that do not have PS in their hydration shells. The dissociation is by far the lowest for Li_2S_4 and higher for Li_2S_6 and Li_2S_8, similar trends are also observed by a recent study [99]. Adding LiTFSI increases the dissociated degree noticeably, which implies that the additional lithium from LiTFSI remains more or less dissociated. In cases without LiTFSI, the effective concentrations of Li^+ and $(LiS_x)^-$ species are both equal to $2c_{\mathrm{PS}}\omega_{\mathrm{Li}^+}$. Introducing LiTFSI adds equivalent concentrations of c_{TFSI^-} to Li^+ as well as $TFSI^-$ species, since the added Li^+ are all dissociated. Thus, the modified NE equation then reads

$$\kappa^{\mathrm{dis}} = \frac{e^2}{k_{\mathrm{B}}T}\left[(2c_{\mathrm{PS}}\omega_{\mathrm{Li}^+} + c_{\mathrm{TFSI}^-})D_{\mathrm{Li}^+} + 2c_{\mathrm{PS}}\omega_{\mathrm{Li}^+}D_{\mathrm{PS}} + c_{\mathrm{TFSI}^-}D_{\mathrm{TFSI}^-}\right]. \tag{4.5}$$

Note that all the species in this treatment are monovalent, therefore $z_i^2 = 1$. In Fig 4.6a–d, we plot the conductivities κ^{dis} from Eq 4.5 (cross symbols), which in most cases approach much closer to the experimental and MD results than the other two theoretical approaches.

Finally, all three theoretical approaches help us to elucidate the conductivity mechanism of Li_2S_x solutions. Due to high Li–PS pairing, most of the ion carriers are 'neutralized' and do not contribute to the conductivity. Only the associated fraction acts on the external electric field, which results into an electric current. When LiTFSI salt is added, it contributes mostly dissociated Li^+ and $TFSI^-$ ions and therefore fully contribute to the conductivity, which also explains the almost constant trend in Fig 4.6d.

As reported by Zheng *et al.* [203] a practical sulfur/electrolyte (S/E) ratio (i.e., density of sulfur in electrolyte) with improved cycling stability and Coulombic efficiency are achieved for S/E ratio of $50\,\mathrm{g\,L^{-1}}$. This corresponds to approximately 0.4 M Li_2S_4 in our systems for a complete conversion of all sulfur into Li_2S_4. Above this concentrations, the saturation of the conductivity caused by increasing ionic pairing and viscosity can be one of the limiting factors [20] for using the high S/E ratio solutions.

Sue *et al.* [18] reported that, in solvent-in-salt systems, high viscosity and incomplete

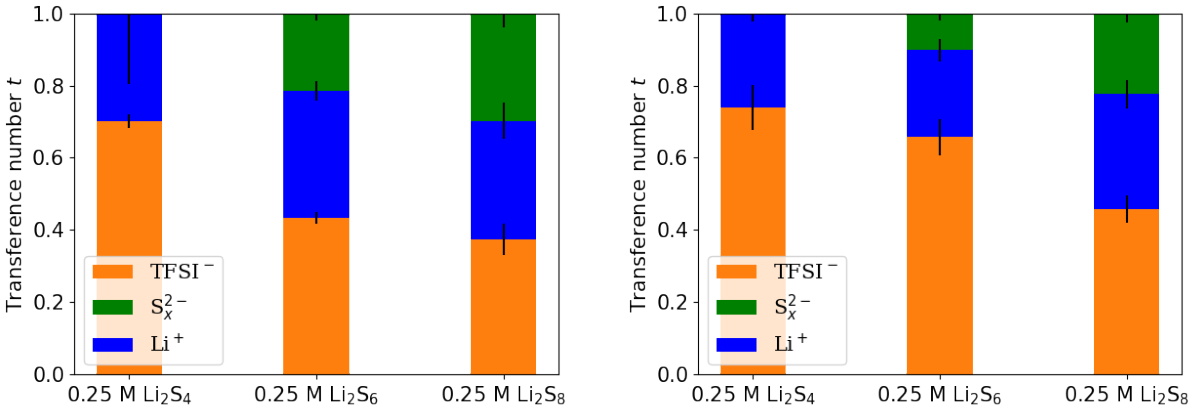

(a) 0.25 M Li_2S_x + 0.5 M LiTFSI.

(b) 0.25 M Li_2S_x + 1 M LiTFSI.

Figure 4.8: Transference numbers for Li^+, $TFSI^-$, and $S_x{}^{2-}$ in different polysulfide solutions.

solvation shell facilitate higher Li^+ transference number ($t_{Li^+} = J_{Li^+}/J$), which is unlike in conventional salt-in-solvent electrolytes. In our system, the Li^+ transference number does not increase with Li_2S_x concentration (see Fig 4.6e). Instead, it stays around 0.2 for a wide range of PS concentrations without LiTFSI (as also demonstrated experimentally [16]). The low value can be explained by the fact that Li^+ ions are mostly moving collectively together with PS ions. The constant value of the transference number is also in accordance with the weak dependence of coordination numbers on PS concentrations. Expectedly, with 0.5 M LiTFSI t_{Li^+} increases, since additional Li^+ that come from LiTFSI are not bound to PS and contribute to the conductivity to a greater extent. In the latter case, the contribution of PS to conductivity becomes negligible, as evident from the low PS transference number in the presence of LiTFSI (see Fig 4.8a and b). Again, due to the strong binding between Li^+ and $S_4{}^{2-}$, Li_2S_4 behaves as a neutral species and is therefore not subject to the electric field. We presume that these short PS chains are more likely to participate in the shuttle mechanism during the charge.

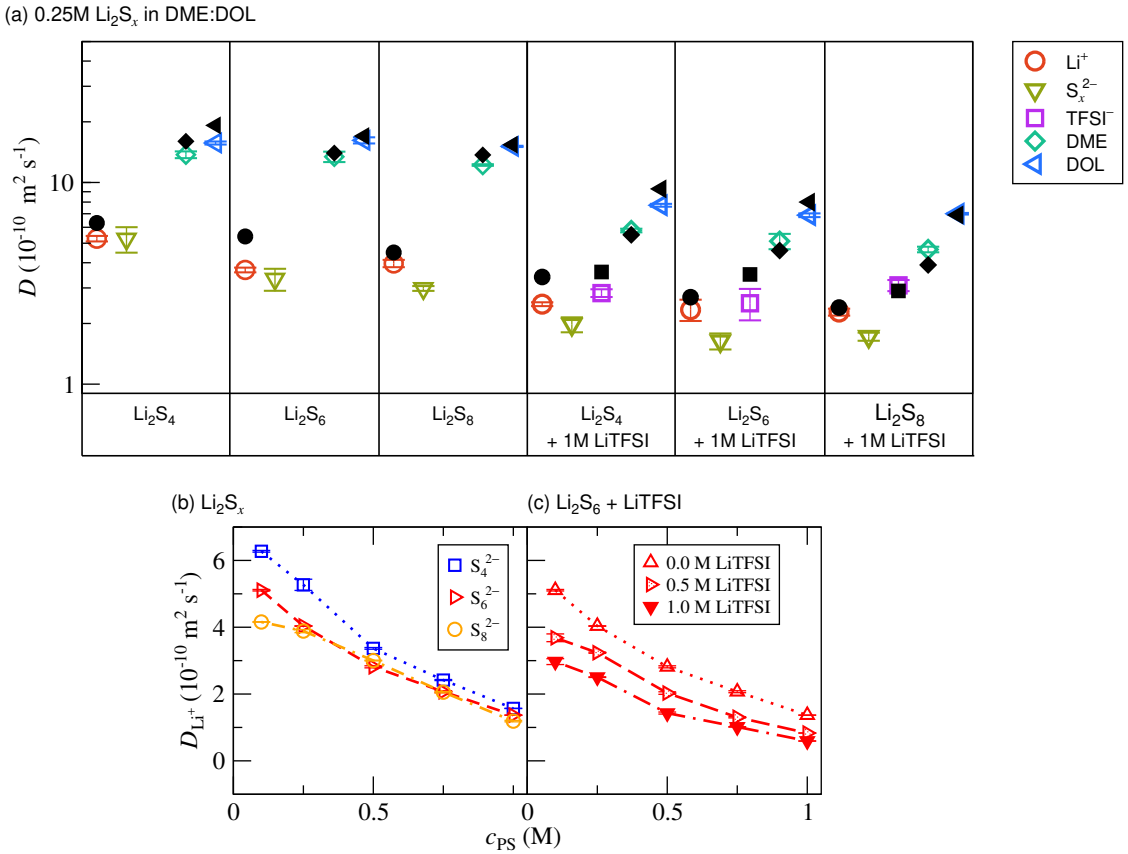

Figure 4.9: (a) Long-time self-diffusion coefficients D of all species in the 0.25 M of the polysulfide as obtained from MD simulations (empty symbols) and PFG-NMR measurements (black filled symbols) [98]. (b) Diffusion coefficients of Li^+ in different PS solutions as a function of the PS concentration from MD simulations. (c) Diffusion coefficients of Li^+ as a function of Li_2S_6 concentration in the presence of different amounts of LiTFSI from MD simulations.

4.2.4 Diffusion coefficients

Evaluating the long-time mean square displacement, we now compute the self diffusion coefficients of all the species in our system. The diffusion coefficients from MD simulations are compared with measured values from PFG-NMR [98] in Fig 4.9a, which suggests fair agreement. At this point, we remark that without the ECC treatment of ionic charges, the MD results would deviate from the experiments by an order of magnitude as we demonstrate in Fig A.8 in Appendix. Namely, without ECC, the PS–Li^+ binding is unrealistically strong and thus exaggerates the ion-pair formation [204, 119, 120, 118].

Shorter PS chains (S_4^{2-}) diffuse faster than longer ones (such as S_6^{2-} and S_8^{2-}), which

can simply be explained in terms of the Stokes–Einstein relations, where the diffusion coefficient is inversely proportional to the particle's effective size. We furthermore notice (Fig 4.9a) that the diffusion coefficients of Li^+ and S_x^{2-} in the solvent (without $TFSI^-$ ions) are of the same order. This can be related to collective diffusion of S_x^{2-} and Li^+ ions due to their strong association. As we increase the PS concentration, the Li^+ diffusivity monotonically decreases (Fig 4.9b), as also demonstrated experimentally [16]. This effect can be ascribed to an increasing viscosity in more concentrated PS solutions (Fig A.9a in Appendix). At low concentrations of PS, the diffusion coefficient of Li^+ significantly depends on the PS type. Namely, shorter PS (Li_2S_4) promotes higher diffusion than longer PS (Li_2S_6 and Li_2S_8). Yet, this differences disappear at higher concentrations of PS (above around 0.5 M). Interestingly, adding 1 M LiTFSI reduces the diffusion up to about 50% (Fig 4.9a, c), as also reported in a previous simulation study [98]. Also this effect can be attributed to an increased viscosity when LiTFSI is added (see Fig A.9b in Appendix). The estimated viscosity of Li_2S_6 in DME/DOL with 1M LiTFSI is about a factor of three higher than without LiTFSI. As we have seen, viscosity plays a critical role in ionic transport in the PS solutions. Introducing LiTFSI into dilute PS solutions increases the number of dissociated Li^+ and leads to a higher conductivity (Fig 4.6). Yet, this ionic effect fades out compared to an increasing viscosity at high PS concentrations.

4.2.5 Clustering

Due to the high attraction between terminal sulfur ends of PS and Li^+ ions, occasionally two different PS ions can bind to the same Li^+ ion, such that the Li^+ ion represents a "bridging" element for the two PS ions. This can result into supramolecular clusters that are composed of several PS chains and Li^+ ions. Figure 4.10 shows the cluster-size distribution $P(N)$ of PS in log–lin presentation. As seen, the clusters do not have a characteristic size but are extremely polydisperse and roughly follow an exponential distribution $P(N) \sim \exp(-N/\overline{N})$, where $\overline{N}$ is the mean size of the clusters [205]. Some deviations from the exponential behavior occur for larger clusters at higher concentra-

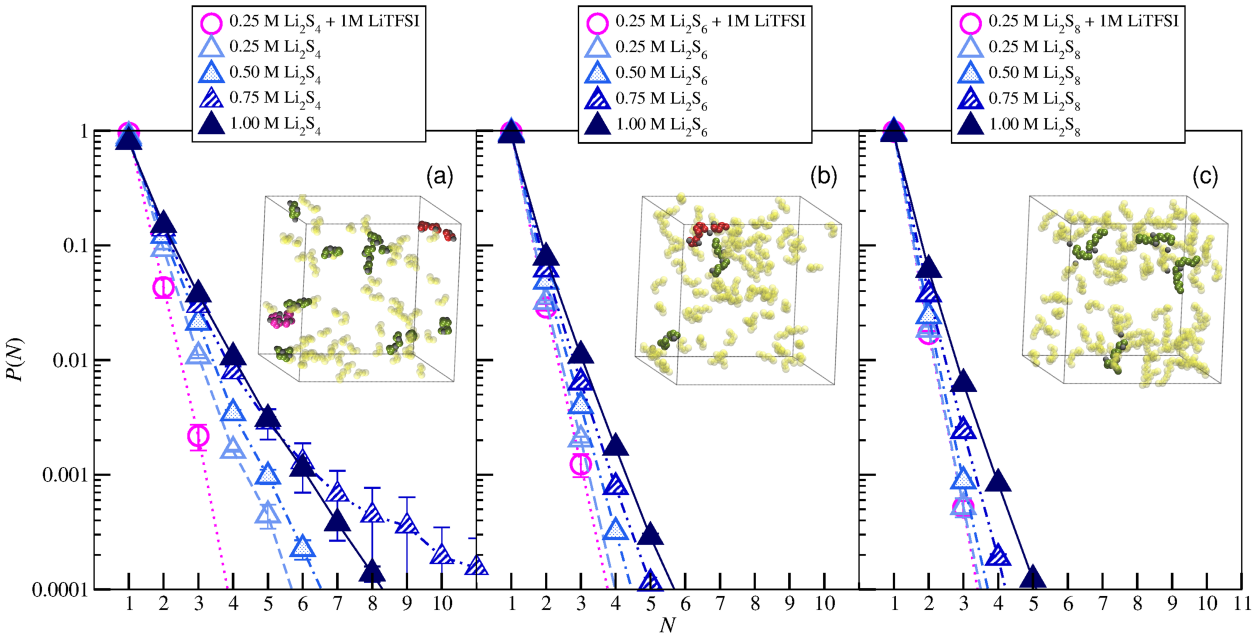

Figure 4.10: Cluster size distributions for (a) Li_2S_4, (b) Li_2S_6, and (c) Li_2S_8 in DME/DOL. Insets show representative simulation snapshots of 0.25 M of the polysulfide. Clusters of different sizes are shown in different colors: yellow ($N = 1$), green ($N = 2$), pink ($N = 3$), and red ($N = 4$).

tions, suggesting a cooperative binding. Yet, the cluster size distribution indicates that single monomers and small PS clusters prevail.

Clearly, higher concentrations of PS increase the proportion of larger clusters, simply because the probability of different PS chains to meet is higher in a more concentrated solution. Even higher concentrations, approaching the solubility limit (not shown), thus provide critical nucleation sites for formation of large cluster precipitates. The morphology of the cluster may thus depend on the growth and nucleation rates [203].

Moreover, comparing the clustering of different PS lengths reveals that the shorter PSs tend to form larger clusters more readily, especially at high concentrations, compared with longer PSs. A higher frequency of clusters up to 80 atoms was also observed recently for the shorter chains (S_4^{2-}) when compared to the longer ones [99]. The reason lies in the stronger charge localization at S termini in shorter PS chains, as already discussed above. These results are in line with Vijayakumar *et al.* [152] who reported that Li_2S_4 favors dimer formation, whereas Li_2S_8 favors monomer formation in dimethyl sulfoxide solvent, while Li_2S_6 being somewhere in between. Representative simulation snapshots are shown in the insets of Fig 4.10, featuring larger cluster formation in the

case of Li_2S_4 than in the other two cases. Note that even shorter PS chains, like S_2^{2-}, are even less soluble in the existing solvent and tend to precipitate out of solution even at very low concentrations [194, 206, 207] (see Figures A.10 for the analysis of S_2^{2-} and Fig A.11 for snapshot in Appendix).

Interestingly, adding 1M of LiTFSI inhibits the clustering for Li_2S_4 (Figures 4.10a–c), as also reported before [98, 208]. This can, however, not be claimed for the other two PS species. As discussed above, the presence of LiTFSI does not significantly influence the Li^+–PS binding as seen from coordination numbers of S_{ter}. However, it apparently tends to inhibit cluster formation via other mechanisms, such as increased electrostatic screening due to LiTFSI ions. This influence of the ionic strength on the Li–PS network also impacts the shuttle effect in Li/S batteries [199, 49]. Sustaining the Li–S networks by using low ion-pairing salt, can decrease the shuttle effect and increase the cycle performance of the batteries [209, 210].

4.3 Summary and concluding remarks

We developed an atomistic model for PS in an organic functional solvent that is currently in use for the development of Li/S batteries. We focused particularly on structural and dynamic properties of three different sizes of PS ions, S_4^{2-}, S_6^{2-}, S_8^{2-} in the presence of Li^+ and $TFSI^-$ ions. The conductivity and diffusion coefficients of PS solutions are validated by experimental measurements. Conductivities of PS solutions first exhibit an increase with the Li_2S_x concentrations and eventually a saturation at around 0.5 M. The saturation in the conductivity can be linked to viscosity and the ionic correlations between PS and Li^+, which also lead to occurrence of supramolecular clusters. The tendency of clustering increases with the concentration of Li_2S_x and is more pronounced for shorter PS ions (i.e., $x = 4$). Shorter chains have their electronic density more strongly localized at the terminal sulfur atoms than longer chains, thus facilitating the electrostatic attraction with Li^+.

The addition of $TFSI^-$ ions leads to larger amount of dissociated Li^+ ions and to a noticeable increase in the viscosity. The dissociated Li^+ contributes to the conductivity

considerably, on the other hand, increased viscosity inhibits the conductivity at larger PS concentrations. The presence of LiTFSI also reduces cluster formation of shorter PS ions. Even though TFSI ions do not significantly reduce the Li^+–PS binding, they weaken the binding between multiple PS ions into clusters, partially because of a higher ionic strength. Thus, LiTFSI increases the solubility of PS ions and with that enhances the shuttle effect in the Li/S batteries.

Our simulation results of PS solutions reveal that structural and transport properties are subject to subtle interactions among ions and solvents molecules, which should be considered carefully when it comes to the design of electrolytes for Li/S batteries [211]. In the next step, studies on different types of anions in Li/PS solutions [212] as well as in confining electrode materials are envisioned.

5 Chasing Aqueous Biphasic Systems from simple salts by exploring the LiTFSI / LiCl / H_2O phase diagram

5.1 Introduction

The interactions of ions with the solvent determine whether the ions are dispersed, aggregated, chemically/physically bound to each other or whether they precipitate out of the liquid electrolyte [29]. The attractive or repulsive forces between the ions caused by electrostatic, the van der Waals forces or steric hindrance will favor a certain liquid structure.

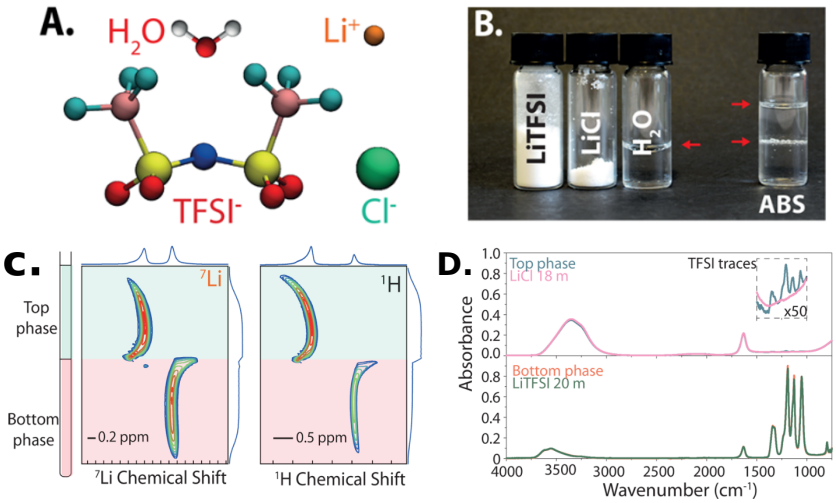

Figure 5.1: A. Constituents of the system: water molecule, Li^+ cation, $TFSI^-$ and Cl^- anions. B. Stoichiometric amount of LiTFSI, LiCl and water to prepare the 12m LiCl – 5m LiTFSI ABS. C. Chemical Shift Imaging (CSI) of an NMR tube containing the 12m LiCl – 5m LiTFSI ABS, revealing distinct local environments for Li^+ cations and water in the two phases. The color indicates the intensity (from blue for low to red for high) as a function of chemical shift and position, while the shape of the peaks reflects the distortion of the magnetic field near the liquid-liquid and liquid-air interfaces. D. FTIR spectra of the top and bottom phases of the 12m LiCl – 5m LiTFSI ABS compared with those of a 18m LiCl solution and a 20m LiTFSI solution, respectively.

Ionic correlations can induce an effective strong attraction between the ions and can trigger a phase separation, which might be accelerated in intermediate or highly con-

centrated solutions [30]. Aqueous biphasic systems (ABSs), in which two aqueous phases with different compositions coexist as separate liquids, were first reported more than a century ago with polymer solutions. Recent observations of ABS forming from concentrated mixtures of inorganic salts and ionic liquids raise the fundamental question of how "different" the components of such mixtures should be for a liquid-liquid phase separation to occur. While first ABS based on polymers were discovered in the late 19th century [213], the coexistence of two aqueous solutions of different salts has only been reported much more recently and the range of such ABS remains comparatively limited [31, 32, 33]. Their composition usually involves a concentrated inorganic salt and an ionic liquid.

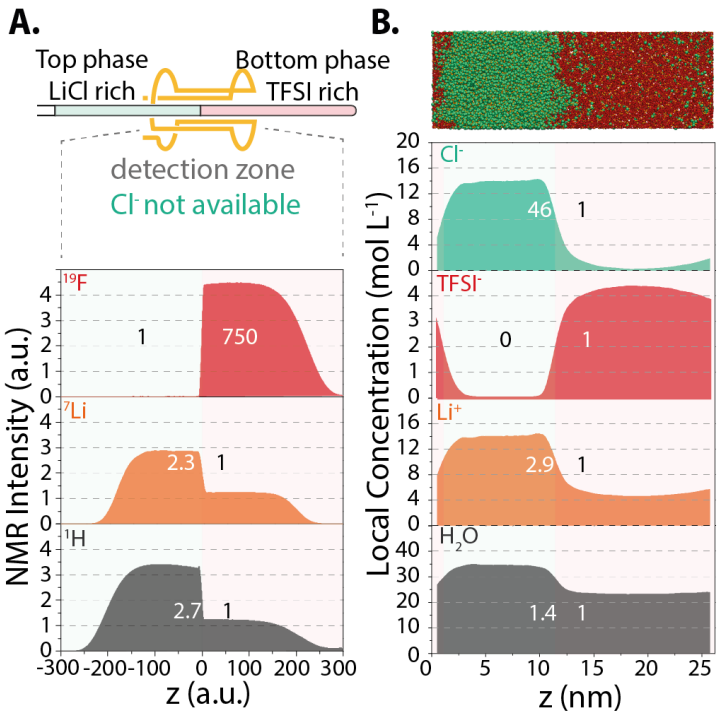

Figure 5.2: A. Density profiles for ^{19}F, ^{7}Li and ^{1}H obtained by NMR for the 12m LiCl – 5m LiCl ABS compared with B. those obtained by molecular dynamics simulations for Cl^-, $TFSI^-$, Li^+ and H_2O for the same system. On the top of panel B, a snapshot extracted from the simulation (Li^+ ions are in orange, Cl^- anions in green, $TFSI^-$ anions in red, and water molecules are not shown) illustrates the presence of a sharp interface.

Meanwhile, the development of aqueous lithium-ion batteries has recently led to the exploration of highly concentrated aqueous electrolyte solutions using organic lithium salts [214, 215, 216]. It prompts us the development of the relevant applications for

lithium-ion batteries with the phase separation property. Here we show that even mixtures of two monovalent salts sharing a common simple cation (lithium, Li^+) but with different anions result in the presence of water in the coexistence between two aqueous liquid phases over a wide range of compositions at room temperature. Specifically, we investigate aqueous mixtures of LiTFSI, which can form so-called "water-in-salt" [214, 215, 216] electrolytes (with a salt-to-solvent ratio larger than one in mass and volume) relevant *e.g.* for battery applications, and the more standard lithium chloride, LiCl, salt (see Fig 5.1A and simulated systems are summarized Table A.7 in Appendix).

5.2 Results

We show in Fig 5.1B that a global composition of 12m (mol/kg of water) LiCl and 5m LiTFSI results in approximately equal volumes of two coexisting liquids with a sharp interface. The formation of an interface between these two liquids exchanging matter is further evidenced in Fig A.12 in Appendix by images showing the evolution of a drop of 5m LiTFSI in a saturated (18m) LiCl solution, as well as by the measurement of a finite surface tension (5.7 mN/m for the 12m LiCl – 5m LiTFSI, approximately an order of magnitude smaller than the for the water-air interface).

Nuclear Magnetic Resonance (NMR) then provides spatially resolved specific information on the chemical environment of the various species. The evolution of the chemical shifts across the interface (Fig 5.1C) indicates that both Li^+ cations and water molecules adopt distinct local environments in the two liquid phases, while the change of dielectric constant results in a distortion at the interface between the two phases. In addition, Fourier-Transform Infrared (FTIR) spectroscopy allows us to probe the local environment of water in both phases, which in turn provides indirect information on their composition. As shown in Fig 5.1D, water molecules from the top phase exhibit O-H bond stretching modes (broad signal around 3400 cm^{-1}) similar to those in an aqueous 18m LiCl solution, while weak absorbance peaks around 1250 cm^{-1} reveal traces of TFSI in solution [217]. A similar resemblance between the bottom phase and aqueous 20m LiTFSI can also be deduced from their FTIR spectra.

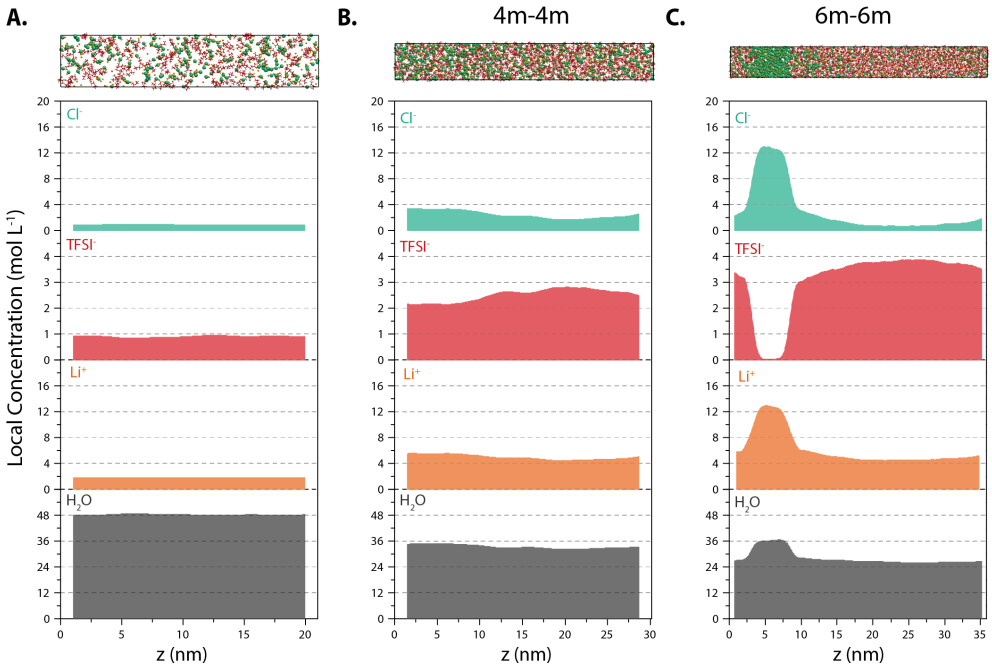

Figure 5.3: Concentration profiles obtained by Molecular Dynamics simulations for the 1m-1m (A), 4m-4m (B), and 6m-6m (C) systems. Snapshots of the simulations are also shown, with Cl^- anions in green, $TFSI^-$ anions in red, and Li^+ cations in orange (water not shown).

The liquid-liquid phase separation is further quantitatively examined in Fig 5.2, which compares the equilibrium density profiles for various elements probed by NMR imaging experiments and computed by MD simulations (see Appendix A.3.1). Despite the difference in length scales probed by both approaches (∼1 cm for NMR, ∼10 nm for MD), they provide a consistent picture of a sharp interface between two coexisting liquids. The compositions are in good agreement for the species that we could probe experimentally (all but Cl^- anions), which validates the MD simulations. In particular, MD simulations predict almost quantitatively the ratio of Li^+ concentration in both phases, as well as the virtual absence of $TFSI^-$ in the Cl-rich phase. The predicted water content in the TFSI-rich phase is smaller than in the other one, even though the ratio is slightly larger than the experimental one. The density profile for Cl^- is also readily available from MD (see Fig 5.3) and indicates that its concentration in the TFSI-rich phase is larger than that of $TFSI^-$ in the Cl-rich phase.

The formation of an ABS, *i.e.*, phase separation between two liquid phases, depends on the global composition of the system. The boundary between the monophasic and

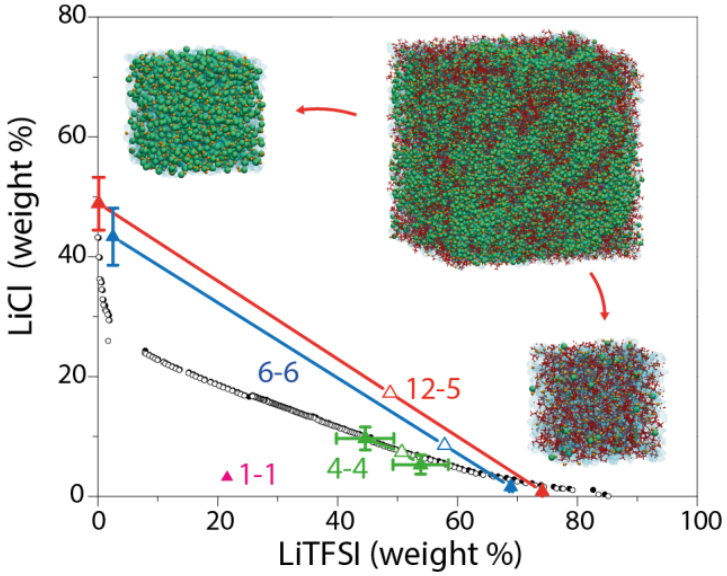

Figure 5.4: Phase diagram of the ternary LiCl-LiTFSI-H_2O mixture. The phase boundary is located by cloud point experiments between full black circles correspond to a biphasic system and empty circles corresponding to a monophasic system. Tie lines are obtained by MD simulations for 12m-5m (red), 6m-6m (blue), 4m-4m (green) and 1m-1m (magenta) LiCl-LiTFSI systems and relate the global composition of the system (empty triangles) to that of the resulting phases (full triangles). MD simulation snapshots illustrate the initial system for the 12m LiCl – 5m LiTFSI composition and resulting LiCl and LiTFSI rich phases (note that the latter are only zooms on each phase, since the complete system contains both of them separated by interfaces, as shown in Fig 5.2B).

biphasic regions of the phase diagram, determined by cloud point measurements (see Methods A.3.3 in Appendix), is shown in Fig 5.4. As for the above-mentioned system (12m LiCl + 5m LiTFSI), we also observe a phase separation in the MD simulations for a global composition of 6m+6m, while for a more dilute system (1m+1m) the system remains monophasic. At a global composition of 4m+4m, the system is close to the transition between the one- and two-phase behavior (see density profiles for 4m+4m and 6m+6m in Fig 5.3). The resulting compositions of the coexisting liquids in the phase-separating cases, obtained from the MD density profiles, are very close to the experimental phase boundaries. Such an agreement is remarkable considering the complexity of the system. This further supports the validity of the MD simulations, which in turn complements the experimental phase boundaries with the tie lines (which could in principle be obtained by separating and weighting both phases, but would require larger volumes and therefore be much more expensive).

We finally turn to the physical origin of the phase separation. In contrast to previously

reported ABS, in the present systems the salts share a common cation. In agreement with previous MD studies of bulk WiSEs [214], we find that in our case the relevant cationic species in both phases is the hydrated Li^+, despite the observed partial desolvation in this high concentration regime (see Fig 5.5), indicating that the phase separation is essentially driven by the different properties of the anions.

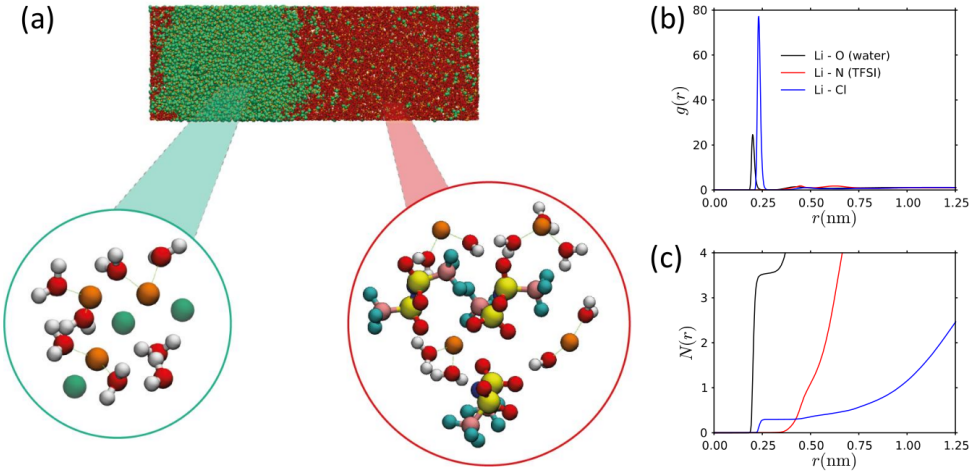

Figure 5.5: (a) MD snapshot of the 12m LiCl–5m LiTFSI system, showing the solvation structures of Li^+ cations (orange) in the LiCl (Cl^- in green in top panel and bottom left panel) and LiTFSI ($TFSI^-$ in red in top panel, with separate colors for each atom in bottom right panel) rich phases. Li^+ cations remain partially solvated by water molecules (O in red, H in white) in both phases. (b) Radial distributions around Li^+ cations in the TFSI-rich phase. (c) Running coordination numbers around Li^+ cations in the TFSI-rich phase

The driving force to form an ABS was previously proposed to result from the difference in interaction with water molecules between two salts: one structuring water (kosmotropic) and the other disordering the hydrogen bond network of water (chaotropic) [32], a phenomenon classically evidenced by viscosity measurements [218]. While $TFSI^-$ was reported to be chaotropic, viscosity measurements carried out in this work (see Fig A.13 in Appendix) reveal that $TFSI^-$ exhibits a positive Jones-Dole B-coefficient, which is usually observed for kosmotropic salts. This could result from the large size and hydrophobic character of $TFSI^-$ anion [219, 220]. However the concept of chao/kosmotropicity, which underlines the effect of individual ions on water, should be taken with some caution at such high concentrations. This is particularly true for WiSEs where the salt-to-water ratio is larger than one, since in this regime the effects of ion-water interactions are not additive [221, 222].

From a thermodynamic point of view, a mixture of a solvent with two salts sharing a common ion can be considered as a ternary mixture, due to the constraint of electroneutrality. Using integral equations, Lo Celso *et al.* analyzed the phase behaviour of such mixtures for neutral (solvent) and charged (ions) hard spheres [223] and found that an asymmetry in the size of the counterions can be sufficient to induce a phase separation, for a range of compositions and temperatures. On the microscopic scale, this means that the liquid structures satisfying both the local electroneutrality and packing constraints with each counterion separately are more stable than for the case when all ions are mixed. This is not to say that water does not play a role in the mixing free energy, which determines whether or not the phase separation occurs: It does contribute both energetically (via ion solvation and screening of electrostatic interactions) and entropically (configurational entropy via the composition of each phase). However, this contribution may not be the dominant one. This claim is further supported by the low solubility of alkali halides in conventional ionic liquids [224].

5.3 Summary and concluding remarks

In this chapter, we have shown the formation of ABS formed by mixing salts containing a common cation, namely LiTFSI and LiCl. With the help of NMR and MD simulations, we demonstrated that for a large range of compositions, the system segregates into two phases, one being rich in LiTFSI and containing some LiCl and one containing almost exclusively LiCl at high concentration. While the chao/kosmotropic phenomenological effect of ions was previously suggested, our findings support the idea that the anion size asymmetry is the driving force for the formation of an ABS in this system. While the first ABS based flow cell battery was proposed recently [225], preliminary results indicate the possibility to make use of this ABS to develop aqueous dual-ion batteries (see Fig A.14 in Appendix). Furthermore, controlling this phase separation phenomenon could provide new avenues to recycle LiTFSI from aqueous solutions.

6 Long-range correlation length in concentrated electrolytes

6.1 Introduction

The decay of correlations between particle positions and how electric fields are screened are of fundamental importance in liquid state physics as well as electrochemical devices. It influences the physio-chemical properties of liquid electrolytes, for instance the adsorption mechanism [226, 227, 228, 138, 229] or Faradaic reaction rates at the electrodes [11, 230]. An essential interaction between ions immersed in a continuum solvent is already well described by the DH theory, which predicts that the potential created by a solvated ion decays monotonically: for instance, exponentially with the distance from a flat surface (*e.g.*, a charged mica surface or a metallic electrode). The corresponding decay length (the screening length) is given by the Debye screening length λ_D (Eq. 1.1). This assumption is valid in dilute solutions; on the other hand, the DH framework is not applicable when the finite-size effects of ions and their concentration increases or the permittivity is low.

As the concentration increases, the structure of the electrolyte may undergo more dramatic changes than a simple correction to the mean-field DH picture. In his seminal review, Kirkwood reported the transition (now known as the Kirkwood line) from charge-based monotonic to oscillatory exponential decay [231]. This is, however, not the only transition observed in electrolytes: the Fisher-Widom line defines a change from an asymptotic monotonic decay to an oscillatory one governed by the packing of the discrete species in the system [232]. In the 1990s, parallel yet independent endeavors based on liquid-state theories for the primitive model of electrolytes (charged hard spheres), by Evans [233, 139, 234] using the Mean Spherical Approximation (MSA) and by Attard [235] using the hypernetted chain closure, developed a more complex portrait of the effects of concentration and temperature on correlations in electrolytes.

Both strategies identified areas of charge and density-dominated oscillatory decays as well as charge-dominated monotonic decay. The decay of ionic correlations has also been analyzed within the dressed ion theory, an exact reformulation of the statistical mechanical description of electrolytes developed by Kjellander and Mitchell [236, 237, 238, 239], used in particular to investigate the primitive model of electrolytes. These studies, together with molecular simulations of molten salts [240, 241] or charged hard spheres [242], and more recent attempts with coarse-grained models, in particular to relate the structural properties in such systems to their electrochemical response in capacitors [243, 244, 227, 245, 246, 229, 222], situated the field in a position of strong theoretical understanding.

Approximately 70 years since Kirkwood's review, there has been a distinct lack of an experimental observation of such transitions between decay regimes. However, recent surface force experiments by Gebbie *et al.* [247, 35] uncovered a long-range force between charged plates across an ionic liquid. While the interpretation of such a long-range force was debated [248], its existence was subsequently shown to be a more general property of concentrated electrolytes and harmonized with the previous work of Evans and Attard by Lee *et al.* [249, 36]. It is different from the more readily explicable short-range structures observed in confinement [250, 251] and follows a "universal" behavior, observed for a variety of liquid systems with different solvents and ions: upon increasing concentration, the decay length of the measured surface forces, λ_{exp}, transitions from a DH-like regime of decreasing length until it becomes comparable to the ion diameter d, to an "anomalous" regime of increasing (and sometimes large) decay length at higher concentration, according to a simple scaling law [252]

$$\left(\frac{\lambda_{\mathrm{exp}}}{\lambda_{\mathrm{D}}}\right) \sim \left(\frac{d}{\lambda_{\mathrm{D}}}\right)^{\alpha} \tag{6.1}$$

with an exponent $\alpha \approx 3$. A long decay length has also been observed in ionic liquids by atomic force microscopy, [253] and recent fluorescence-based measurement of ion density also offered the first observation of a long-range correlation length in a concentrated electrolyte using a nonforce-based method [254].

The experimentally observed increase in screening lengths has prompted a new set

of theoretical works to explain the specific behavior observed in experiments. Using fluctuation theory and MSA theory, a study of the restricted primitive model (RPM, charged hard spheres with identical diameters) recovered the transition between the regimes and a scaling compatible with Eq. 6.1 albeit with a smaller exponent and corresponding smaller correlation lengths [255]. Another mechanism was proposed by Lee *et al.* to explain the observed scaling, based on the creation of charge defects [252], reminiscent of that reported by Uralcan *et al.* in the context of the capacitive response of dense ionic solutions [226]. A recent classical density functional theory study reproduced some features of the changes in the oscillatory structure observed by Evans and Attard, as well as the associated increase in screening length [138]. Very similar results were obtained using a simple model based on the modification of the Coulomb interaction, though again without reproducing the experimentally observed value of α [256]. Finally, within this current environment, Kjellander further expanded his dressed ion theory in an attempt to describe the experimental observations [24, 257].

At present, it cannot be ruled out that these approximate theories do not capture all correlations in the behavior of real world electrolytes. In contrast to model electrolytes, in reality "chemical" complexities arise due to the atomistic and molecular nature of complex ions and solvents and their many degrees of freedom. With improved computational power nowadays, MD simulations can be performed with relatively high accuracy and are accessing the same time scales of the correlation lengths and the necessary sampling times of the correlations. Therefore, in this chapter, we study the correlations length of the charge-charge pair correlations in concentrated electrolyte solutions by means of MD simulations.

6.1.1 Simulated systems and force fields

We study four liquid electrolytes (three in aqueous solvent and one in organic solvents) to mirror the extremely diverse experimental systems in which these behaviors were observed in Refs. [249, 252]: aqueous solutions of LiCl, NaI and LiTFSI, as well as the same LiTFSI salt solvated in an mixture of DME and DOL.

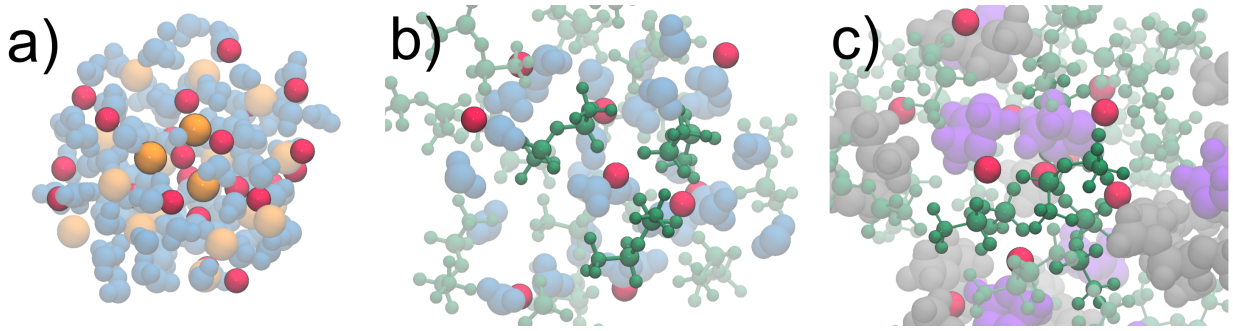

Figure 6.1: Illustration of the simulated systems: a) LiCl in water, with Li^+ in red, Cl^- in orange and water molecules in blue; we also investigate similar NaI solutions (not shown). b) LiTSFI in water, with $TFSI^-$ anions in green. c) LiTFSI in an organic solvent, namely an equimolar mixture of DME, in gray, and DOL, in violet. See Table 6.1 for the composition of all simulated systems.

The structures of all the constituent molecules and ions are shown in Fig 6.1. The simple salts are modeled using the Dang force field [258, 259], the water is modeled using the SPC/E force field [260], while for TFSI we use the Siqueira [261] force field for the aqueous systems and CL&P [170] force field for organic ones, in line with previous studies. We use the ECC model for LiTFSI in DME/DOL systems. The same force fields for DME and DOL are employed as in previous chapters. The lengths of the simulations and dimensions of the boxes are provided in Table 6.1. We can note from this information that in order to perform these simulations successfully we have to use exceptionally large boxes and long simulation times.

6.2 Results

Fig 6.2 shows some calculated RDFs illustrative of the general trends obtained across all salts at all concentrations. Looking first at the RDFs for aqueous lithium chloride in panel 6.2a, at 0.5 mol/L (dashed lines) for both for $g_{\mathrm{LiLi}}(r)$ and $g_{\mathrm{ClCl}}(r)$ there is a long-range decay towards $g_{ij} = 1$ with some features overlayed owing to the solvation structure. At a higher concentration of 5 mol/L (solid lines), however, these correlation functions immediately exceed 1 in their first peak and then oscillate about $g_{ij} = 1$

Table 6.1: Salt concentrations, box sizes and simulation run times for the four simulated systems.

Concentration (mol/L)	box size (nm)	Simulation length (ns)	Molar ratio $\frac{n_{\text{ion pairs}}}{n_{\text{solvent}}}$
LiCl(aq)			
0.2	8.93	50	0.004
0.5	8.91	50	0.009
1	8.88	50	0.019
2	8.84	50	0.040
5	8.76	50	0.115
10	8.68	50	0.295
NaI(aq)			
0.2	8.94	50	0.004
0.5	8.94	50	0.009
1	8.93	50	0.019
2	8.94	50	0.041
5	9.00	50	0.124
10	9.14	50	0.354
LiTFSI(aq)			
0.3	11.97	34	0.006
1	8.00	80	0.021
2.35	8.47	80	0.063
3.54	9.32	50	0.126
4.48	8.62	40	0.216
4.85	10.57	30	0.271
5.34	10.24	30	0.361
LiTFSI(DME/DOL)			
0.20	10.54	200	0.023
0.51	10.74	200	0.048
0.98	10.96	185	0.098
1.98	11.03	200	0.229
3.1	10.43	200	0.444
4.87	11.09	200	1.18

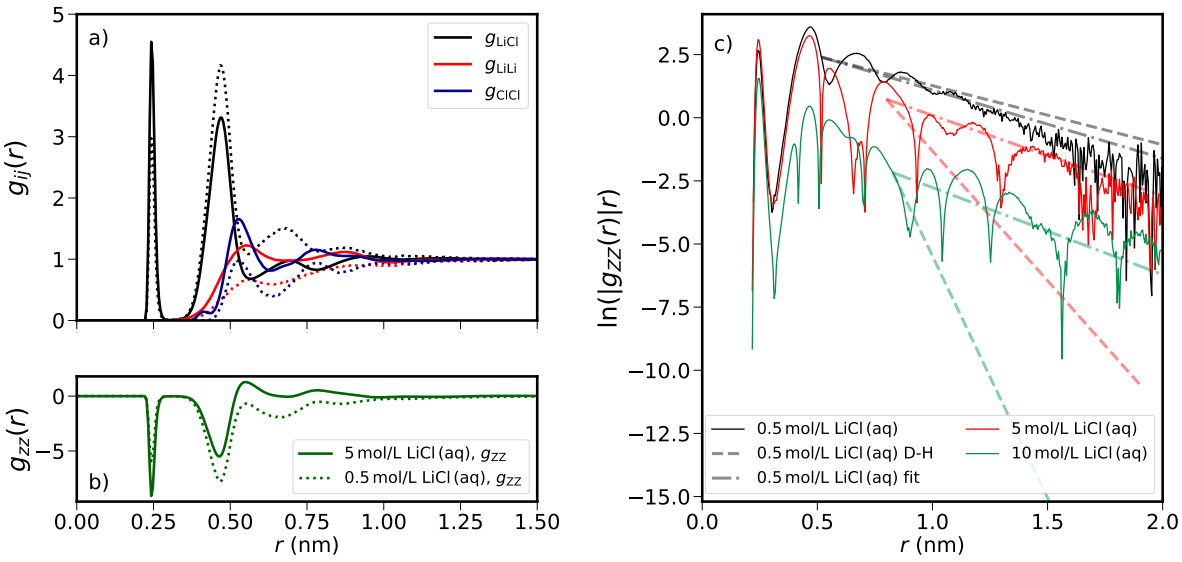

Figure 6.2: Correlation functions of aqueous LiCl. a) RDFs ions for 0.5 mol/L (dotted) and 5 mol/L (solid) for LiCl(aq). b) Charge–charge correlation functions, $g_{ZZ}(r)$, for concentrations of 0.5 mol/L (dotted) and 5 mol/L (solid) for LiCl(aq). c) $\log(|g_{ZZ}(r)|r)$ for three concentrations of LiCl(aq): 0.5 M, 5 M, and 10 M. The dotted curves in this panel correspond to the prediction simple DH theory, Eq 1.1, while the dashed-dotted lines illustrate the gradients obtained from fitting the MD data to straight lines outside the initial solvation peaks (*cf* Table A.8 in Appendix).

in an increasingly damped manner. The most striking features of $g_{\mathrm{LiCl}}(r)$ at both concentrations are the forepeak at 0.25 nm, which is representative of contact ion pairs, and a second peak at 0.5 nm representative of ions separated by a single water molecule. Beyond these two peaks, the long-range behaviors in $g_{\mathrm{LiCl}}(r)$ are analogous to $g_{\mathrm{LiLi}}(r)$ and $g_{\mathrm{ClCl}}(r)$, with decay towards $g_{ij} = 1$ from above for 0.5 mol/L and increasingly damped oscillations about $g_{ij} = 1$ for 5 mol/L.

The charge-charge correlation functions $g_{ZZ}(r)$ in Fig 6.2 b for 0.5 mol/L (dashed lines) and 5 mol/L LiCl (aq) (solid line) show similar behaviors as observed for the individual RDFs. At 0.5 mol/L, $g_{ZZ}(r)$ tends towards zero in a manner consistent with DH theory. At 5 mol/L (solid line), an initial peak related to solvation is followed by damped oscillations about $g_{ZZ}(r) = 0$. These behaviors correspond to what was previously observed in the RDFs. Figure 6.2 c shows $\log(|g_{ZZ}(r)|r)$ used to calculate the decay length (see Eq (2.42)) for three concentrations of aqueous LiCl (0.5, 5 and 10 mol/L).

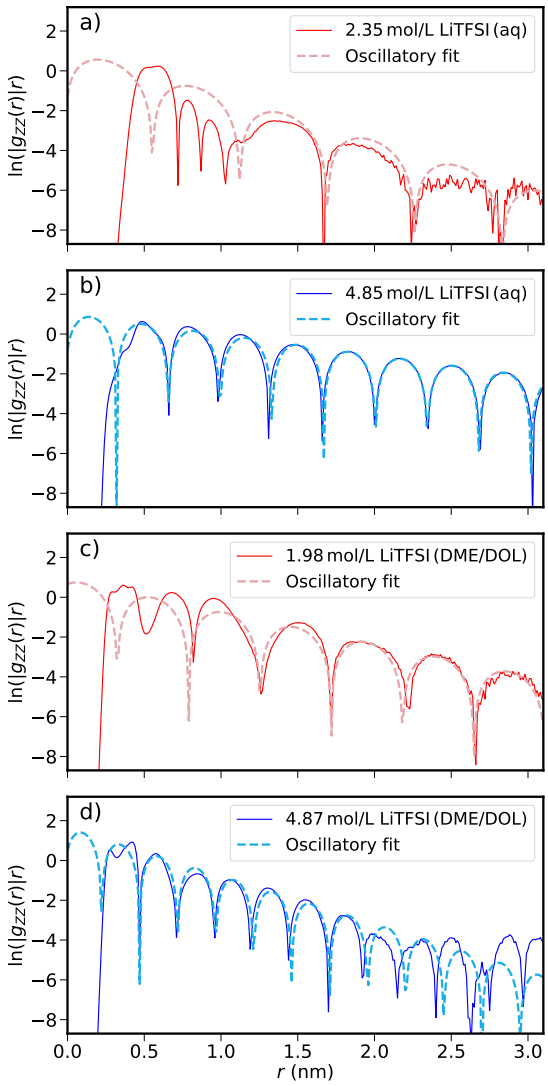

Figure 6.3: Correlation functions of aqueous and organin solutions of LiTFSI. $\log(|g_{ZZ}(r)|r)$ for 2.33 mol/L (a), and 4.85 mol/L LiTFSI (aq) (b) and for 1.98 mol/L (c), and 4.87 mol/L LiTFSI (DME:DOL) (d). The paler dashed curves are oscillatory fits (see Eq 2.42) of the MD data. For both salts, a substantial decrease in oscillatory wavelength is observed upon increasing concentration (from red to blue curves)

We first note the differences in the form of the plot beyond 1 nm: for the 0.5 mol/L LiCl(aq) system, there is a linear decay, while higher concentrations the decay maintains an oscillatory nature beyond the initial solvent layering. The crossover between these regimes has previously been theoretically predicted in a general scene [138, 262, 235], and observed experimentally for solutions of an ionic liquids in propylene carbonate [263]. Then, the comparison with the prediction of DH theory (dashed lines in panel 6.2 c) indicate large deviations at higher concentrations (as expected), with an anomalously long correlation length.

Beyond the simple salts considered so far, Fig 6.3 shows the charge-charge correlation function for the LiTFSI salt in the regime of oscillatory decay, and examines more specifically the effects of salt concentration (increasing from panel a) to b) and from c) to d)) and of the nature of the solvent (water in panels a) and b), DME/DOL in panels c) and d)). In all panels, we also plot the fits of the simulation results to Eq (2.42).

In both the aqueous and organic cases, increasing concentration results in a better-defined oscillatory structure. This is obvious in the more concentrated aqueous case (panel b), where the oscillatory decay is remarkably represented by Eq (2.42) up to very large distances. Such a particularly well-defined structure appears to be a feature of this salt, compared *e.g.* to the LiCl case of Fig 6.2c) (see Figs A.15, A.17 and A.18 in Appendix for the other salts) In addition, in both solvents the wavelength of the oscillations decreases with increasing concentration, as discussed in more detail below.

The changing nature of these structures has previously been described by de Carvalho and Evans using the generalized MSA [234]. This study contextualized previous theoretical work by proposing that with increasing concentration, one observes crossovers of correlations in charge and number densities from monotonic to oscillatory decays, at the Kirkwood [231] and Fisher–Widom [232] lines, respectively. They proposed that the correlation electrolytes could have one of three natures: monotonic charge dominated decay, oscillatory charge dominated decay, and oscillatory density dominated decay. In a real system the wavelength of a charge dominated oscillatory decay will be roughly twice that of a density dominated decay, due to packing constraints. These three natures can be linked by means of a phase diagram dependent on both temperature and reduced ion density. Here at moderate temperatures the system can be assumed to undergo a structural crossover from charged monotonic decay to charged oscillatory and eventually to density dominated oscillatory decay for 1:1 electrolytes, with 2:2 electrolytes showing a very different structure with charge dominated decay being observed at the highest concentrations [234].

In their more recent study consisting of both MD simulations and analytical theory of a hard sphere ion-solvent mixture, Coupette *et al.* [138] found a structural crossover between density to charge dominated oscillatory decay with increasing concentration

for binary monovalent salts, which is somewhat different to Evans and de Carvalho's previous study [234]. This illustrates the high sensitivity of the dominant mechanism to different variables including ion charge, concentration, ion asymmetry, and ion size. Here we observe no significant change in the oscillatory period for simple salts. However for LiTFSI in both solvents there is a sharp decrease in oscillatory period by roughly a factor of 2 at around 2 mol/L, suggesting a transition from charge dominated oscillatory structure to a density dominated one. This can be observed in Fig 6.3 panels a and b where the oscillatory period for 2.33 mol/L LiTFSI(aq) can be seen to be twice that of 4.85 mol/L as well as in panels c and d for 2 and 4 mol/L LiTFSI (DME:DOL).

Fig 6.4 collates the screening lengths obtained for each salt (values are listed in Table A.9 in Appendix) which also shows all the charge-charge correlation functions from which they are extracted). Taking inspiration from previous theoretical studies [234, 235] and plotting $\log(\lambda_{\text{sim}}/\lambda_{\text{D}})$ against $\log(d/\lambda_{\text{D}})$, with d being the mean ion diameter, discussed below, the experimental data collapse onto a single curve. As can be seen from the expression Eq 1.1 of the Debye length, the ratio d/λ_{D} is essentially equivalent to the square root of the concentration, only with a slight modulation for the permittivity, which depends on the system (nature of the salt and its concentration, nature of the solvent). We evaluate the permittivity in the simulations in two ways: (i) more approximately but as typically done by considering only the fluctuations of dipoles in molecules and molecular ions, and (ii) accurately by additionally taking into account the translational contribution of the ions via Einstein-Helfand method [264, 142, 265, 266] (see section 2.3.2 in Appendix). The corresponding permittivities and noted ϵ_r^{rot} and ϵ_r, respectively (see Table A.9 in Appendix). In panels 6.4a and 6.4b, the mean diameter d_{vol} is defined as in previous experimental studies [249], as half the diameter of a sphere with a volume equal to that per a single ion pair [249]. This can be obtained by a linear extrapolation of ion and solvent densities as shown in Fig A.19. In panel 6.4c, we consider instead the position of the first peak in the RDF for an unlike ion pair, d_{RDF}. The effect of the definition of the permittivity, calculated with or

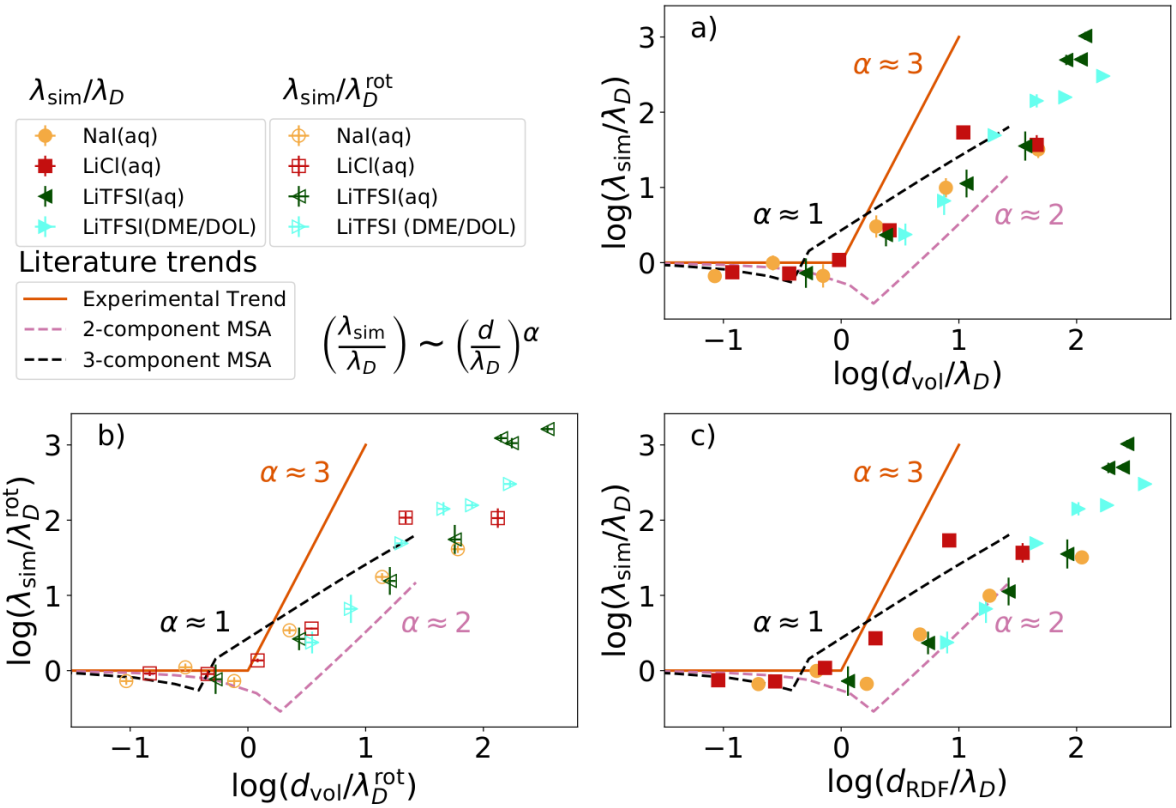

Figure 6.4: Ratio between the simulated correlation length and the Debye length, as a function of the ion diameter divided by the Debye length, on a double-logarithmic scale, *i.e.*, $\ln(\lambda_{sim}/\lambda_D)$ vs. $\ln(d/\lambda_D)$. The three panels correspond to different choices of relative permittivity ϵ_r to compute the Debye length and of the ion diameter d: (a) d_{vol} is calculated as half the diameter of a sphere with a volume equal to that of an ion pair; (b) the same value of d is used as in (a) but the Debye length (λ_D^{rot}) is calculated using the permittivity arising only from the rotational contributions, ϵ_r^{rot} (see Table A.9 in Appendix); (c) the value of d_{RDF} is calculated from the first peak in the RDFs, which should occur at the same distance as the mean ion diameter for simple salts. As an illustration of predictions from liquid state theory, we show results with the mean spherical approximation (MSA) from Ref. [255] (see text for details and discussion of other theories). The experimental trend is the one reported in Ref. [249].

without the translational contribution of ions, on the Debye length and corresponding scaling plot, is examined in panel b where the debye length obtained using only the contribution of molecular dipoles (λ_D^{rot}) is employed.

All three panels of Fig 6.4 display a similar form to those reported from the surface force balance experiments, consisting of three regions. First, DH like behavior at the lowest values of d/λ_D. Next, a transition region where the screening length λ_{sim} is slightly shorter than λ_D. Finally, at high concentration ($d/\lambda_D >> 1$) the screening lengths increases approximately as predicted by Eq 6.1 but with the exponent α between 1 and 2. This third region corresponds to the anomalous behavior observed in recent

experimental studies [263, 249, 35], and its elucidation is the motivation behind this study. The quality of its description in the three panels varies depending on the choices made in calculating the mean ion diameter. However, the method by which the Debye length was calculated does not affect the form of the curve. The data appears to be better unified by using the volume derived value d_{vol} in panels a and b, than the one derived from RDFs , d_{RDF}, in panel c. This is probably due to the complex non-spherical nature of the TFSI anion, a problem that may be particularly pertinent due to the bidentate and monodentate coordination of the TFSI oxygen atoms to lithium cations.

6.3 Discussion

While the present study provides clear indications from MD simulations of extended screening lengths in concentrated electrolytes, the results should now be compared to the experimental ones and put in the broader perspective of the theoretical studies trying to account for the latter. A positive feature of all the results summarized in Fig 6.4 is that they exhibit a general scaling form, near identical to the one obtained in experiments [249]. However, an important difference between these molecular simulation results and the experimental values is the scaling exponent α in Eq 6.1, visible in Fig 6.4 as the slope of the line in the high concentration region. As can be seen in Fig 6.4 the experimental slope taken from Ref. [249] (solid orange line, $\alpha = 3$), is far steeper than that obtained from simulated data ($\alpha \approx 1.3$). This corresponds well with several previous theoretical studies, all of which have been unable to recover a gradient as large as that measured experimentally [262, 138], as discussed below. Importantly, such a lower exponent reflects the fact that the decay lengths are much smaller than those reported in experiments. As shown Fig A.20 in Appendix, the values of λ_{sim} do not extend beyond 1 nm, *i.e.*, of the order of 1-2 molecular diameters, in contrast to the experimentally reported values of up to 4 nm for simple salts, and 10 nm for ionic liquids [249].

The lower exponent (and corresponding smaller screening length) is, however, in good

agreement with previous theoretical results, with reported exponents ranging between 1 and 2 [262, 138, 256, 257]. As an illustration of such predictions of liquid state theories, Fig 6.4 also indicates the results of Ref. [262], obtained using the MSA for the RPM, *i.e.* with cations and anions modeled as oppositely charged hard spheres with identical diameters. These results are reported as dashed lines in Fig 6.4): In the 2–component MSA, the solvent is not modeled explicitly but solely as a continuum with a homogeneous permittivity, whereas the 3–component MSA maintains this continuum effect but also includes the solvent molecules as uncharged spheres of the same size as the ions. Both approximations result in the 3–region structure described above, and the corresponding slopes of 1 and 3/2 bound the trends observed in the present work with molecular simulations. Such similar results suggests that the underlying behavior we have observed is fundamental to charged particles in solution.

Another prediction of liquid state theories for the RPM is the existence of a cusp, visible on the lines in Fig 6.4. However, the relatively small variations in this $d/\lambda_D \sim 1$ range, together with the limited number of simulated systems prevents the definite observation of such a cusp, as in the experiments – for which it is also difficult to extract decay lengths comparable to the molecular sizes, since the 'long-range' regime is then mixed with the short-range solvation forces. Such a cusp was also obtained by Adar *et al.* by introducing a simple modification of the Coulomb interaction kernel to account for the excluded volume of the neighboring ions [256], which resulted in the high-concentration regime in a scaling exponent $\alpha = 2$, *i.e.* between the present results from MD molecular simulations and the experimental ones.

We note that in the high-concentration regime, all the theoretical decay lengths correspond to an oscillatory decay, while no such oscillations are observed in the experimental force profiles. However, it should be remembered here that surface force experiments do not directly measure the bulk correlation length, but forces between confined interfaces. The long-range behavior of these forces is governed by the decay modes of the bulk fluid [139], provided there are no additional features (*e.g.*, chemistry) arising at the interface. While it is possible that long range correlations exist, which are too weak to be observed in molecular simulations (see below), the similarity be-

tween the simulations and theoretical model suggest that the difference may arise from elsewhere. On the experimental side, two possible sources of this discrepancy with the experimental results are the confined setups used in both the surface force [249] and fluorescence [254]experiments, and the lateral ordering of ions at interfaces, as has been previously observed with great detail for ionic liquids on graphite [267], and for simple salts on muscovite mica [268] using state of the art imaging atomic force microscopy experiments. Conversely, it might be possible to make progress using liquid state theory, by introducing additional complexity (*i.e.* beyond Coulomb interaction and finite volume of the ions) within models treating, *e.g.*, ion pairing and clustering, or charge regulation on surfaces, within analytically or numerically tractable assumptions [269, 270, 271].

We finally note that, even though we did not observe indications of an effect of the finite size of the simulation boxes (as shown in Fig. A.21 in Appendix), additional correlation lengths extending beyond the box sizes considered in the present work might still exist in real systems. From the practical point of view, this would lead to two difficulties to capture them in molecular simulations. On the one hand, the computational cost associated with such systems sizes (beyond tens of nm) and corresponding time scales needed to sample their configurations would become prohibitive. On the other hand, identifying the slowest decay length might become even more challenging because the corresponding features would be difficult to sample accurately (this is already visible in the noisier data for larger distances). In principle, progress on the former aspect could be expected thanks to the increase in computational resources, to the use of more efficient algorithms and resort to simpler yet accurate (coarse-grained) models of electrolytes. As for the latter, one may consider both using improved estimators of the radial distribution functions [272, 273] and more sophisticated analysis of the latter to extract the correlation lengths, based *e.g.* on Bayesian inference [274].

6.4 Summary and concluding remarks

The results we have presented corroborate the general experimental trend of increasing decay length in high concentration electrolytes. The recovered increase is governed by a universal power law of the same form as experimentally observed, however, the exponent is significantly lower than experimentally observed, albeit very similar to previous theoretical calculations of correlations in bulk electrolytes. Accordingly, the decay lengths in the high concentration regime obtained with the present molecular simulations (and earlier theories for primitive models of electrolytes) are in the range of 1-2 molecular diameters, much shorter than those reported experimentally (up to $\sim$ 10 nm). Though the reason for this difference is difficult to assess, one may identify two concurrent origins for such differences. On the one hand, while the consistent results obtained for various liquids seem to indicate that quantitative differences are not due to details of the electrolyte models (in particular force fields), it remains difficult to sample numerically the long tails of the RDFs. On the other hand, all experimental studies reporting such long correlation lengths involve liquids confined between surfaces (this is the case for force-based and fluorescence-based studies). It may therefore be instructive to investigate theoretically whether such a confinement may induce long-range correlations that are not present in the bulk (at least one study of confined electrolytes, using the primitive model and MSA theory, did not observe such behavior [275]), and large-scale molecular simulations may also contribute to such a modeling endeavor [226].

7 Summary and outlook of the thesis

7.1 Summary

In chapter 3, we construct an efficient molecular model for state-of-the-art battery electrolytes used in metal-sulfur or metal-air batteries. Our atomistic model is verified with a variety of experimentally observable structural and dynamical features. Experimental measurements, for instance the density, dielectric constant, viscosity, and diffusion coefficient of solvent mixtures DME/DOL are consistent with our MD simulations for all molar ratios. The ionic systems with 1:20 ratio also reproduce experimental conductivities and Li^+ transference number. It indicates that the ECC model in MD simulations is crucial to demonstrate the proper Li^+ solvation structure and pair association with $TFSI^-$ anions in DME/DOL solvent. Moreover, the physical properties, such as Li^+ solvation environment and diffusivity of the full state-of-the-art Li/S battery electrolytes are in detail investigated and give unprecedented structural insight in the composition of the important first lithium solvation shell.

In chapter 4, we incorporate polysulfide species into the electrolytes solutions and develop an atomistic model for PS. We focus particularly on structural and dynamic properties of three different sizes of PS ions, ${S_4}^{2-}$, ${S_6}^{2-}$, ${S_8}^{2-}$ in the presence of Li^+ and $TFSI^-$ ions. The conductivity and diffusion coefficients of PS solutions from our atomistic model are consistent with experimental measurements. Conductivities of PS solutions from both experiments and MD simulations exhibit an increase with the Li_2S_x concentrations and eventually a saturation at around 0.5 M. The saturation in the conductivity can be linked to viscosity and the ionic correlations between PS and Li^+, which also lead to occurrence of supramolecular clusters. The tendency of clustering increases with the concentration of Li_2S_x and is more pronounced for shorter PS ions (i.e., $x = 4$). It can be attributed to their electronic density more strongly localized at the terminal sulfur atoms than longer chains, thus facilitating the electrostatic attraction with Li^+. The addition of $TFSI^-$ ions into the solutions, brings

about larger amount of dissociated Li^+ ions and to a noticeable increase in the viscosity. The relationships between the dissociated Li^+ and conductivity are discussed with the modified NE equation. We demonstrate that the dissociated Li^+ contributes to the conductivity significantly. At larger PS concentrations, increased viscosity inhibits the conductivity. According to the transference number results and the strong binding between Li^+ and ${S_4}^{2-}$, Li_2S_4 behaves as a neutral species. We conclude that these short PS chains are more likely to participate in the shuttle mechanism during the charge. It is found that $TFSI^-$ reduces cluster formation of shorter PS ions. Even though TFSI ions do not significantly reduce the Li^+–PS binding, they weaken the binding between multiple PS ions into clusters. As a consequence, the addition of LiTFSI into the solutions increases the solubility of PS ions and with that enhances the shuttle effect in the Li/S batteries. Our simulation results of PS solutions reveal that structural and transport properties are subject to subtle interactions among ions and solvents molecules, which should be considered carefully when it comes to the design of electrolytes for Li/S batteries as well as other energy-storage devices.

A phase separation might exist in concentrated electrolytes if the physio-chemical properties of liquid are very different. In chapter 5, the formation of ABS constituted by mixing salts containing a common cation. We explore the phase diagram for a large range of compositions with NMR and MD simulations and find the segregation into two phases, one being rich in LiTFSI and containing some LiCl and one containing almost exclusively LiCl at high concentration. While the chao/kosmotropic phenomenological effect of ions is previously suggested, our findings support the idea that the anion size asymmetry is the driving force for the formation of an ABS in this system. Our results present the possibility to make use of this ABS to develop aqueous dual-ion batteries. Namely, controlling this phase separation phenomenon could provide new avenues to recycle LiTFSI from aqueous solutions.

In chapter 6, we conduct MD simulations of a selected set of concentrated monovalent electrolytes in homogeneous bulk solution, in an attempt to directly quantify the long-range correlations. Our MD simulations results show a similar trend with the general experimental observations of increasing decay length in high concentration electrolytes.

The recovered increase is governed by a universal power law of the same form as experimentally observed, however, the exponent is significantly lower than experimentally observed, albeit very similar to previous theoretical calculations of correlations in bulk electrolytes. The possible inconsistency between experiments and our MD simulation (as well as the primitive models and MSA theory) might be the surface effects in experiments. All experimental studies reporting such long correlation lengths involve liquids confined between surfaces. Thus, the confinement effects might be investigated whether it causes the long-range correlations.

7.2 Outlook

In chapters 3 and 4, as shown, our atomistic model for Li/S battery electrolytes reproduces the experimental transport properties and gives insight drawn from the atomistic structures in bulk. With our atomistic model, the research can be applied to the transport and structural properties at interfaces. Cleavage of S_8 ring and PS dissolution are observed immediately as soon as the discharge is initiated [276]. Even though, sulfur molecules are supposed to stay in the cathode, PS and Li_2S_2/Li_2S react with the anode and form insoluble layers [277, 84]. PS dissolution is not easily avoidable unless one employs a microporous (≤ 0.5 nm) carbon structure [278], sulfurized organics (*i.e.* PAN) [76] or solid-state electrolytes [279] to bypass the interaction between sulfur and electrolyte. Once PS is dissolved into the electrolyte, PS might either (1) undergoes redox reaction near the conductive host and precipitates or (2) be detached and diffuse from the host, resulting in being electrically insulated. The battery capacity will be deteriorated if the scenario (2) is dominant. For the reason, a large number of studies attempt to increase the affinity between carbon materials and PS by using anchoring agents such as a heterogeneous atom doping on carbon [280], conductive polymers [281] and metal oxides [282, 283]. Meanwhile, studies of atomistic-level structural properties at interfaces are still lacking. With our model, the adsorption properties of PS on the graphene surfaces or confinement can be investigated. The adsorption properties are subject to choices of solvents, ions, concentrations, etc. Hence, one can screen various

solvents or lithium salts. Subsequently, promising candidates (solvents or lithium salts) could be narrowed down for experiments. The polarizability of interfaces can affect the ionic adsorption. Thus, the Drude oscillator model or a constant potential electrode model can be considered. Moreover, various conductive host materials also have many merits for Li/S batteries. Sulfurized-polymer matrix, metal oxides or Mxene nanosheets can be studied to verify the interface properties of Li/S battery solutions.

Several studies have suggested using the sparingly solvating electrolytes to decrease the solubility of PS [284, 285, 209]. It is expected that the low solubility of PS might retard the PS shuttle. On the other hand, other studies have proposed to use a salt anion with a high donor number [286, 287]. Two different strategies also raise questions of the behavior of PS in confinement, where the solubility or clustering properties of PS might behave differently from that in the bulk. Our atomistic model can be applied to the Li/S battery solutions with various anions with different donor numbers to elucidate the solvation structure, adsorption and clustering behavior in confinement.

In order to translate a laboratory scale to an application cell level, high sulfur loading or low electrolyte-to-sulfur (E/S) ratio is necessary to facilitate high energy density. Yet, the low content of electrolyte in a system causes high viscosity and a limiting diffusion of the electrolyte. It can also cause dewetting of the electrode, leading to capacity loss. MD simulations can investigate the dynamical and solvation properties of the electrolyte with low E/S ratio.

Chapter 5 shows that the phase separation is driven by the different ionic sizes and thermodynamics, leading to retard the mass transport between the phases. The partition of PS electrolyte might be applied to conventional Li/S or flow batteries where the immiscibility of PS electrolyte is exploited to control the solubility of PS and its migration. Various strategies can be attempted to stimulate the phase separation, which hinders the PS shuttling between the electrodes. For example, the large range of possible components, *e.g.* ionic liquids, salt or solvents, can be examined. In addition, the effects of the temperature or pH may play a role in the phase behavior [225].

In chapter 6, we find significant inconsistency between experiments and our MD simulation. Even though the finite-size effects on the decay lengths were not observed in our

MD simulations, large-scale molecular simulations or advanced sampling methods may also contribute to such a modeling endeavor [226]. All experimental studies reporting such long correlation lengths involve liquids confined between surfaces (this is the case for force-based and fluorescence-based studies). It may therefore be instructive to theoretically investigate whether such a confinement may induce long-range correlations that are not present in the bulk (at least one study of confined electrolytes, using the primitive model and MSA theory, did not observe such behavior [275]). In addition, the long-range correlations that appear in the concentrated electrolytes might change the local electric fields near interfaces [11]. As a result, the transport of ions through and out of the electric double layer would be affected. These details of atomistic level MD simulations and models may underpin a continuum level battery theory.

In sum, we successfully discussed the structure-property relation in Li/S battery electrolytes and demonstrated the phase separation and long-range correlations in intermediate or highly concentrated electrolytes. Further, extensive research can be conducted to improve Li/S batteries and elucidate the intrinsic properties of concentrated electrolytes.

A Appendix

A.1 Electrolyte structure and dynamics in battery solvents

A.1.1 Force fields

Table A.1: Dielectric constant ϵ (evaluated via Eqs. 2.43 and 2.44) and viscosity obtained from MD simulations for DOL/DME with different force fields. OPLS-AA-1 includes the original parameters from the all-atom OPLS force field. OPLS-AA-2 employs the same interaction parameters as OPLS-AA-1, but the partial charges q of DOL are from the modified TraPPE-UA force field. OPLS-AA-3 uses the partial charges calculated from quantum chemistry calculations (Gaussian [187]). The chosen force fields for the result production in this work is assigned with an ‡ mark.

force fields	dielectric constant ϵ	viscosity (mPa s)
DOL		
experiments	7.00 (298 K) [288]	0.58 [174]
AMBER	6.6	0.79(2)
TraPPE-UA	2.4	0.44(1)
OPLS-AA-1‡	5.9	0.56
OPLS-AA-2	13.5	0.56(1)
OPLS-AA-3	7.8	0.49(1)
DME		
experiments	7.05 (298 K) [288]	0.42 [173]
OPLS-AA-1‡	10.6	0.43(1)
AMBER	10.9	0.58(2)

Table A.2: Force field test of Li^+ in terms of σ and ϵ. The test set of test-1,3-4 and 6 are taken from literature, see references in the Table. The LJ parameters of test-2 is produced in a such way that the σ_{ii} and ϵ_{ii} are taken from test-1 and test-3, respectively. The value of σ_{ii} in test-5 is modified based on test-4. The last column shows diffusion coefficients of the lithium ion in LiTFSI/DME (the molar ratio of 1:20) at 304 K.

simulations	σ_{ii} (nm)	ϵ_{ii} (kJ/mol)	source	D_{Li^+} ($10^{-10}m^2$ s^{-1}) Expt. : 7.7 [160]
test-1	0.12	26.15	Chandrasekhar et al. [289]	7.5(1.0)
test-2	0.12	0.076		8.6(1.0)
test-3	0.21	0.076	OPLS-AA [115]	7.6(1.0)
test-4‡	0.1507	0.6906	Dang et al. [172]	7.6(1.1)
test-5	0.172	0.69		7.8(1.0)
test-6	0.288	0.00061	Horinek et al. [290]	7.7(1.0)

Table A.3: Diffusion coefficients of the ions and molecules in LiTFSI/DOL (the molar ratio of 1:20) at 304 K with different LJ parameter sets as well as two different partial charge q of DOL are shown.

Li^+ parameters	D_{Li^+}	D_{TFSI^-} ($10^{-10}m^2$ s^{-1})	D_{DOL}
experiments [160]	6.4	6.2	17.0
the partial charge q_{DOL} using OPLS-AA-1			
test-4‡	6.4(0.4)	5.7(0.7)	17.0(0.4)
test-6	5.7(1.0)	5.3(1.0)	13.4(1.0)
the partial charge q_{DOL} using OPLS-AA-3			
test-4	5.7(1.0)	5.7(1.0)	16.3(1.0)
test-6	5.8(1.0)	5.6(1.0)	16.4(1.0)

A.1.2 Finite-size effects

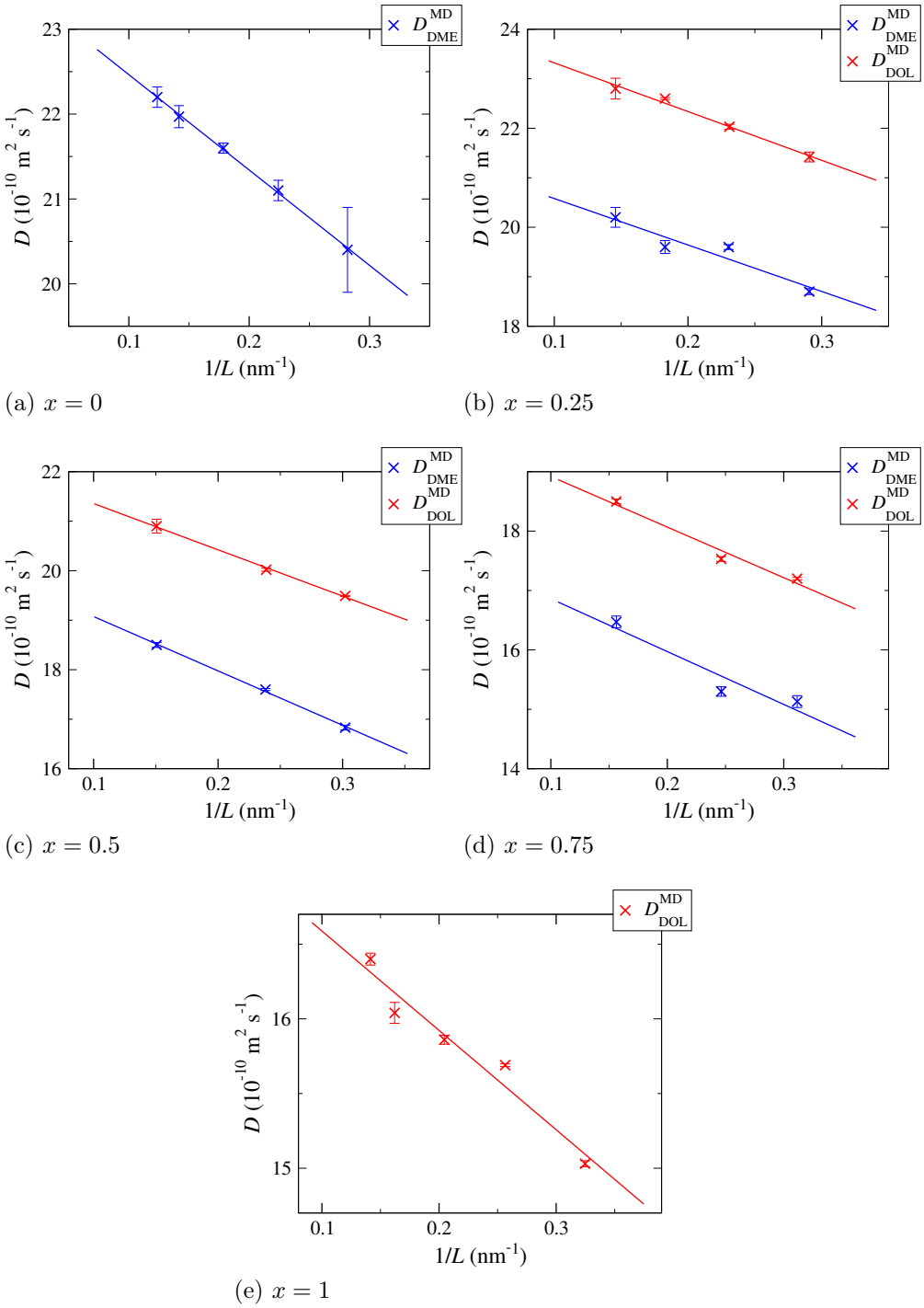

(a) $x = 0$ (b) $x = 0.25$

(c) $x = 0.5$ (d) $x = 0.75$

(e) $x = 1$

Figure A.1: Diffusion coefficients of the solvent molecules in system I versus the inverse simulation box size $1/L$ for various molar ratios x. Extrapolation to infinite box sizes, $1/L \to 0$, provides the 'real', finite-size corrected diffusion coefficients and L-dependent correction $\Delta D_{\mathrm{FSC}}(L)$.

A.1.3 Structure : Radial distribution function RDF

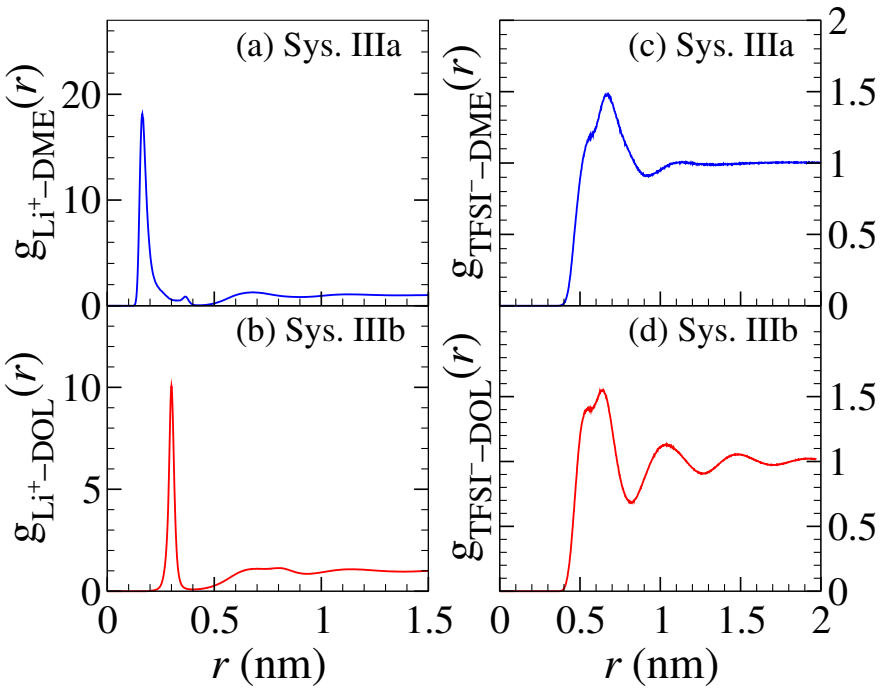

Figure A.2: Center of mass RDFs in system IIIa, panels (a) and (c), and system IIIb, panels (b) and (d), are shown. $g_{Li^+–DME}(r)$ and $g_{Li^+–DOL}(r)$ for the corresponding systems are shown in the left column and $g_{TFSI^-–DME}(r)$ and $g_{TFSI^-–DOL}(r)$ for the corresponding systems are shown in the right column.

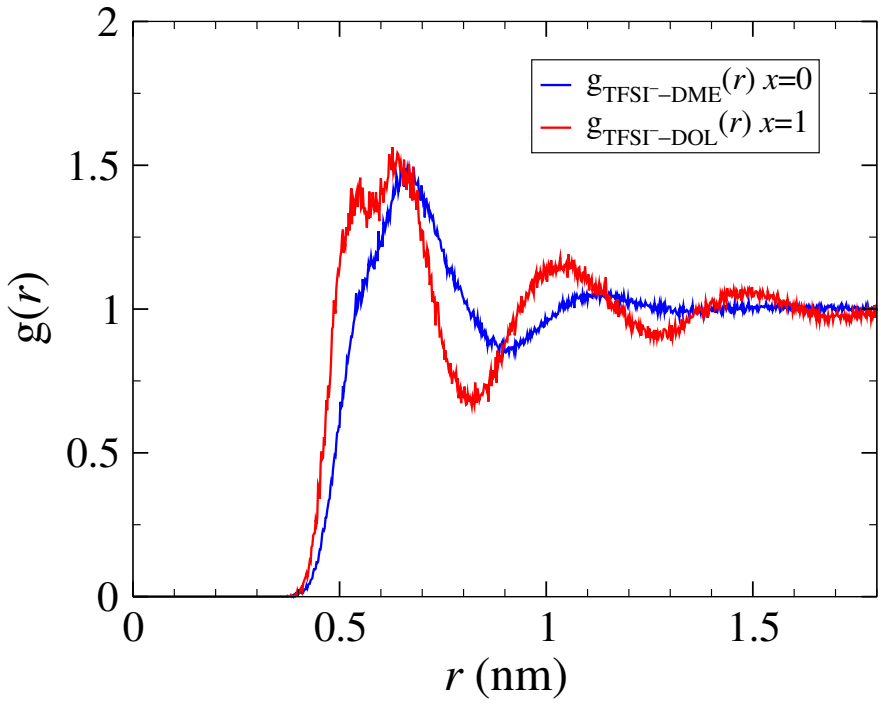

Figure A.3: Center of mass RDFs of $g_{\mathrm{TFSI^-\text{–}DME}}(r)$ at $x = 0$ and $g_{\mathrm{TFSI^-\text{–}DOL}}(r)$ at $x = 1$ in system IIc are depicted by the blue and the red lines, respectively.

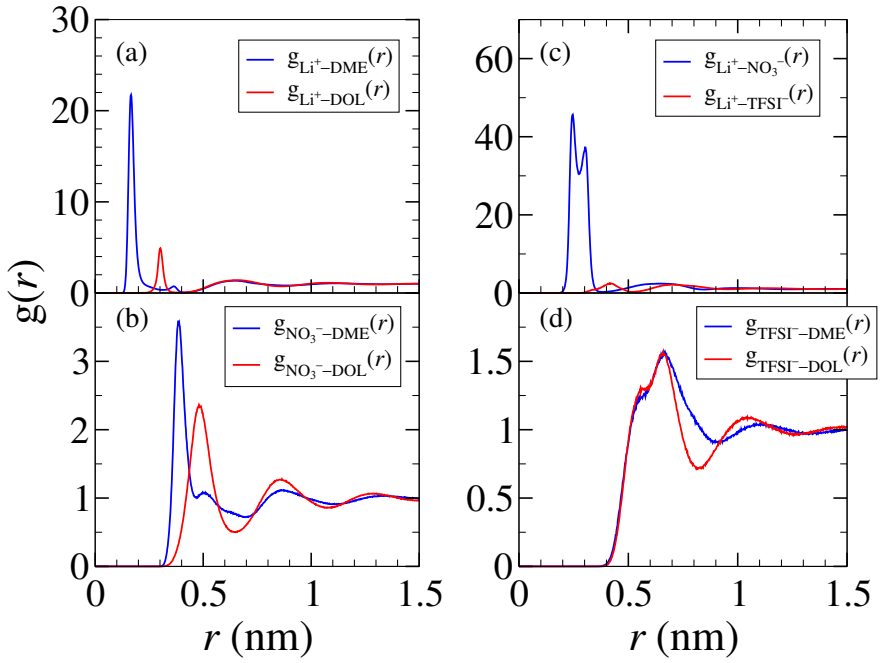

Figure A.4: Center of mass RDFs of system IVa. $g_{\mathrm{Li^+\text{–}DME}}(r)$, $g_{\mathrm{Li^+\text{–}DOL}}(r)$, $g_{\mathrm{Li^+\text{–}NO_3^-}}(r)$ and $g_{\mathrm{Li^+\text{–}TFSI^-}}(r)$ are shown in panel (a) and (c), $g_{\mathrm{NO_3^-\text{–}DME}}(r)$, $g_{\mathrm{NO_3^-\text{–}DOL}}(r)$, $g_{\mathrm{TFSI^-\text{–}DME}}(r)$ and $g_{\mathrm{TFSI^-\text{–}DOL}}(r)$ are exhibited in panel (b) and (d).

A.1.4 Conductivity

Table A.4: The conductivity measured by impedance spectroscopy corresponding to system IVa. The measurements are carried out in different salt concentrations in DME and DOL (1:1 wt%) solvents.

Salts molarity	conductivity (S m^{-1})
0.6M $LiNO_3$ + 0.3M LiTFSI	0.59(3)
0.4M $LiNO_3$ + 0.5M LiTFSI	0.88(3)
0.2M $LiNO_3$ + 0.7M LiTFSI	1.11(3)

A.2 Structural and transport properties of the Polysulfide Species

A.2.1 Force fields – Sulfur non-bonded parameters

Table A.5: Lennard-Jones parameters for sulfur from conventional force fields (FF). Conductivity calculations are carried out using OPLS-AA, CHARMM27, and DREIDING FF for a benchmark (see Fig. A.6).

	σ_S (nm)	ϵ_S (kJ mol^{-1})
OPLS-AA [115]	0.3550	1.0460
AMBER99 [188]	0.3563	1.0460
GAFF [291]	0.3563	1.0460
CHARMM27 [189]	0.3919	1.9664
ENCAD [190]	0.3844	0.3088
ECEPP [191]	0.3698	0.9330
UFF [192]	0.3596	1.1464
DREIDING [193]	0.3592	1.4393

A.2.2 Conductivity

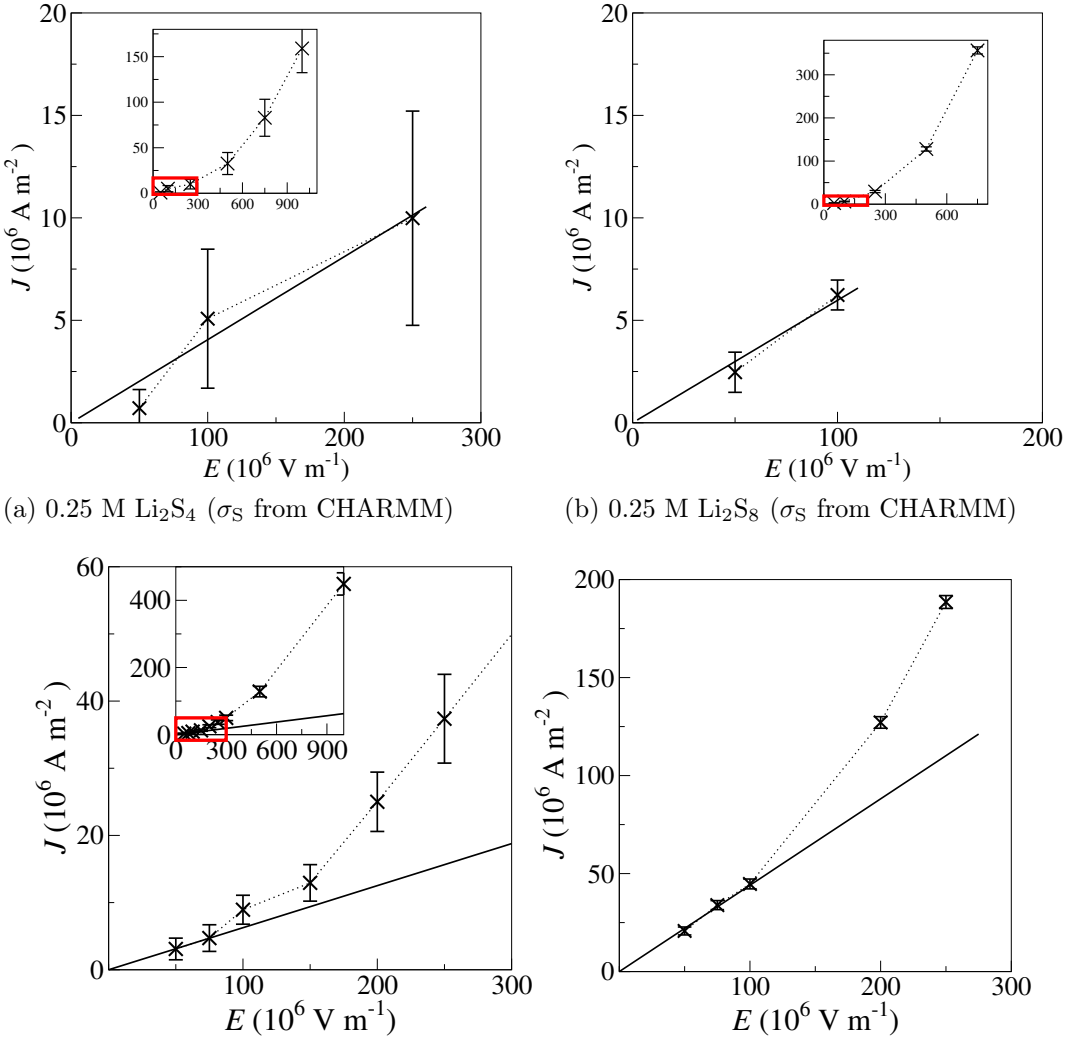

(a) 0.25 M Li_2S_4 (σ_S from CHARMM)

(b) 0.25 M Li_2S_8 (σ_S from CHARMM)

(c) 0.25 M Li_2S_4 (σ_S from DREIDING, $\sigma_{Li\text{-}S} = 0.275$ nm)

(d) 0.25 M Li_2S_8 (σ_S from DREIDING, $\sigma_{Li\text{-}S} = 0.275$ nm)

Figure A.5: Current density versus applied electric field using different FFs for S atoms. (a) and (b) are results from CHARMM FF for S. (c) and (d) are results from DREIDING FF for S and with $\sigma_{Li-S} = 0.275$ nm set manually. Conductivity is computed within the linear response regime. Insets show larger range of the evaluated data, where the red rectangles indicate the regions shown in the main plot.

A.2.3 Lennard-Jones parameterization based on conductivity

Figure A.6 shows conductivity in the dependence of polysulfide concentration for different force fields. The conductivities with σ_S from the OPLS-AA and CHARMM force fields are shown by orange and blue symbols, respectively, and deviate by more than an order of magnitude above concentrations of 0.5 M (both panels). The results from the DREIDING FF with different σ_{Li-S} values span over two orders of magnitude for the largest concentration of Li_2S_4. Hence, using an interpolation of the latter results, we choose the value of $\sigma_{Li-S} = 0.275\,nm$ for the cross-interaction (that is, by scaling the geometric mixing value by a factor of 1.0786) in order to fit the experimental conductivity measurements, while other LJ parameters for S are taken from the DREIDING FF.

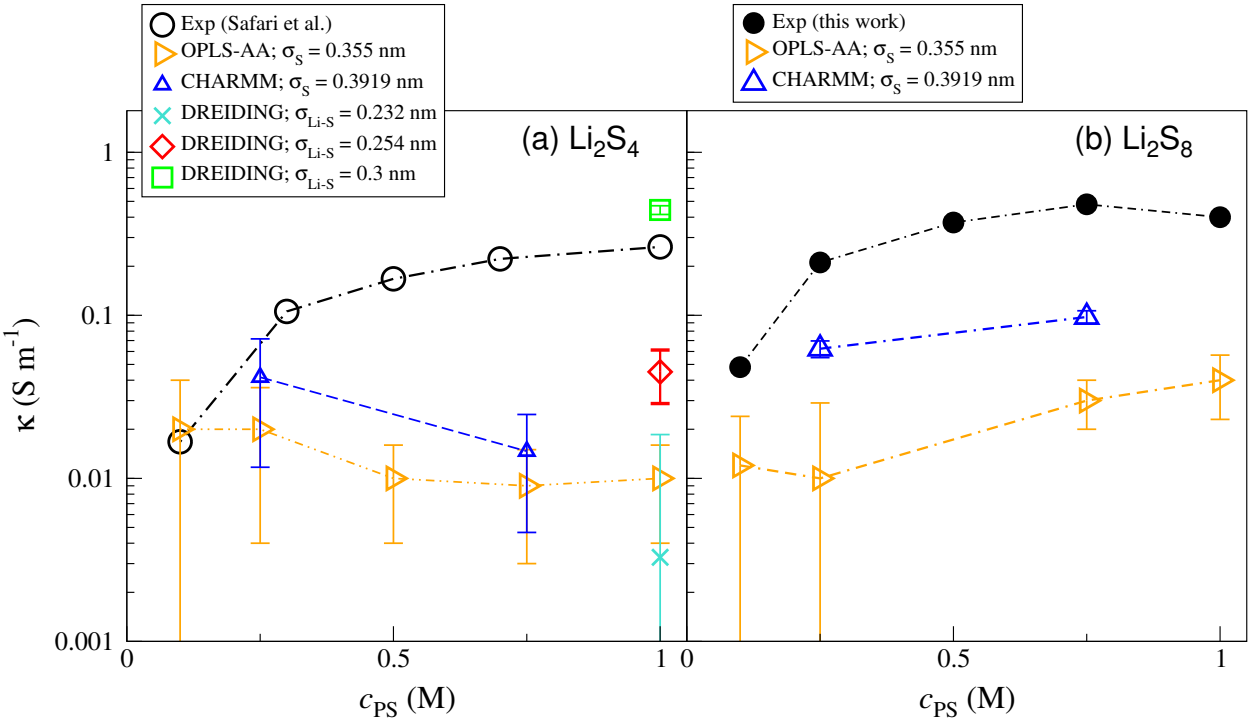

Figure A.6: Conductivities from simulations using different σ_S or σ_{Li-S} and from experimental measurements (Safari *et al.* [16] and ours) of (a) Li_2S_4 and (b) Li_2S_8 in DME/DOL (as a function of polysulfide concentration).

A.2.4 Radial distribution functions: 0.25 M Li_2S_x in DME/DOL with 1 M LiTFSI

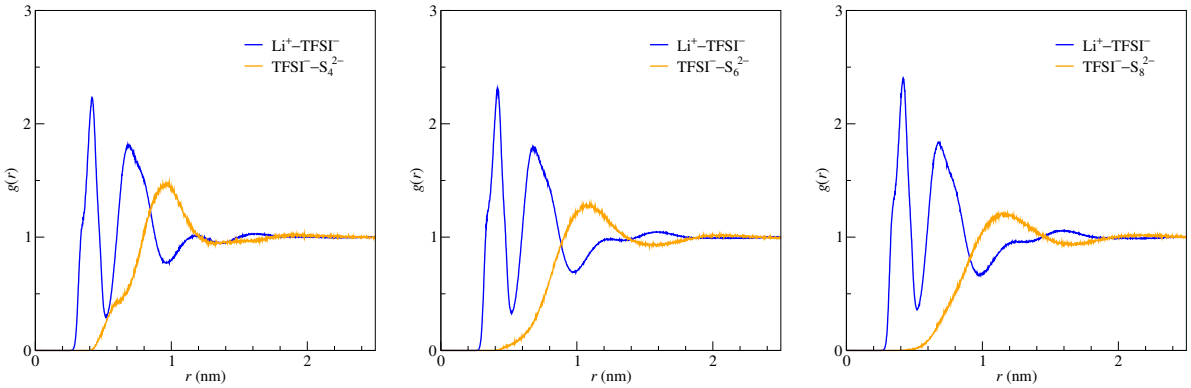

(a) 1 M LiTFSI + 0.25 M Li_2S_4 (b) 1 M LiTFSI + 0.25 M Li_2S_6 (c) 1 M LiTFSI + 0.25 M Li_2S_8

Figure A.7: Center-of-mass RDFs of Li^+–$TFSI^-$ and $S_x{}^{2-}$–$TFSI^-$ in 0.25 M Li_2S_x with 1 M LiTFSI in DME/DOL.

A.2.5 Correlation function

Table A.6: The integral $\int_0^\infty h_{ij}(r)rdr$ in units nm^2, which appears in Eq. 4.2, for different pairs of atoms.

	Li^+–Li^+	Li^+–S_x^{2-}	S_x^{2-}–S_x^{2-}
0.1 M Li_2S_4	3.0(1)	7.4(1)	1.5(1)
0.5 M Li_2S_4	0.66(3)	1.46(1)	0.40(2)
0.1 M Li_2S_6	2.2(4)	5.6(4)	1.5(4)
0.5 M Li_2S_6	0.29(1)	1.01(1)	0.05(1)
0.1 M Li_2S_8	2.4(4)	4.8(4)	1.8(4)
0.5 M Li_2S_8	0.03(1)	0.49(1)	0.03(1)

A.2.6 Diffusion coefficients without ECC

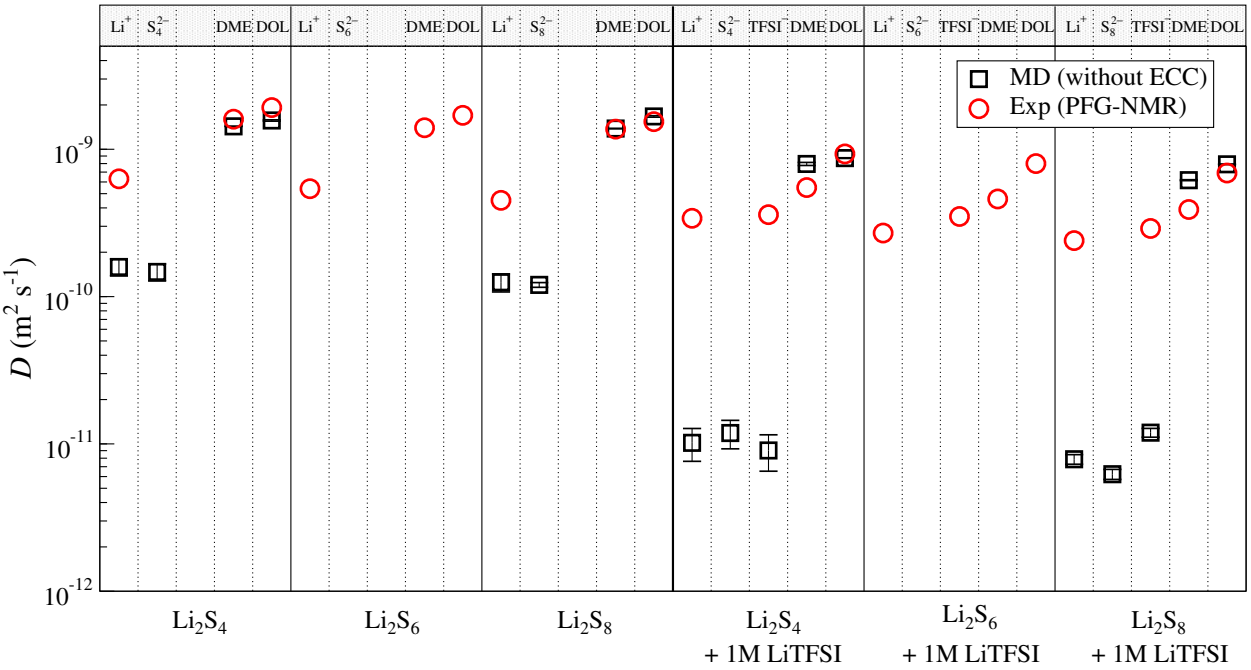

Figure A.8: Long-time self-diffusion coefficients D of all species in 0.25 M of the polysulfide without applying the ECC approach (black squares) and PFG-NMR experimental measurements [98] (red circles).

A.2.7 Viscosity

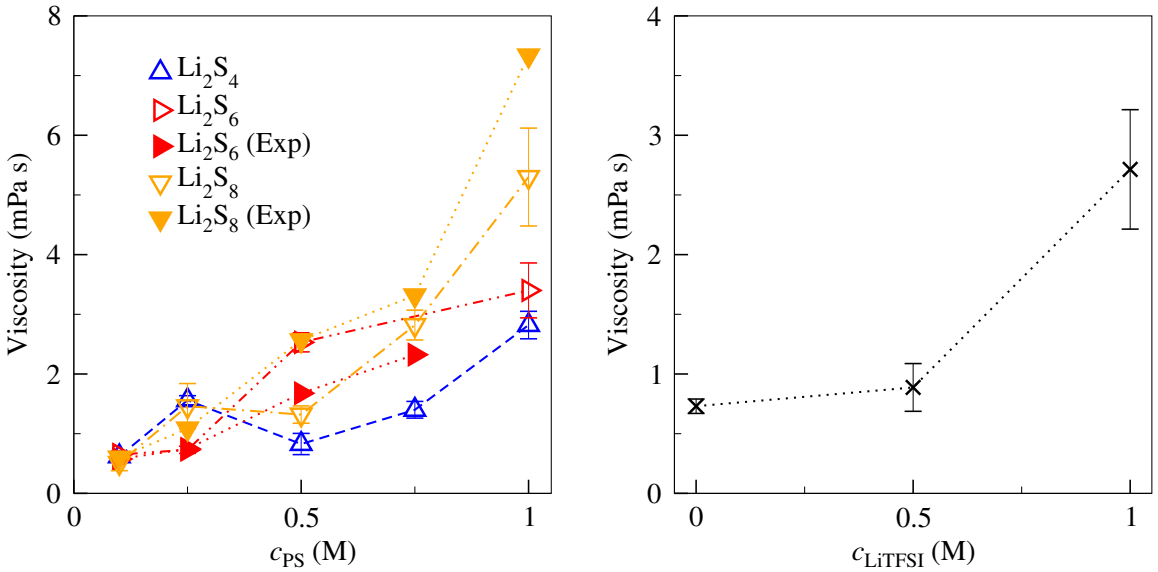

(a) Li_2S_x in DME/DOL.

(b) 0.25 M Li_2S_6 + LiTFSI in DME/DOL.

Figure A.9: (a) Viscosities of Li_2S_x in DME/DOL ($x = 4, 6$, and 8) as a function of polysulfide concentration. Filled triangles are our experimental measurements for Li_2S_6 and Li_2S_8. Empty triangles are viscosities from our MD simulations. (b) Viscosity of 0.25 M Li_2S_6 in DME/DOL as a function of LiTFSI concentration from our MD simulations.

A.2.8 Clustering

A.2.8.1 Li_2S_2 in DME/DOL

Cluster size distribution analysis is carried out for Li_2S_2 with/without 1 M LiTFSI in DME/DOL (Fig. A.10). Initially, the molecules are inserted into the simulation box at random positions and we monitor the mean cluster size $<N>$ as a convergence test, see Fig. A.10a. After 150 ns, the cluster size distribution is calculated in Fig. A.10b. A snapshot of 0.25 M Li_2S_2 in DME/DOL is shown in Fig. A.11.

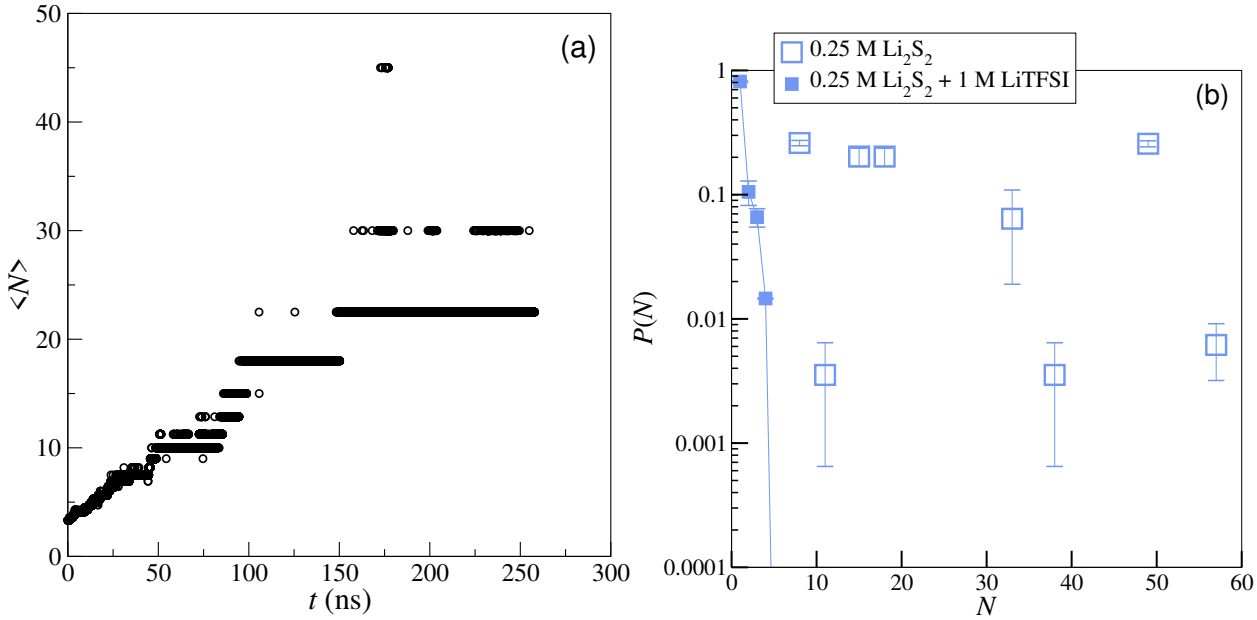

Figure A.10: (a) Convergence test monitoring the number of clusters in 0.25 M Li_2S_2 in DME/DOL. (b) Log-lin plot of polysulfides cluster size distribution for 0.25 M Li_2S_2 in DME/DOL or 1 M LiTFSI DME/DOL. The cluster size distribution is analyzed after 150 ns.

A.2.8.2 Snapshot: Li_2S_2 in DME/DOL

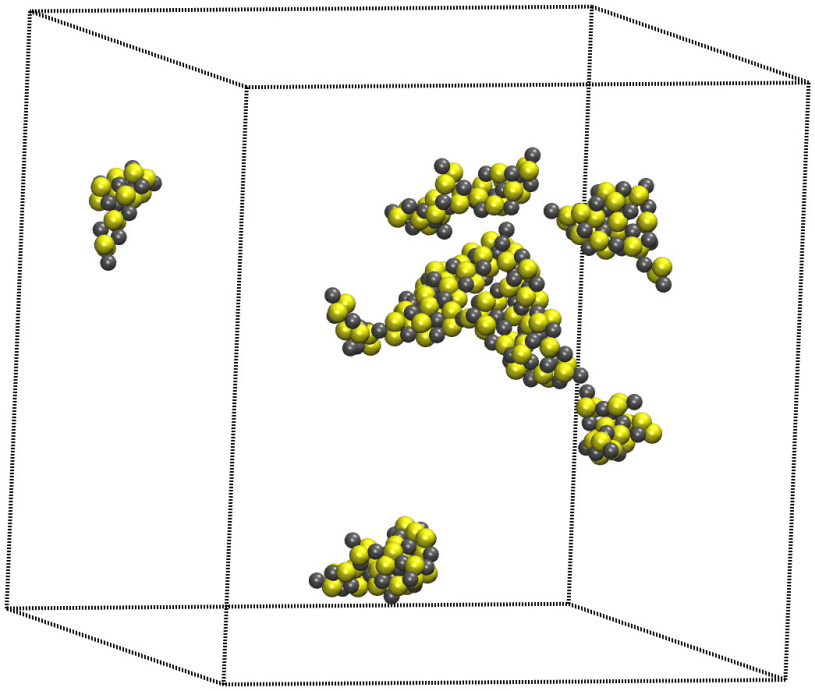

Figure A.11: Snapshot of 0.25 M Li_2S_2 in DME/DOL after 290 ns (the solvent is not shown). Gray: Li^+ and yellow: ${S_2}^{2-}$.

A.3 Chasing Aqueous Biphasic Systems from simple salts by exploring the LiTFSI / LiCl / H_2O phase diagram

A.3.1 MD simulations

All-atom molecular dynamics simulations are carried out with the GROMACS 5.1 simulation package [292]. Initially, two independent simulation boxes for LiCl+water and LiTFSI+water are prepared with the PACKMOL package [293] according to the concentrations of interest. The sizes of the simulation box and numbers of species are summarized in Table A.7. The initial configurations in the simulation boxes are first relaxed by minimizing the potential energy using steepest descent and then the two independent simulation boxes are merged into a single simulation box. For the equilibration and production runs, the simulation boxes are maintained at an isotropic pressure of 1 bar with the Parrinello-Rahman barostat [109] and the temperature at 298 K with a velocity rescaling thermostat [108]. We monitor the density profiles for ions and water molecules until the profiles are converged (see Table A.7) for the duration of the equilibration and production runs). The density profiles reported in the figures correspond only to the production runs. Periodic boundary conditions are applied in all three spatial directions. Non-bonded interatomic interactions are described by a 6–12 Lennard-Jones potential with a cut-off at 1.2 nm. The Particle-Mesh-Ewald (PME) method 5 with a Fourier spacing of 0.12 nm and a 1.2 nm real-space cut-off is used to calculate electrostatic interactions. The LINCS algorithm [294] is employed for all bond constraints. The OPLS-AA force field [115] is used for Li^+, Cl^- and the CL & P force field [170] is employed for $TFSI^-$. The SPC/E model is used for the water molecules [260].

Table A.7: Simulation box sizes, duration of the production run and numbers of ions/molecules in MD simulations

System	Equilibrium box	Equilibration	Number of ions/molecules			
	nm^3	Production runs (ns)	Li^+	Cl^-	$TFSI^-$	Water
1m+1m	4.2 × 4.2 × 21.0	100 & 400	400	200	200	10746
4m+4m	4.2 × 4.2 × 30.2	500 & 230	1600	800	800	10746
6m+6m	4.2 × 4.2 × 35.9	500 & 180	2340	1170	1170	10746
12m+5m	9.1 × 9.0 × 26.2	200 & 160	11137	7937	3200	35988

A.3.2 Photography of drop of LiTFSI in LiCl aqueous solutions

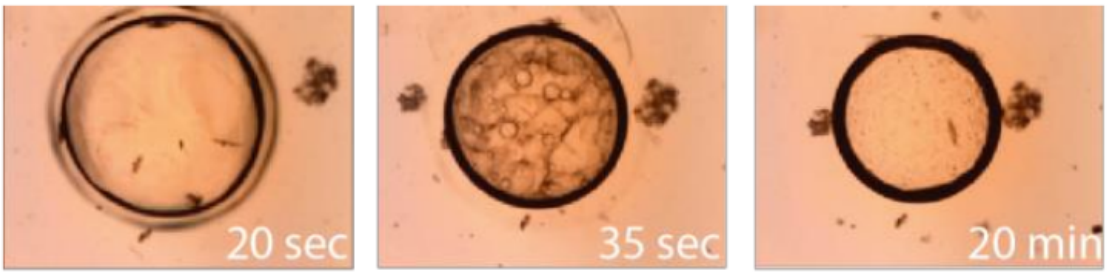

Figure A.12: Optical microscopy images showing the evolution over time of a $\sim$ 10µL drop of 5 m LiTFSI solution in 18 m LiCl solution.

In Fig. A.12, the decrease of the drop diameter reveals a mass transfer from the 5 m LiTFSI phase to the 18 m LiCl solution, which could be attributed to a transfer of water. After 20 minutes, no further evolution was observed. This confirms the formation of a stable ABS even for small volumes.

A.3.3 Phase-diagram construction

The phase diagram is constructed using the point-cloud titration method [31]. Briefly, a precise mass of a concentrated solution of LiTFSI (20 m) or LiCl (18 m) is introduced in a test tube, which was weighted (m_I). The other solution is introduced dropwise, until a cloudy solution is observed. The tube is weighted again (m_c) so that the mass of the added solution can be deduced ($m_S = m_c$ - m_I) and the composition of the system is reported as a point of coexistence (biphasic system). Then, water is added dropwise until the solution turns limpid. The tube is then weighted (m_L) to determine the mass of added water ($m_W = m_L$ -m_C) and the point corresponding to the monophasic system is reported on the phase diagram. To ensure a proper determination of the required number of drops, the solution is vortexed after every drop addition. To study the system for a large range of compositions, the titration was carried out starting either from a stock solution of LiTFSI or LiCl. The proper junction between the two series of measurements observed in the phase diagram (Fig. 5.4, main text) validates the accuracy of the method.

A.3.4 Viscosity measurements and Jones-Dole coefficients for LiTFSI, LiCl, and KCl aqueous solutions

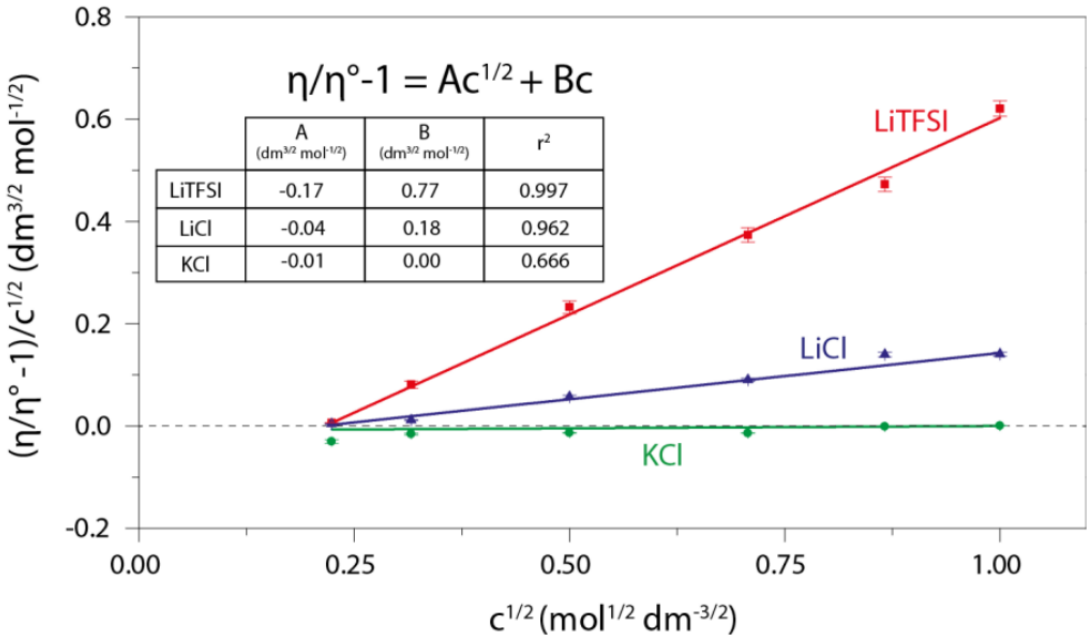

Figure A.13: Viscosity measurements for low concentrations (0 to 1 mol L^{-1}) aqueous solutions of LiTFSI (red), LiCl (blue) and KCl (green). Straight lines represent a linear fitting with the Jones-Dole equation.

As described in the main manuscript, the formation of an ABS using different salts was explained in the literature to result from the presence of water structuring (kosmotropic) ions in one phase and disorder-making (chaotropic) ions in the other phase. A common way to assess effect of individual ions on water structure is to measure the viscosity of dilute solutions (from 5 mM to 500 mM) and to determine the B-coefficient in the Jones-Dole equation ($\eta/\eta_{\text{water}} \ \ 1 = Ac^{1/2} + Bc$) by comparing with the results obtained for KCl, assuming the additivity of ionic contributions (and using the fact that B_{K^+} = -B_{Cl^-} , see below) [218, 220]. The viscosity measured for LiTFSI, LiCl, and KCl solutions from 50 mM to 1 M are well described by the Jones-Dole equation for the three salts, which allows us to determine the corresponding A and B parameters. An almost null B-coefficient is measured for KCl, for which it can be deduced B_{K^+} = -B_{Cl^-} = 0.00 $dm^{3/2}$ $mol^{-1/2}$. The positive B-coefficient of +0.18 $dm^{3/2}$ $mol^{-1/2}$ found for Li^+ cations indicates its water-structuring role (kosmotropic) and is in excellent

agreement with the literature (+0.15 $dm^{3/2}$ $mol^{-1/2}$ in reference [295]). Finally, the B-coefficient for $TFSI^-$ anions of +0.59 $dm^{3/2}$ $mol^{-1/2}$ can be deduced from the slope obtained for LiTFSI and the above value for Li^+. As discussed in the main text, such positive coefficients may indicates a kosmotropic effect for $TFSI^-$ anions, which may seem counter-intuitive based on previous reports [219, 296]. From reference [218], it can be concluded that this positive coefficient is rather due to the large size and hydrophobic character of $TFSI^-$ anions.

A.3.5 Dual ion battery using the ABS as electrolyte

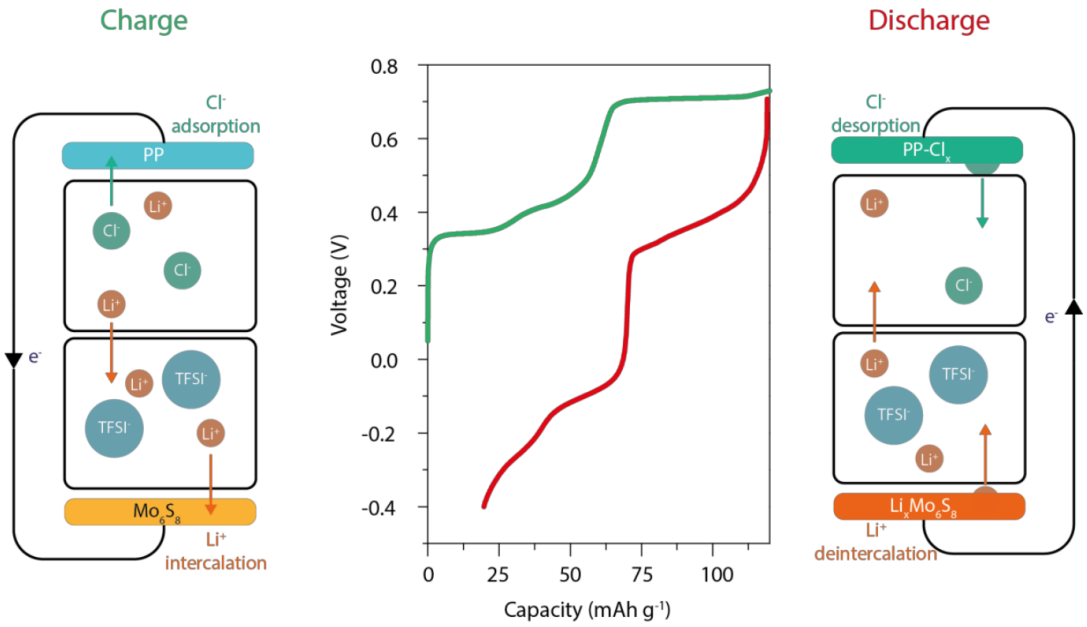

Figure A.14: First charge (green) and discharge (red) cycle obtained for a dual ion battery using a 20m LiTFSI-18m LiCl ABS electrolyte with a polypyrrole chlorine adsorption positive electrode and a Mo_6S_8 negative electrode. Capacity is expressed based on the Mo_6S_8 mass. Cycling was done at a C rate of 1 (1 mol of electron per hour), based on Mo_6S_8 mass.

This experiment confirms the possibility of using ABS to develop dual ion batteries with different anolytes and catholytes in absence of any membrane. The "water-in-salt" electrolyte (20 m LiTFSI) allows the cycling of Mo_6S_8 in aqueous electrolyte [214], while the 18 m LiCl electrolyte allows the PP electrode to work as a pseudo-capacitor for Cl^- ions [295]. In particular, the interface between the two phases remains stable even when an electric field is applied. Further improvements, such as stability of the

positive current collector in presence of Cl^- and reducing the large hysteresis observed in this preliminary experiment, would be required to assemble a practical dual ion battery based on ABS electrolytes.

A.4 Long range correlation length in concentrated electrolytes

Table A.8: Decay lengths λ_{sim} extracted from the fits of the simulated charge–charge correlation functions, $g_{ZZ}(r)$.

Concentration (mol/L)	λ_{sim} (nm)
LiCl(aq)	
0.2	0.61 ± 0.01
0.5	0.37 ± 0.04
1	0.16 ± 0.01
2	0.26 ± 0.02
5	0.31 ± 0.05
10	0.29 ± 0.02
NaI(aq)	
0.2	0.55 ± 0.01
0.5	0.24 ± 0.03
1	0.22 ± 0.04
2	0.27 ± 0.04
5	0.25 ± 0.03
10	0.25 ± 0.02
LiTFSI(aq)	
0.3	0.44 ± 0.09
1	0.37 ± 0.06
2.35	0.37 ± 0.08
3.54	0.37 ± 0.08
4.48	0.82 ± 0.06
4.85	0.96 ± 0.05
5.34	0.73 ± 0.04
LiTFSI(DME/DOL)	
0.25	0.28 ± 0.07
0.51	0.36 ± 0.07
0.98	0.56 ± 0.03
1.98	0.62 ± 0.06
3.1	0.51 ± 0.02
4.87	0.49 ± 0.02

A.4.1 Aqueous Sodium Iodide

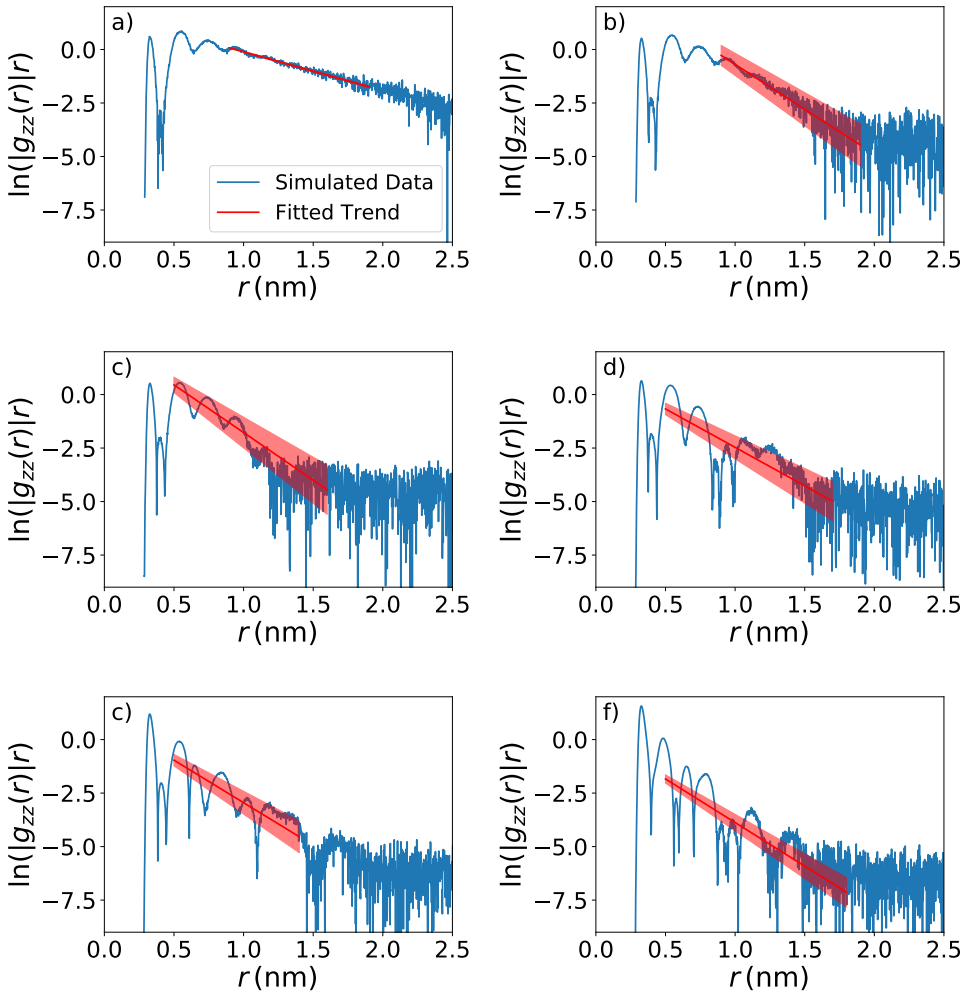

Figure A.15: Data from molecular dynamics simulations (blue), and fits to the them (red) of NaI (aq). Panels (a) to (f) are for concentrations: 0.2, 0.5, 1, 2, 5 and 10 mol/L. The shaded area illustrates uncertainty estimates on the slope, as described in the main text. The trend and the bounds of the shaded area converge at the y axis.

A.4.2 Aqueous Lithium Chloride

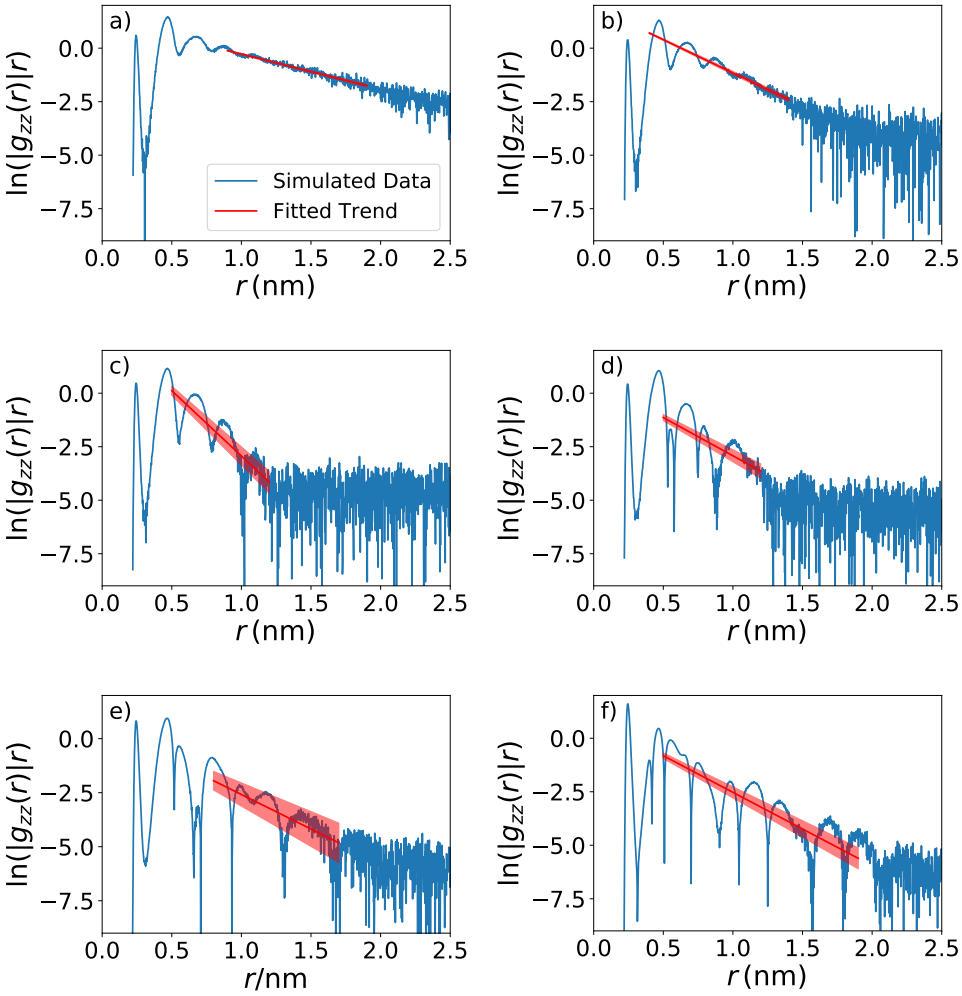

Figure A.16: Data from molecular dynamics simulations (blue), and fits to the them (red) of LiCl (aq). Panels (a) to (f) are for concentrations: 0.2, 0.5, 1, 2, 5 and 10 mol/L. The shaded area illustrates uncertainty estimates on the slope, as described in the main text. The trend and the bounds of the shaded area converge at the y axis.

A.4.3 Aqueous Lithium Bistriflimide

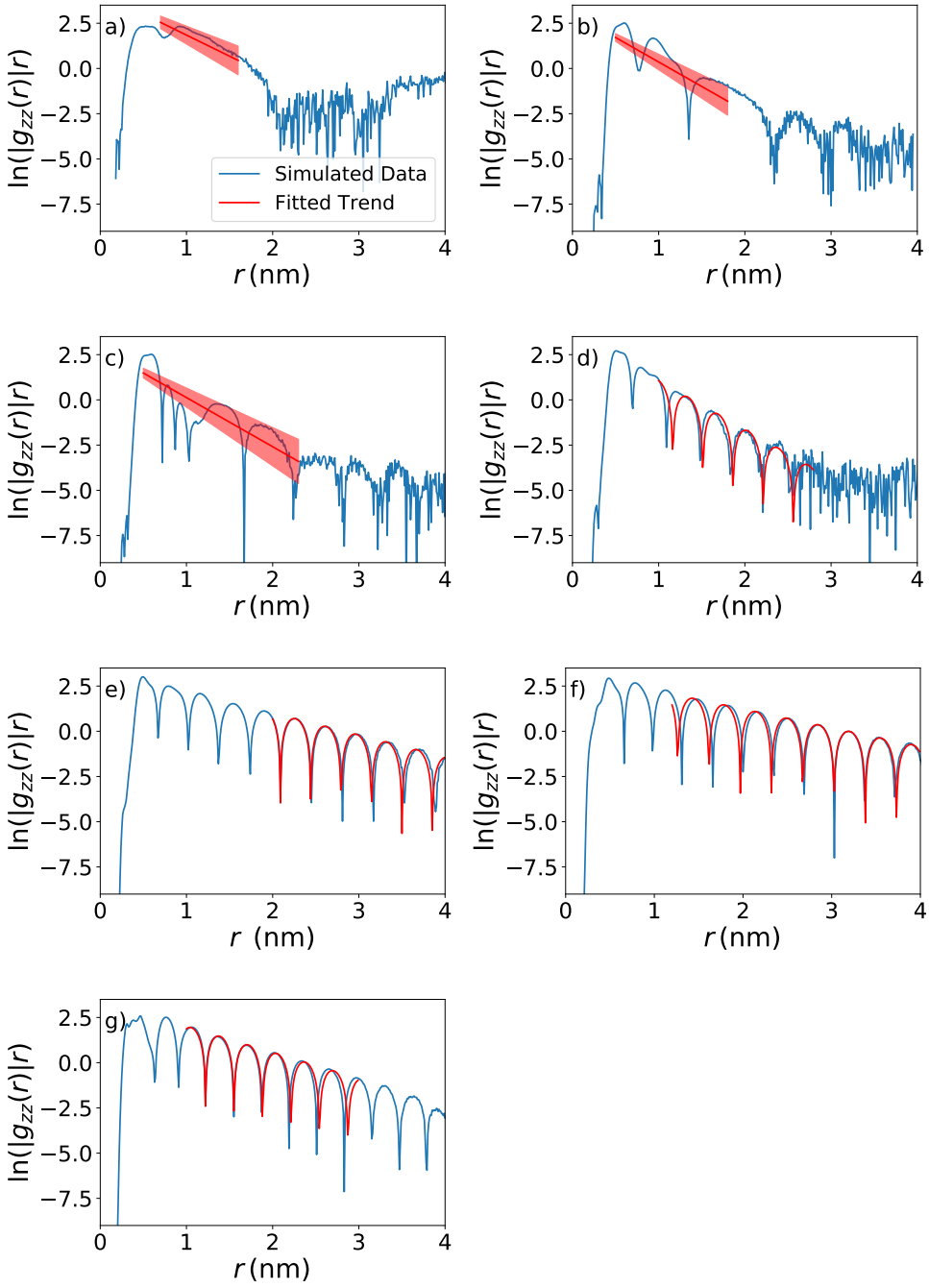

Figure A.17: Data from molecular dynamics simulations (blue), and fits to the them (red) of LiTFSI (aq). Panels (a) to (g) are for concentrations: 0.3, 1, 2.35, 3.54, 4.48, 4.85 and 5.34 mol/L. The shaded area illustrates uncertainty estimates on the slope, as described in the main text. The trend and the bounds of the shaded area converge at the y axis. Note that the reported distance range is larger for the higher concentrations.

A.4.4 Lithium Bistriflimide DME/DOL

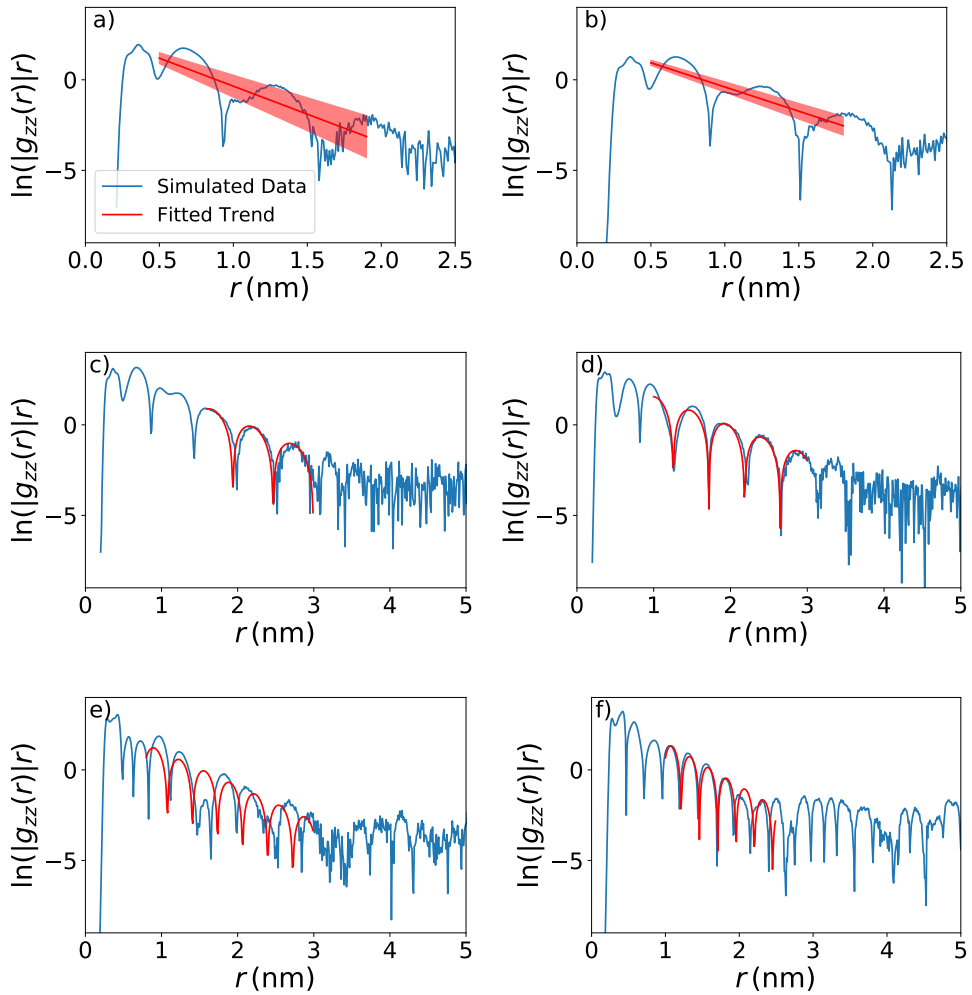

Figure A.18: Data from molecular dynamics simulations (blue), and fits to the them (red) of LiTFSI (DME/DOL). Panels (a) to (f) are for concentrations: 0.25, 0.51, 0.98, 1.98, 3.1 and 4.87 mol/L. The shaded area illustrates uncertainty estimates on the slope, as described in the main text. The trend and the bounds of the shaded area converge at the y axis.

Table A.9: Permittivities and corresponding Debye length for all simulated systems. The results are given both for the full calculation of the permittivity, including rotational and translational components as computed by the Einstein-Helfand method, and considering only the rotational component (the latter case is indicated with the "rot" superscript). The average relative error for ε_r (resp. $\varepsilon_r^{\mathrm{rot}}$) is 0.06 (resp. 0.05), which results in an average relative error for λ_{D} (resp. $\lambda_{\mathrm{D}}^{\mathrm{rot}}$) of 0.03 (resp. 0.02).

Concentration (mol/L)	ε_r	λ_{D} (nm)	$\varepsilon_r^{\mathrm{rot}}$	$\lambda_{\mathrm{D}}^{\mathrm{rot}}$ (nm)
LiCl(aq)				
0.2	81	0.69	68	0.63
0.5	77	0.43	63	0.39
1	66	0.28	54	0.25
2	56	0.18	43	0.16
5	40	0.10	11	0.07
10	23	0.05	9.1	0.03
NaI(aq)				
0.2	73	0.66	67	0.63
0.5	68	0.40	62	0.38
1	58	0.26	54	0.25
2	47	0.17	42	0.16
5	36	0.09	22	0.09
10	15	0.04	12	0.04
LiTFSI(aq)				
0.3	65	0.51	62	0.49
1	56	0.26	50	0.24
2.35	33	0.13	25	0.11
3.54	18	0.08	13	0.08
4.48	11	0.06	6.0	0.06
4.85	9.0	0.05	7.8	0.05
5.34	11	0.05	3.9	0.05
LiTFSI(DME/DOL)				
0.25	10	0.22	7.7	0.19
0.51	10	0.16	7.4	0.13
0.98	8.9	0.10	6.8	0.09
1.98	8.7	0.07	5.7	0.06
3.1	8.4	0.06	5.1	0.05
4.87	7.0	0.04	3.9	0.03

A.4.5 Extrapolation of $d_{\mathbf{vol}}$

In order to scale the screening length relative to ion size we have extrapolated from ion concentrations to calculate the mean ion diameter from the volume per an ion pair, as shown in Figure A.19. The calculated mean ion diameters are 0.255 nm for LiCl, 0.275 nm for NaI, and 0.375 nm and 0.38 nm for LiTFSI in water and DME/DOL.

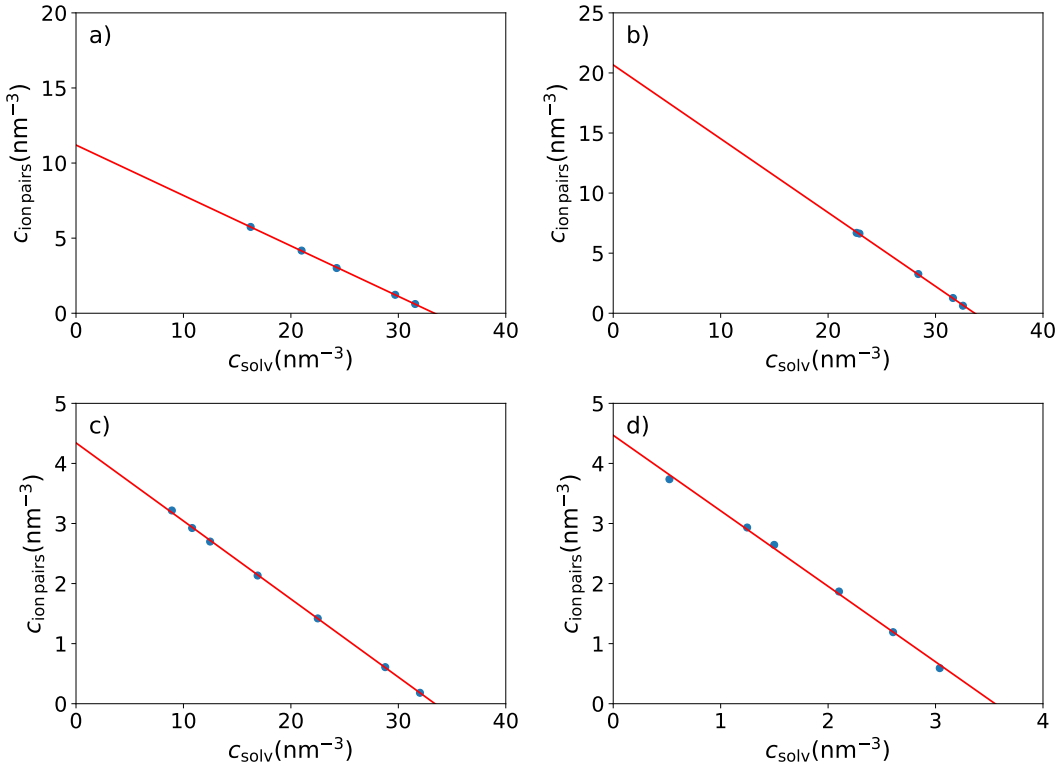

Figure A.19: Linear extrapolation of ion concentrations of: NaI (aq) (a), LiCl (aq) (b), LiTFSI (aq) (c), and LiTFSI (DME:DOL) (d). These plots allow for the calculation of volume per ion pair. The linear extrapolation is shown in red while the values of the simulated systems are shown in blue. The concentrations are in ions or molecules per cubic nanometer.

A.4.6 Decay lengths and wavelengths

Two different types of fit were used to extract decay lengths from charge-charge correlation functions, more precisely from $\ln(|g_{zz}(r)|r)$: linear fit where the oscillatory structure was irregular or the decay was linear, or oscillatory decay (see the expression in the main text). The screening lengths calculated from the simulations described in chapter 6 are plotted in Figure A.20 as a function of concentration and listed in Table A.8. The plots from which decay lengths were extracted are reported in the following. MD data are indicated in blue, while fits are shown in red. Table A.10 summarizes the wavelength extracted from the oscillatory fits, for the corresponding systems.

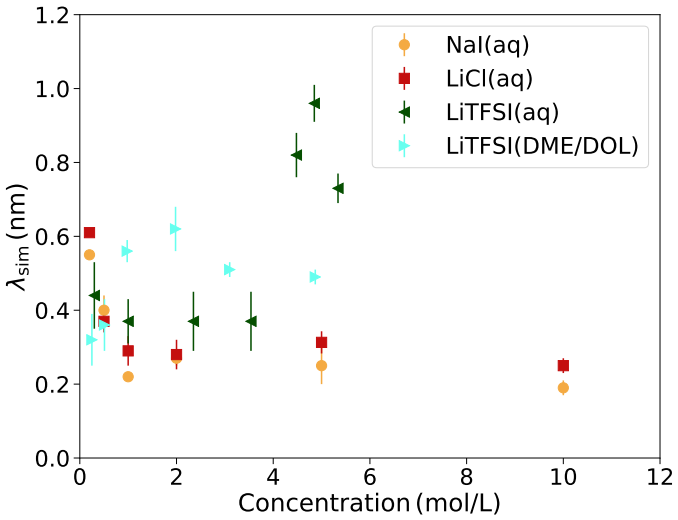

Figure A.20: Simulated decay lengths (λ_{sim}) for all systems, as a function of salt concentration. The shaded area illustrates uncertainty estimates on the slope, as described in the main text. All decay lengths obtained by in the present molecular simulations are smaller by a factor of 2 to 10 compared to those reported from Surface Force Balance experiments in Ref. [249].

Table A.10: Oscillatory wavelengths l_{sim} extracted from the fits of the simulated charge–charge correlation functions, $g_{ZZ}(r)$.

Concentration (mol/L)	l_{sim} (nm)
LiTFSI(aq)	
2.35	1.1
3.54	0.70
4.48	0.70
4.85	0.70
5.34	0.66
LiTFSI(DME/DOL)	
0.98	1.10
1.98	0.93
3.1	0.60
4.87	0.50

A.4.7 Effect of box size on the charge-charge correlation function In

In order to investigate possible finite size effects preventing the correct extraction of the screening length, we carried out simulations for a variety of box sizes and found no significant effect on the radial distribution functions for the considered box size. This is illustrated in Fig. A.21 for 0.98 mol/L LiTFSI in DME/DOL, simulated as described in the main paper, but changing the box size (5.5, 8.7 and 10.96 nm). For the smaller box sizes, simulation lengths where 100 and 130 ns, respectively.

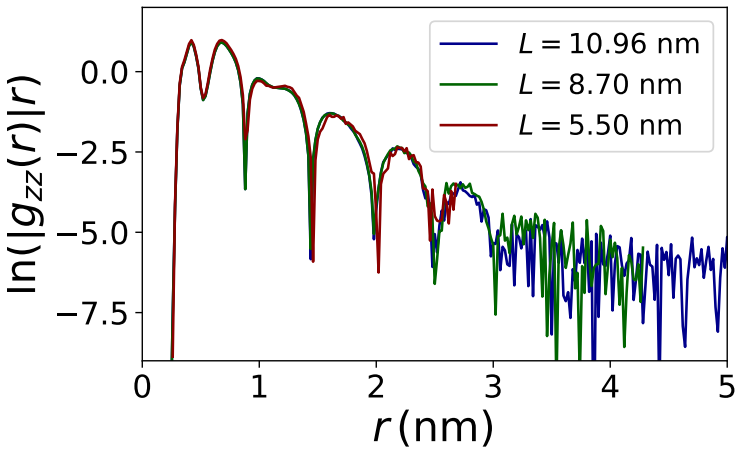

Figure A.21: $\ln(|g_{ZZ}(r)|r)$ for 0.98 mol/L LiTFSI in DME/DOL, using three box sizes L (see legend).

List of tables

List of figures

List of abbreviations

ABS Aqueous Biphasic Systems

CIP Contact Ion Pair

CSI Chemical Shift Imaging

DFT Density Functional Theory

DH Debye–Hückel

DME 1,2-dimethoxyethane

DN Gutmann donor number

DOL 1,3-dioxolane

ECC Electronic Continuum Correction

FF Force Fields

FTIR Fourier-Transform Infrared

HZB Helmholtz-Zentrum Berlin

IEES Institute for Electrochemical Energy Storage

Li/S Lithium-sulfur

LiTFSI Lithium bis(trifluoromethanesulfonyl)imide

LJ Lennard-Jones

MD Molecular Dynamics

MSA Mean Spherical Approximation

MSD Mean Square Displacement

NE Nernst–Einstein

NMR Nuclear Magnetic Resonance

OZ Ornstein-Zernike

PME Particle-Mesh-Ewald

PS Polysulfides

RHS Right-Hand Side

RPM Restricted Primitive Model

SEI Solid-Electrolyte Interface

SSIPs Solvent-Separated Ion Pairs

THF Tetrahydrofuran

Bibliography

[1] J. He and A. Manthiram. "A review on the status and challenges of electrocatalysts in lithium-sulfur batteries". *Energy Storage Materials* (2019).

[2] S. B.W. D. Brudermüller M. "A vision for a sustainable battery value chain in 2030". *World economic forum* (2019).

[3] A. Fotouhi et al. "A review on electric vehicle battery modelling: From Lithium-ion toward Lithium–Sulphur". *Renewable and Sustainable Energy Reviews* 56 (2016), pp. 1008–1021.

[4] M. Li and J. Lu. "Cobalt in lithium-ion batteries". *Science* 367.6481 (2020), pp. 979–980.

[5] L. Gaines, P. Nelson, et al. "Lithium-ion batteries: possible materials issues". *13th international battery materials recycling seminar and exhibit, Broward County Convention Center, Fort Lauderdale, Florida*. 2009, p. 16.

[6] J. B. Goodenough and K.-S. Park. "The Li-ion rechargeable battery: a perspective". *Journal of the American Chemical Society* 135.4 (2013), pp. 1167–1176.

[7] X. Zhang et al. "Direct view on the phase evolution in individual $LiFePO_4$ nanoparticles during Li-ion battery cycling". *Nature communications* 6.1 (2015), pp. 1–7.

[8] X. Zuo et al. "Silicon based lithium-ion battery anodes: A chronicle perspective review". *Nano Energy* 31 (2017), pp. 113–143.

[9] J. S. Newman and C. W. Tobias. "Theoretical analysis of current distribution in porous electrodes". *Journal of The Electrochemical Society* 109.12 (1962), p. 1183.

[10] D. R. Wheeler et al. "Modeling of lithium-ion batteries Modeling of lithium-ion batteries". 7753.June 2003 (2014).

[11] P. Biesheuvel, Y. Fu, and M. Z. Bazant. "Diffuse charge and Faradaic reactions in porous electrodes". *Physical Review E* 83.6 (2011), p. 061507.

[12] A. Latz and J. Zausch. "Thermodynamic consistent transport theory of Li-ion batteries". *Journal of Power Sources* 196.6 (2011), pp. 3296–3302.

[13] S. Clark, A. Latz, and B. Horstmann. "Rational development of neutral aqueous electrolytes for zinc–air batteries". *ChemSusChem* 10.23 (2017), pp. 4735–4747.

[14] J. Newman and W. Tiedemann. "Porous-electrode theory with battery applications". *AIChE Journal* 21.1 (1975), pp. 25–41.

[15] B. Jache and P. Adelhelm. "Use of graphite as a highly reversible electrode with superior cycle life for sodium-ion batteries by making use of co-intercalation phenomena". *Angewandte Chemie International Edition* 53.38 (2014), pp. 10169–10173.

[16] M. Safari, C. Y. Kwok, and L. F. Nazar. "Transport properties of polysulfide species in lithium–sulfur battery electrolytes: coupling of experiment and theory". *ACS Cent. Sci.* 2.8 (2016), pp. 560–568.

[17] M. Z. Bazant. "Theory of chemical kinetics and charge transfer based on nonequilibrium thermodynamics". *Accounts of chemical research* 46.5 (2013), pp. 1144–1160.

[18] L. Suo et al. "A new class of solvent-in-salt electrolyte for high-energy rechargeable metallic lithium batteries". *Nat. Commun.* 4 (2013), p. 1481.

[19] C. Zhang et al. "Chelate effects in glyme/lithium bis (trifluoromethanesulfonyl) amide solvate ionic liquids, part 2: importance of solvate-structure stability for electrolytes of lithium batteries". *J. Phys. Chem. C* 118.31 (2014), pp. 17362–17373.

[20] F. Y. Fan et al. "Solvent effects on polysulfide redox kinetics and ionic conductivity in lithium-sulfur batteries". *J. Electrochem. Soc.* 163.14 (2016), A3111–A3116.

[21] L. Medenbach and P. Adelhelm. "Cell Concepts of Metal-Sulfur Batteries (Metal 5 Li, Na, K, Mg): Strategies for Using Sulfur in Energy Storage Applications". *Electrochemical Energy Storage*. Springer, 2019, pp. 101–125.

[22] D. Sharon et al. "Aprotic metal-oxygen batteries: recent findings and insights". *Journal of Solid State Electrochemistry* 21.7 (2017), pp. 1861–1878.

[23] C. Xu et al. "Secondary batteries with multivalent ions for energy storage". *Scientific reports* 5 (2015), p. 14120.

[24] R. Kjellander. "Focus Article: Oscillatory and long-range monotonic exponential decays of electrostatic interactions in ionic liquids and other electrolytes: The significance of dielectric permittivity and renormalized charges". *The Journal of Chemical Physics* 148.19 (2018), p. 193701.

[25] M. Z. Bazant, B. D. Storey, and A. A. Kornyshev. "Double layer in ionic liquids: Overscreening versus crowding". *Physical Review Letters* 106.4 (2011), p. 046102.

[26] M. McEldrew et al. "Theory of the double layer in water-in-salt electrolytes". *The journal of physical chemistry letters* 9.19 (2018), pp. 5840–5846.

[27] M Wild et al. "Lithium sulfur batteries, a mechanistic review". *Energy & Environmental Science* 8.12 (2015), pp. 3477–3494.

[28] R. Fang et al. "More reliable lithium-sulfur batteries: status, solutions and prospects". *Adv. Mater.* 29.48 (2017), p. 1606823.

[29] Y. Levin. "Electrostatic correlations: from plasma to biology". *Reports on progress in physics* 65.11 (2002), p. 1577.

[30] A. Diehl, M. C. Barbosa, and Y. Levin. "Charge renormalization and phase separation in colloidal suspensions". *Europhysics Letters* 53.1 (2001), pp. 86–92.

[31] K. E. Gutowski et al. "Controlling the aqueous miscibility of ionic liquids: aqueous biphasic systems of water-miscible ionic liquids and water-structuring salts for recycle, metathesis, and separations". *Journal of the American Chemical Society* 125.22 (2003), pp. 6632–6633.

[32] N. J. Bridges, K. E. Gutowski, and R. D. Rogers. "Investigation of aqueous biphasic systems formed from solutions of chaotropic salts with kosmotropic salts (salt–salt ABS)". *Green Chemistry* 9.2 (2007), pp. 177–183.

[33] M. G. Freire et al. "Aqueous biphasic systems: a boost brought about by using ionic liquids". *Chemical Society Reviews* 41.14 (2012), pp. 4966–4995.

[34] J. Hansen and I. McDonald. *Theory of Simple Liquids: with Applications to Soft Matter*. Elsevier Science, 2013.

[35] M. A. Gebbie et al. "Long-range electrostatic screening in ionic liquids". *Proceedings of the National Academy of Sciences* 112.24 (2015), pp. 7432–7437.

[36] C. S. Perez-Martinez, A. M. Smith, S. Perkin, et al. "Scaling analysis of the screening length in concentrated electrolytes". *Physical review letters* 119.2 (2017), p. 026002.

[37] S. Wenzel et al. "Room-temperature sodium-ion batteries: improving the rate capability of carbon anode materials by templating strategies". *Energy & Environmental Science* 4.9 (2011), pp. 3342–3345.

[38] P. K. Nayak et al. "Review on challenges and recent advances in the electrochemical performance of high capacity Li-and Mn-rich cathode materials for Li-ion batteries". *Advanced Energy Materials* 8.8 (2018), p. 1702397.

[39] N. Nitta et al. "Li-ion battery materials: present and future". *Materials today* 18.5 (2015), pp. 252–264.

[40] M. Hagen et al. "Lithium–sulfur cells: the gap between the state-of-the-art and the requirements for high energy battery cells". *Advanced Energy Materials* 5.16 (2015), p. 1401986.

[41] T. Cleaver et al. "Perspective–commercializing lithium sulfur batteries: Are we doing the right research?" *J. Electrochem. Soc.* 165.1 (2018), A6029–A6033.

[42] W. Kang et al. "A review of recent developments in rechargeable lithium–sulfur batteries". *Nanoscale* 8.37 (2016), pp. 16541–16588.

[43] D. Herbert and J. Ulam. *Electric Dry Cells and Storage Batteries*. U.S. Patent 3043896. Issued June 10, 1962.

[44] E. J. Cairns and H. Shimotake. "High-temperature batteries". *Science* 164.20 (1969), pp. 1347–1355.

[45] J. Dobson, F. McLarnon, and E. Cairns. "Voltammetry of lithium polysulfides at metal electrodes". *Journal of The Electrochemical Society* 133.8 (1986), pp. 1549–1554.

[46] E. J. Cairns and J. S. Dunning. "High-temperature batteries". *Progress in High Temperature Physics and Chemistry* 5 (1976).

[47] M. S. Whittingham. "Electrical energy storage and intercalation chemistry". *Science* 192.4244 (1976), pp. 1126–1127.

[48] *Organic electrolyte cells, U.S. Patent 3413154*. 1968.

[49] E Peled et al. "Lithium-sulfur battery: evaluation of dioxolane-based electrolytes". *Journal of the Electrochemical Society* 136.6 (1989), pp. 1621–1625.

[50] E Peled et al. "Rechargeable lithium sulfur battery". *Journal of Power Sources* 26 (1989), pp. 269–271.

[51] J. Gao et al. "Effects of liquid electrolytes on the charge–discharge performance of rechargeable lithium/sulfur batteries: electrochemical and in-situ X-ray absorption spectroscopic studies". *J. Phys. Chem. C* 115.50 (2011), pp. 25132–25137.

[52] N. A. Cañas et al. "In-situ X-ray diffraction studies of lithium–sulfur batteries". *Journal of Power Sources* 226 (2013), pp. 313–319.

[53] M. Cuisinier et al. "Sulfur speciation in Li–S batteries determined by operando X-ray absorption spectroscopy". *J. Phys. Chem. Lett.* 4.19 (2013), pp. 3227–3232.

[54] Y.-X. Yin et al. "Lithium–sulfur batteries: electrochemistry, materials, and prospects". *Angewandte Chemie International Edition* 52.50 (2013), pp. 13186–13200.

[55] T. Ould Ely et al. "Lithium–sulfur batteries: state of the art and future directions". *ACS Applied Energy Materials* 1.5 (2018), pp. 1783–1814.

[56] G. Zheng et al. "Hollow carbon nanofiber-encapsulated sulfur cathodes for high specific capacity rechargeable lithium batteries". *Nano letters* 11.10 (2011), pp. 4462–4467.

[57] X. Ji, K. T. Lee, and L. F. Nazar. "A highly ordered nanostructured carbon–sulphur cathode for lithium–sulphur batteries". *Nature materials* 8.6 (2009), p. 500.

[58] Y. Xu et al. "Confined sulfur in microporous carbon renders superior cycling stability in Li/S batteries". *Advanced Functional Materials* 25.27 (2015), pp. 4312–4320.

[59] L. Sun et al. "Super-aligned carbon nanotube/graphene hybrid materials as a framework for sulfur cathodes in high performance lithium sulfur batteries". *Journal of Materials Chemistry A* 3.10 (2015), pp. 5305–5312.

[60] X.-B. Cheng et al. "Aligned carbon nanotube/sulfur composite cathodes with high sulfur content for lithium–sulfur batteries". *Nano Energy* 4 (2014), pp. 65–72.

[61] X. Chen et al. "Sulfur-Impregnated, Sandwich-Type, Hybrid Carbon Nanosheets with Hierarchical Porous Structure for High-Performance Lithium-Sulfur Batteries". *Advanced energy materials* 4.13 (2014), p. 1301988.

[62] K. Mi et al. "Hierarchical carbon nanotubes with a thick microporous wall and inner channel as efficient scaffolds for lithium–sulfur batteries". *Advanced Functional Materials* 26.10 (2016), pp. 1571–1579.

[63] L. Ji et al. "Graphene oxide as a sulfur immobilizer in high performance lithium/sulfur cells". *Journal of the American Chemical Society* 133.46 (2011), pp. 18522–18525.

[64] D. Wei et al. "Synthesis of N-doped graphene by chemical vapor deposition and its electrical properties". *Nano letters* 9.5 (2009), pp. 1752–1758.

[65] X. Liang et al. “A highly efficient polysulfide mediator for lithium–sulfur batteries”. *Nature communications* 6 (2015), p. 5682.

[66] L. Xiao et al. “A soft approach to encapsulate sulfur: polyaniline nanotubes for lithium-sulfur batteries with long cycle life”. *Advanced materials* 24.9 (2012), pp. 1176–1181.

[67] X. Wang et al. “Sulfurized Polyacrylonitrile Cathodes with High Compatibility in Both Ether and Carbonate Electrolytes for Ultrastable Lithium–Sulfur Batteries”. *Advanced Functional Materials* (2019), p. 1902929.

[68] A. Bhargav et al. “Rationally Designed High-Sulfur-Content Polymeric Cathode Material for Lithium–Sulfur Batteries”. *ACS applied materials & interfaces* 11.6 (2019), pp. 6136–6142.

[69] K. Xie et al. “Fabrication of a novel TiO 2/S composite cathode for high performance lithium–sulfur batteries”. *RSC advances* 5.94 (2015), pp. 77348–77353.

[70] J. Liu et al. “SnO_2 as a high-efficiency polysulfide trap in lithium–sulfur batteries”. *Nanoscale* 8.28 (2016), pp. 13638–13645.

[71] Y. Zhang et al. “Novel V_2O_5/S composite cathode material for the advanced secondary lithium batteries”. *Solid State Ionics* 181.17-18 (2010), pp. 835–838.

[72] X. Liang et al. “Interwoven MXene Nanosheet/Carbon-Nanotube Composites as Li–S Cathode Hosts”. *Advanced Materials* 29.3 (2017), p. 1603040.

[73] C.-S. Kim et al. “Facile dry synthesis of sulfur-LiFePO4 core–shell composite for the scalable fabrication of lithium/sulfur batteries”. *Electrochemistry Communications* 32 (2013), pp. 35–38.

[74] T. An et al. “MnO modified carbon nanotubes as a sulfur host with enhanced performance in Li/S batteries”. *Journal of Materials Chemistry A* 4.33 (2016), pp. 12858–12864.

[75] H. Chen et al. “Ultrafine sulfur nanoparticles in conducting polymer shell as cathode materials for high performance lithium/sulfur batteries”. *Scientific reports* 3 (2013), p. 1910.

[76] S. Wei et al. "Metal–sulfur battery cathodes based on PAN–sulfur composites". *Journal of the American Chemical Society* 137.37 (2015), pp. 12143–12152.

[77] S. Moon, Y. H. Jung, and D. K. Kim. "Enhanced electrochemical performance of a crosslinked polyaniline-coated graphene oxide-sulfur composite for rechargeable lithium–sulfur batteries". *Journal of Power Sources* 294 (2015), pp. 386–392.

[78] F. Wu et al. "Sulfur/polythiophene with a core/shell structure: synthesis and electrochemical properties of the cathode for rechargeable lithium batteries". *The Journal of Physical Chemistry C* 115.13 (2011), pp. 6057–6063.

[79] Y. Zhang et al. "One-step synthesis of branched sulfur/polypyrrole nanocomposite cathode for lithium rechargeable batteries". *Journal of power sources* 208 (2012), pp. 1–8.

[80] J.-Q. Huang et al. "Ionic shield for polysulfides towards highly-stable lithium–sulfur batteries". *Energy & environmental science* 7.1 (2014), pp. 347–353.

[81] M. Agostini and J. Hassoun. "A lithium-ion sulfur battery using a polymer, polysulfide-added membrane". *Scientific reports* 5 (2015), p. 7591.

[82] C. Li et al. "Polysulfide-blocking microporous polymer membrane tailored for hybrid Li-sulfur flow batteries". *Nano letters* 15.9 (2015), pp. 5724–5729.

[83] Z. Wu et al. "Utmost limits of various solid electrolytes in all-solid-state lithium batteries: A critical review". *Renewable and Sustainable Energy Reviews* 109 (2019), pp. 367–385.

[84] Y. V. Mikhaylik and J. R. Akridge. "Polysulfide shuttle study in the Li/S battery system". *J. Electrochem. Soc.* 151.11 (2004), A1969–A1976.

[85] K. Kumaresan, Y. Mikhaylik, and R. E. White. "A mathematical model for a lithium–sulfur cell". *Journal of The Electrochemical Society* 155.8 (2008), A576–A582.

[86] A. F. Hofmann, D. N. Fronczek, and W. G. Bessler. "Mechanistic modeling of polysulfide shuttle and capacity loss in lithium–sulfur batteries". *Journal of Power Sources* 259 (2014), pp. 300–310.

[87] D. N. Fronczek and W. G. Bessler. "Insight into lithium–sulfur batteries: Elementary kinetic modeling and impedance simulation". *Journal of power sources* 244 (2013), pp. 183–188.

[88] T. Danner et al. "Modeling of nano-structured cathodes for improved lithium-sulfur batteries". *Electrochimica Acta* 184 (2015), pp. 124–133.

[89] M. Marinescu, T. Zhang, and G. J. Offer. "A zero dimensional model of lithium–sulfur batteries during charge and discharge". *Physical Chemistry Chemical Physics* 18.1 (2016), pp. 584–593.

[90] V. Thangavel et al. "A microstructurally resolved model for Li-S batteries assessing the impact of the cathode design on the discharge performance". *Journal of The Electrochemical Society* 163.13 (2016), A2817–A2829.

[91] Y. Ren et al. "Modeling of lithium-sulfur batteries incorporating the effect of Li2S precipitation". *Journal of Power Sources* 336 (2016), pp. 115–125.

[92] C. Xiong et al. "Mathematical modeling of the charging process of Li-S batteries by incorporating the size-dependent Li2S dissolution". *Electrochimica Acta* 296 (2019), pp. 954–963.

[93] A. Fotouhi et al. "Lithium–Sulfur Cell Equivalent Circuit Network Model Parameterization and Sensitivity Analysis". *IEEE Transactions on Vehicular Technology* 66.9 (2017), pp. 7711–7721.

[94] Z. Liu, A. Mistry, and P. P. Mukherjee. "Mesoscale Physicochemical Interactions in Lithium–Sulfur Batteries: Progress and Perspective". *Journal of Electrochemical Energy Conversion and Storage* 15.1 (2018).

[95] A. Mistry and P. P. Mukherjee. "Precipitation–Microstructure Interactions in the Li-Sulfur Battery Electrode". *The Journal of Physical Chemistry C* 121.47 (2017), pp. 26256–26264.

[96] B. Wang, S. M. Alhassan, and S. T. Pantelides. "Formation of large polysulfide complexes during the lithium-sulfur battery discharge". *Phys. Rev. Appl.* 2.3 (2014), p. 034004.

[97] P. Partovi-Azar, T. D. Kühne, and P. Kaghazchi. "Evidence for the existence of Li2S2 clusters in lithium–sulfur batteries: ab initio Raman spectroscopy simulation". *Phys. Chem. Chem. Phys.* 17.34 (2015), pp. 22009–22014.

[98] N. N. Rajput et al. "Elucidating the solvation structure and dynamics of lithium polysulfides resulting from competitive salt and solvent interactions". *Chem. Mater.* 29.8 (2017), pp. 3375–3379.

[99] A. Andersen et al. "Structure and dynamics of polysulfide clusters in a non-aqueous solvent mixture of 1, 3-dioxolane and 1, 2-dimethoxyethane". *Chem. Mater.* (2019).

[100] M. Abraham et al. *GROMACS development team, GROMACS user manual version 5.1. 4*. 2016.

[101] T. Darden, D. York, and L. Pedersen. "Particle Mesh Ewald: An N log(N) Method for Ewald Sums in Large Systems". *J. Chem. Phys.* 98.12 (1993), pp. 10089–10092.

[102] U. Essmann et al. "A Smooth Particle Mesh Ewald Method". *J. Chem. Phys.* 103.19 (1995), pp. 8577–8593.

[103] R. W. Hockney, S. Goel, and J. Eastwood. "Quiet high-resolution computer models of a plasma". *Journal of Computational Physics* 14.2 (1974), pp. 148–158.

[104] H. J. Berendsen et al. "Molecular dynamics with coupling to an external bath". *J. Chem. Phys.* 81.8 (1984), pp. 3684–3690.

[105] H. C. Andersen. "Molecular dynamics simulations at constant pressure and/or temperature". *The Journal of chemical physics* 72.4 (1980), pp. 2384–2393.

[106] S. Nosé. "A molecular dynamics method for simulations in the canonical ensemble". *Molecular physics* 52.2 (1984), pp. 255–268.

[107] W. G. Hoover. "Canonical dynamics: Equilibrium phase-space distributions". *Physical review A* 31.3 (1985), p. 1695.

[108] G. Bussi, D. Donadio, and M. Parrinello. "Canonical Sampling through Velocity Rescaling". *J. Chem. Phys.* 126.1, 014101 (2007), p. 014101.

[109] M. Parrinello and A. Rahman. "Polymorphic transitions in single crystals: A new molecular dynamics method". *Journal of Applied physics* 52.12 (1981), pp. 7182–7190.

[110] B. J. Alder and T. E. Wainwright. "Studies in molecular dynamics. I. General method". *The Journal of Chemical Physics* 31.2 (1959), pp. 459–466.

[111] J. A. Lemkul et al. "An empirical polarizable force field based on the classical drude oscillator model: development history and recent applications". *Chemical Reviews* 116.9 (2016), pp. 4983–5013.

[112] W. D. Cornell et al. "A Second Generation Force Field for the Simulation of Proteins, Nucleic Acids, and Organic Molecules". *J. Am. Chem. Soc.* 117 (1995), pp. 5179–5197.

[113] A. D. MacKerell Jr, J. Wiorkiewicz-Kuczera, and M. Karplus. "An all-atom empirical energy function for the simulation of nucleic acids". *Journal of the American Chemical society* 117.48 (1995), pp. 11946–11975.

[114] W. F. van Gunsteren et al. "Biomolecular simulation: the GROMOS96 manual and user guide". *Vdf Hochschulverlag AG an der ETH Zürich, Zürich* 86 (1996).

[115] W. L. Jorgensen, D. S. Maxwell, and J. Tirado-Rives. "Development and testing of the OPLS all-atom force field on conformational energetics and properties of organic liquids". *J. Am. Chem. Soc* 118.45 (1996), pp. 11225–11236.

[116] T. A. Halgren and W. Damm. "Polarizable force fields". *Current opinion in structural biology* 11.2 (2001), pp. 236–242.

[117] T. P. Lybrand and P. A. Kollman. "Water–water and water–ion potential functions including terms for many body effects". *The Journal of chemical physics* 83.6 (1985), pp. 2923–2933.

[118] P. E. Mason, E. Wernersson, and P. Jungwirth. "Accurate description of aqueous carbonate ions: An effective polarization model verified by neutron scattering". *J. Phys. Chem. B* 116.28 (2012), pp. 8145–8153.

[119] M. Vazdar, P. Jungwirth, and P. E. Mason. "Aqueous guanidinium–carbonate interactions by molecular dynamics and neutron scattering: relevance to ion–protein interactions". *J. Phys. Chem. B* 117.6 (2013), pp. 1844–1848.

[120] L. Pegado et al. "Solvation and ion-pairing properties of the aqueous sulfate anion: explicit versus effective electronic polarization". *Phys. Chem. Chem. Phys.* 14.29 (2012), pp. 10248–10257.

[121] I. Vorobyov et al. "Additive and classical drude polarizable force fields for linear and cyclic ethers". *Journal of chemical theory and computation* 3.3 (2007), pp. 1120–1133.

[122] C. Oostenbrink et al. "A biomolecular force field based on the free enthalpy of hydration and solvation: the GROMOS force-field parameter sets 53A5 and 53A6". *Journal of computational chemistry* 25.13 (2004), pp. 1656–1676.

[123] T. Simonson and D. Perahia. "Internal and interfacial dielectric properties of cytochrome c from molecular dynamics in aqueous solution". *Proceedings of the National Academy of Sciences* 92.4 (1995), pp. 1082–1086.

[124] G. A. Kaminski et al. "Development of an accurate and robust polarizable molecular mechanics force field from ab initio quantum chemistry". *The Journal of Physical Chemistry A* 108.4 (2004), pp. 621–627.

[125] S. Patel, A. D. Mackerell Jr, and C. L. Brooks III. "CHARMM fluctuating charge force field for proteins: II protein/solvent properties from molecular dynamics simulations using a nonadditive electrostatic model". *Journal of computational chemistry* 25.12 (2004), pp. 1504–1514.

[126] G. Lamoureux et al. "A polarizable model of water for molecular dynamics simulations of biomolecules". *Chemical Physics Letters* 418.1-3 (2006), pp. 245–249.

[127] P. E. Lopes et al. "Polarizable force field for peptides and proteins based on the classical drude oscillator". *Journal of chemical theory and computation* 9.12 (2013), pp. 5430–5449.

[128] J. W. Ponder et al. "Current status of the AMOEBA polarizable force field". *The journal of physical chemistry B* 114.8 (2010), pp. 2549–2564.

[129] A. G. Donchev et al. "Assessment of performance of the general purpose polarizable force field QMPFF3 in condensed phase". *Journal of computational chemistry* 29.8 (2008), pp. 1242–1249.

[130] A. Donchev et al. "A quantum mechanical polarizable force field for biomolecular interactions". *Proceedings of the National Academy of Sciences* 102.22 (2005), pp. 7829–7834.

[131] I. V. Leontyev and A. A. Stuchebrukhov. "Polarizable molecular interactions in condensed phase and their equivalent nonpolarizable models". *J. Chem. Phys.* 141.1 (2014), p. 014103.

[132] J. W. Ponder and D. A. Case. "Force fields for protein simulations". *Advances in protein chemistry*. Vol. 66. Elsevier, 2003, pp. 27–85.

[133] M. B. Gee et al. "A Kirkwood-Buff derived force field for aqueous alkali halides". *Journal of Chemical Theory and Computation* 7.5 (2011), pp. 1369–1380.

[134] S. Weerasinghe and P. E. Smith. "A Kirkwood–Buff derived force field for sodium chloride in water". *The Journal of chemical physics* 119.21 (2003), pp. 11342–11349.

[135] M. Fyta and R. R. Netz. "Ionic force field optimization based on single-ion and ion-pair solvation properties: Going beyond standard mixing rules". *The Journal of chemical physics* 136.12 (2012), p. 124103.

[136] E. E. Bruce and N. F. van der Vegt. "Does an electronic continuum correction improve effective short-range ion-ion interactions in aqueous solution?" *The Journal of chemical physics* 148.22 (2018), p. 222816.

[137] I. Leontyev and A. Stuchebrukhov. "Electronic continuum model for molecular dynamics simulations". *J. Chem. Phys.* 130.8 (2009), p. 085102.

[138] F. Coupette, A. Härtel, et al. "Screening lengths in ionic fluids". *Physical review letters* 121.7 (2018), p. 075501.

[139] R Evans et al. "Asymptotic decay of liquid structure: oscillatory liquid-vapour density profiles and the Fisher-Widom line". *Molecular Physics* 80.4 (1993), pp. 755–775.

[140] J.-P. Hansen and I. R. McDonald. *Theory of simple liquids*. Elsevier, 1990.

[141] R Evans et al. "Asymptotic decay of correlations in liquids and their mixtures". *The Journal of chemical physics* 100.1 (1994), pp. 591–603.

[142] C Schröder, M Haberler, and O Steinhauser. "On the computation and contribution of conductivity in molecular ionic liquids". *The Journal of chemical physics* 128.13 (2008), p. 134501.

[143] M. Chintapalli et al. "Relationship between conductivity, ion diffusion, and transference number in perfluoropolyether electrolytes". *Macromolecules* 49 (2016), pp. 3508–3515.

[144] B. Hess. "Determining the shear viscosity of model liquids from molecular dynamics simulations". *J. Chem. Phys.* 116.1 (2002), pp. 209–217.

[145] B. J. Palmer. "Transverse-current autocorrelation-function calculations of the shear viscosity for molecular liquids". *Phys. Rev. E* 49.1 (1994), p. 359.

[146] R. Fort and W. Moore. "Viscosities of binary liquid mixtures". *Trans. Faraday Soc.* 62 (1966), pp. 1112–1119.

[147] A. Rosenman et al. "Review on Li-sulfur battery systems: an Integral perspective". *Adv. Energy Mater.* 5.16 (2015).

[148] F. Schipper and D. Aurbach. "A brief review: Past, present and future of lithium ion batteries". *Russ. J. Electrochem.* 52.12 (2016), pp. 1095–1121.

[149] X. Ji and L. F. Nazar. "Advances in Li–S batteries". *J. Mater. Chem.* 20.44 (2010), pp. 9821–9826.

[150] J. Scheers, S. Fantini, and P. Johansson. "A review of electrolytes for lithium–sulphur batteries". *J. Power Sources* 255 (2014), pp. 204–218.

[151] E. S. Shin et al. "Polysulfide dissolution control: the common ion effect". *Chem. Commun.* 49.20 (2013), pp. 2004–2006.

[152] M Vijayakumar et al. "Molecular structure and stability of dissolved lithium polysulfide species". *Phys. Chem. Chem. Phys.* 16.22 (2014), pp. 10923–10932.

[153] M. Barghamadi et al. "Lithium–sulfur batteries—the solution is in the electrolyte, but is the electrolyte a solution?" *Energy & Environ Sci.* 7.12 (2014), pp. 3902–3920.

[154] Q. Li et al. "Progress in electrolytes for rechargeable Li-based batteries and beyond". *Green Energy & Environment* 1.1 (2016), pp. 18–42.

[155] K. Xu. "Nonaqueous liquid electrolytes for lithium-based rechargeable batteries". *Chem. Rev.* 104.10 (2004), pp. 4303–4418.

[156] Z. Li et al. "Effect of Organic Solvents on Li^+ Ion Solvation and Transport in Ionic Liquid Electrolytes: A Molecular Dynamics Simulation Study". *J. Phys. Chem. B* 119.7 (2015), pp. 3085–3096.

[157] O. Borodin and G. D. Smith. "LiTFSI Structure and Transport in Ethylene Carbonate from Molecular Dynamics Simulations". *J. Phys. Chem. B* 110 (2006), pp. 4971–4977.

[158] D. M. Seo et al. "Solvate structures and spectroscopic characterization of LiTFSI electrolytes". *J. Phys. Chem. B* 118.47 (2014), pp. 13601–13608.

[159] V. Lesch et al. "The influence of cations on lithium ion coordination and transport in ionic liquid electrolytes: a MD simulation study". *Phys. Chem. Chem. Phys.* 18.1 (2016), pp. 382–392.

[160] K. Hayamizu et al. "Pulse-gradient spin-echo ^1H, ^7Li, and ^{19}F NMR diffusion and ionic conductivity measurements of 14 organic electrolytes containing $LiN(SO_2CF_3)_2$". *J. Phys. Chem. B* 103.3 (1999), pp. 519–524.

[161] S. Risse et al. "Multidimensional operando analysis of macroscopic structure evolution in lithium sulfur cells by X-ray radiography". *Phys. Chem. Chem. Phys.* 18 (2016), pp. 10630–10636.

[162] S. J. Keasler et al. "Transferable Potentials for Phase Equilibria–United Atom Description of Five-and Six-Membered Cyclic Alkanes and Ethers". *J. Phys. Chem. B* 116.36 (2012), pp. 11234–11246.

[163] P. M. Anderson and M. R. Wilson. "Developing a force field for simulation of poly (ethylene oxide) based upon ab initio calculations of 1, 2-dimethoxyethane". *Mol. Phys.* 103.1 (2005), pp. 89–97.

[164] I. Leontyev et al. "Continuum level treatment of electronic polarization in the framework of molecular simulations of solvation effects". *J. Chem. Phys.* 119.15 (2003), pp. 8024–8037.

[165] I. Leontyev and A. Stuchebrukhov. "Electronic polarizability and the effective pair potentials of water". *J. Chem. Theory Comput.* 6.10 (2010), pp. 3153–3161.

[166] I. Leontyev and A. Stuchebrukhov. "Electronic continuum model for molecular dynamics simulations of biological molecules". *J. Chem. Theory Comput.* 6.5 (2010), pp. 1498–1508.

[167] I. Leontyev and A. Stuchebrukhov. "Accounting for electronic polarization in non-polarizable force fields". *Phys. Chem. Chem. Phys.* 13.7 (2011), pp. 2613–2626.

[168] I. V. Leontyev and A. A. Stuchebrukhov. "Polarizable mean-field model of water for biological simulations with AMBER and CHARMM force fields". *J. Chem. Theory Comput.* 8.9 (2012), pp. 3207–3216.

[169] Y. Marcus. *The properties of solvents*. Vol. 16. Wiley Chichester, 1998.

[170] J. N. Canongia Lopes and A. A. Pádua. "Molecular force field for ionic liquids composed of triflate or bistriflylimide anions". *J. Phys. Chem. B* 108.43 (2004), pp. 16893–16898.

[171] T. Méndez-Morales et al. "Solvation of lithium salts in protic ionic liquids: a molecular dynamics study". *J. Phys. Chem. B* 118.3 (2014), pp. 761–770.

[172] L. X. Dang. "Development of nonadditive intermolecular potentials using molecular dynamics: solvation of Li^+ and F^- ions in polarizable water". *J. Chem. Phys.* 96.9 (1992), pp. 6970–6977.

[173] B. B. Gurung and M. N. Roy. "Study of densities, viscosities and ultrasonic speeds of binary mixtures containing 1, 2-dimethoxyethane and an alkan-l-ol at 298.15 K". *J. Solution Chem.* 35.12 (2006), pp. 1587–1606.

[174] B Giner et al. "Viscosities of binary mixtures of 1, 3-dioxolane or 1, 4-dioxane with isomeric chlorobutanes". *J. Mol. Liq.* 129.3 (2006), pp. 176–180.

[175] D. Brouillette et al. "Stable solvates in solution of lithium bis (trifluoromethylsulfone) imide in glymes and other aprotic solvents: Phase diagrams, crystallography and Raman spectroscopy". *Phys. Chem. Chem. Phys.* 4.24 (2002), pp. 6063–6071.

[176] W. A. Henderson. "Glyme- lithium salt phase behavior". *J. Phys. Chem. B* 110.26 (2006), pp. 13177–13183.

[177] V. Chaban. "Solvation of lithium ion in dimethoxyethane and propylene carbonate". *Chem. Phys. Lett.* 631 (2015), pp. 1–5.

[178] F. Cataldo. "A revision of the Gutmann donor numbers of a series of phosphoramides including TEPA". *European Chemical Bulletin* 4.1-3 (2015), pp. 92–97.

[179] V Gutmann. "Empirical parameters for donor and acceptor properties of solvents". *Electrochim. Acta* 21.9 (1976), pp. 661–670.

[180] J. Zheng et al. "Ionic liquid-enhanced solid state electrolyte interface (SEI) for lithium–sulfur batteries". *J. Mater. Chem. A* 1.29 (2013), pp. 8464–8470.

[181] H.-S. Kim and C.-S. Jeong. "Electrochemical properties of binary electrolytes for lithium-sulfur batteries". *Bull. Korean Chem. Soc.* 32.10 (2011), pp. 3682–3686.

[182] K. H. Wujcik et al. "Characterization of polysulfide radicals present in an ether-based electrolyte of a lithium–sulfur battery during initial discharge using in situ X-ray absorption spectroscopy experiments and first-principles calculations". *Adv. Energy Mater.* 5.16 (2015).

[183] J.-W. Park et al. "Solvent effect of room temperature ionic liquids on electrochemical reactions in lithium–sulfur batteries". *J. Phys. Chem. C* 117.9 (2013), pp. 4431–4440.

[184] H. Pan et al. "On the way toward understanding solution chemistry of lithium polysulfides for high energy Li–S redox flow batteries". *Adv. Energy Mater.* 5.16 (2015), p. 1500113.

[185] D. Zheng et al. "Quantitative chromatographic determination of dissolved elemental sulfur in the non-aqueous electrolyte for lithium-sulfur batteries". *J. Electrochem. Soc.* 162.1 (2015), A203–A206.

[186] S.-H. Yu et al. "Direct visualization of sulfur cathodes: new insights into Li–S batteries via operando X-ray based methods". *Energy Environ. Sci.* 11.1 (2018), pp. 202–210.

[187] M. Frisch et al. *Official Gaussian 09 literature citation.* 2014.

[188] E. J. Sorin and V. S. Pande. "Exploring the helix-coil transition via all-atom equilibrium ensemble simulations". *Biophys. J.* 88.4 (2005), pp. 2472–2493.

[189] A. D. MacKerell Jr et al. "All-atom empirical potential for molecular modeling and dynamics studies of proteins". *J. Phys. Chem. B* 102.18 (1998), pp. 3586–3616.

[190] M. Levitt et al. "Potential energy function and parameters for simulations of the molecular dynamics of proteins and nucleic acids in solution". *Comput. Phys. Commun.* 91.1-3 (1995), pp. 215–231.

[191] G. Nemethy, M. S. Pottle, and H. A. Scheraga. "Energy parameters in polypeptides. 9. Updating of geometrical parameters, nonbonded interactions, and hydrogen bond interactions for the naturally occurring amino acids". *J. Phys. Chem.* 87.11 (1983), pp. 1883–1887.

[192] A. K. Rappé et al. "UFF, a full periodic table force field for molecular mechanics and molecular dynamics simulations". *J. Am. Chem. Soc* 114.25 (1992), pp. 10024–10035.

[193] S. L. Mayo, B. D. Olafson, and W. A. Goddard. "DREIDING: a generic force field for molecular simulations". *J. Phys. Chem.* 94.26 (1990), pp. 8897–8909.

[194] C. Barchasz et al. "Lithium/sulfur cell discharge mechanism: an original approach for intermediate species identification". *Anal. Chem.* 84.9 (2012), pp. 3973–3980.

[195] D. Ben-Yaakov, D. Andelman, and R. Podgornik. "Dielectric decrement as a source of ion-specific effects". *J. Chem. Phys.* 134.7 (2011), p. 074705.

[196] E Glueckauf. "Bulk dielectric constant of aqueous electrolyte solutions". *J. Chem. Soc. Faraday Trans.* 60 (1964), pp. 1637–1645.

[197] Y.-Z. Wei, P. Chiang, and S Sridhar. "Ion size effects on the dynamic and static dielectric properties of aqueous alkali solutions". *J. Chem. Phys.* 96.6 (1992), pp. 4569–4573.

[198] A. Chandra. "Static dielectric constant of aqueous electrolyte solutions: Is there any dynamic contribution?" *J. Chem. Phys.* 113.3 (2000), pp. 903–905.

[199] E. P. Kamphaus and P. B. Balbuena. "First-principles investigation of lithium polysulfide structure and behavior in solution". *J. Phys. Chem. C* 121.39 (2017), pp. 21105–21117.

[200] K. S. Han et al. "Effects of anion mobility on electrochemical behaviors of lithium–sulfur batteries". *Chem. Mater.* 29.21 (2017), pp. 9023–9029.

[201] C. Park et al. "Molecular simulations of electrolyte structure and dynamics in lithium–sulfur battery solvents". *J. Power Sources* 373 (2018), pp. 70–78.

[202] A. Altenberger and H. L. Friedman. "Theory of conductance and related isothermal transport coefficients in electrolytes". *J. Chem. Phys.* 78.6 (1983), pp. 4162–4173.

[203] J. Zheng et al. "How to obtain reproducible results for lithium sulfur batteries?" *J. Electrochem. Soc.* 160.11 (2013), A2288–A2292.

[204] E. Pluhařová, P. E. Mason, and P. Jungwirth. "Ion pairing in aqueous lithium salt solutions with monovalent and divalent counter-anions". *J. Phys. Chem. A* 117.46 (2013), pp. 11766–11773.

[205] J. N. Israelachvili. *Intermolecular and surface forces*. Academic press, 2011.

[206] T. A. Pascal et al. "Thermodynamic origins of the solvent-dependent stability of lithium polysulfides from first principles". *Phys. Chem. Chem. Phys.* 19.2 (2017), pp. 1441–1448.

[207] N. Ding et al. "In situ monitoring the viscosity change of an electrolyte in a Li–S battery". *ChemComm* 53.73 (2017), pp. 10152–10155.

[208] S. Osella et al. "Modelling coupled ion motion in electrolyte solutions for lithium-sulfur batteries". *Batteries & Supercaps* ().

[209] A. Shyamsunder et al. "Inhibiting polysulfide shuttle in lithium–sulfur batteries through low-ion-pairing salts and a triflamide solvent". *Angew. Chem.* 56.22 (2017), pp. 6192–6197.

[210] J. Chen et al. "Restricting the solubility of polysulfides in Li-S batteries via electrolyte salt selection". *Adv. Energy Mater.* 6.11 (2016), p. 1600160.

[211] M. I. Chaudhari et al. "Assessment of simple models for molecular simulation of ethylene carbonate and propylene carbonate as solvents for electrolyte solutions". *Top. Curr. Chem.* 376.2 (2018), p. 7.

[212] V. Lesch et al. "A combined theoretical and experimental study of the influence of different anion ratios on lithium ion dynamics in ionic liquids". *J. Phys. Chem. B* 118.26 (2014), pp. 7367–7375.

[213] M. Beijerinck. "Über eine Eigentümlichkeit der löslichen Stärke". *Zentralblatt for Bakteriologie, Parasiten und Infektionskrankheiten* 2 (1896), pp. 679–699.

[214] L. Suo et al. ""Water-in-salt" electrolyte enables high-voltage aqueous lithium-ion chemistries". *Science* 350.6263 (2015), pp. 938–943.

[215] Y. Yamada et al. “Hydrate-melt electrolytes for high-energy-density aqueous batteries”. *Nature Energy* 1.10 (2016), p. 16129.

[216] L. Suo et al. “Advanced high-voltage aqueous lithium-ion battery enabled by "water-in-bisalt" electrolyte”. *Angewandte Chemie International Edition* 55.25 (2016), pp. 7136–7141.

[217] P. C. Howlett et al. “Electrochemistry at negative potentials in bis (trifluoromethanesulfonyl) amide ionic liquids”. *Zeitschrift für Physikalische Chemie* 220.10 (2006), pp. 1483–1498.

[218] H. D. B. Jenkins and Y. Marcus. “Viscosity B-coefficients of ions in solution”. *Chemical reviews* 95.8 (1995), pp. 2695–2724.

[219] H.-L. Su et al. “Chaotropic salts: Novel modifiers for the capillary electrophoretic analysis of benzodiazepines”. *Electrophoresis* 29.16 (2008), pp. 3384–3390.

[220] Y. Marcus. “Effect of ions on the structure of water: structure making and breaking”. *Chemical reviews* 109.3 (2009), pp. 1346–1370.

[221] O. Borodin et al. “Liquid structure with nano-heterogeneity promotes cationic transport in concentrated electrolytes”. *ACS nano* 11.10 (2017), pp. 10462–10471.

[222] A. Levy, M. McEldrew, and M. Z. Bazant. “Spin-glass charge ordering in ionic liquids”. *Physical Review Materials* 3.5 (2019), p. 055606.

[223] F. L. Celso, A Triolo, and R Triolo. “Phase separation in multi-component mixtures: the four-component case”. *Physica A: Statistical Mechanics and its Applications* 304.1-2 (2002), pp. 299–307.

[224] O Kuzmina et al. “Solubility of alkali metal halides in the ionic liquid [C4C1im][OTf]”. *Physical Chemistry Chemical Physics* 18.24 (2016), pp. 16161–16168.

[225] P. Navalpotro et al. “Pioneering Use of Ionic Liquid-Based Aqueous Biphasic Systems as Membrane-Free Batteries”. *Advanced Science* 5.10 (2018), p. 1800576.

[226] B. Uralcan et al. "Concentration fluctuations and capacitive response in dense ionic solutions". *The journal of physical chemistry letters* 7.13 (2016), pp. 2333–2338.

[227] D. T. Limmer. "Interfacial ordering and accompanying divergent capacitance at ionic liquid-metal interfaces". *Physical review letters* 115.25 (2015), p. 256102.

[228] D. J. Bozym et al. "Anomalous capacitance maximum of the glassy carbon–ionic liquid interface through dilution with organic solvents". *The journal of physical chemistry letters* 6.13 (2015), pp. 2644–2648.

[229] N. B. Ludwig et al. "Describing screening in dense ionic fluids with a charge-frustrated Ising model". *The Journal of chemical physics* 149.16 (2018), p. 164505.

[230] V. Bagoëtìskiæi. *Fundamentals of electrochemistry*. 2006.

[231] J. G. Kirkwood. "Statistical Mechanics of Liquid Solutions." *Chem. Rev.* 19.3 (Dec. 1936), pp. 275–307.

[232] M. E. Fisher and B Wiodm. "Decay of correlations in linear systems". *The Journal of Chemical Physics* 50.9 (1969), pp. 3756–3772.

[233] R. Evans and T. J. Sluckin. "A density functional theory for inhomogeneous charged fluids". *Molecular Physics* 40.2 (1980), pp. 413–435.

[234] R. J.F.L. d. Carvalho and R. Evans. "The decay of correlations in ionic fluids". *Molecular Physics* 83.4 (Nov. 1994), pp. 619–654.

[235] P. Attard. "Asymptotic analysis of primitive model electrolytes and the electrical double layer". *Physical Review E* 48.5 (1993), p. 3604.

[236] R. Kjellander and D. J. Mitchell. "Dressed-ion theory for electrolyte solutions: A Debye–Hückel-like reformulation of the exact theory for the primitive model". en. *The Journal of Chemical Physics* 101.1 (July 1994), pp. 603–626.

[237] R. Kjellander and D. J. Mitchell. "An exact but linear and Poisson—Boltzmann-like theory for electrolytes and colloid dispersions in the primitive model". *Chemical physics letters* 200.1-2 (1992), pp. 76–82.

[238] J. Ennis, R. Kjellander, and D. J. Mitchell. "Dressed ion theory for bulk symmetric electrolytes in the restricted primitive model". *The Journal of chemical physics* 102.2 (1995), pp. 975–991.

[239] J. Ulander and R. Kjellander. "The decay of pair correlation functions in ionic fluids: A dressed ion theory analysis of Monte Carlo simulations". en. *The Journal of Chemical Physics* 114.11 (Mar. 2001), pp. 4893–4904.

[240] P Keblinski et al. "Molecular Dynamics study of screening in ionic fluids". *The Journal of Chemical Physics* 113.1 (2000), pp. 282–291.

[241] M. Salanne et al. "Intermediate range chemical ordering of cations in simple molten alkali halides". en. *J. Phys.: Condens. Matter* 20.33 (July 2008), p. 332101.

[242] J. Janeček and R. R. Netz. "Effective screening length and quasiuniversality for the restricted primitive model of an electrolyte solution". *The Journal of chemical physics* 130.7 (2009), p. 074502.

[243] A. A. Kornyshev. *Double-layer in ionic liquids: paradigm change?* 2007.

[244] C. Merlet et al. "The electric double layer has a life of its own". *The Journal of Physical Chemistry C* 118.32 (2014), pp. 18291–18298.

[245] A. Härtel, S. Samin, and R. Van Roij. "Dense ionic fluids confined in planar capacitors: in-and out-of-plane structure from classical density functional theory". *Journal of Physics: Condensed Matter* 28.24 (2016), p. 244007.

[246] M. Girotto et al. "Lattice model of an ionic liquid at an electrified interface". *The Journal of Physical Chemistry B* 121.26 (2017), pp. 6408–6415.

[247] M. A. Gebbie et al. "Ionic liquids behave as dilute electrolyte solutions". en. *Proceedings of the National Academy of Sciences* 110.24 (June 2013), pp. 9674–9679.

[248] S. Perkin et al. "Is a Stern and diffuse layer model appropriate to ionic liquids at surfaces?" en. *PNAS* 110.44 (Oct. 2013), E4121–E4121.

[249] A. M. Smith, A. A. Lee, and S. Perkin. "The electrostatic screening length in concentrated electrolytes increases with concentration". *The journal of physical chemistry letters* 7.12 (2016), pp. 2157–2163.

[250] A. M. Smith, S. Perkin, et al. "Switching the structural force in ionic liquid-solvent mixtures by varying composition". *Physical review letters* 118.9 (2017), p. 096002.

[251] S. W. Coles et al. "Interfacial structure and structural forces in mixtures of ionic liquid with a polar solvent". *Faraday discussions* 206 (2017), pp. 427–442.

[252] A. A. Lee et al. "Scaling Analysis of the Screening Length in Concentrated Electrolytes". en. *Physical Review Letters* 119.2 (July 2017), p. 026002.

[253] N. Hjalmarsson, R. Atkin, and M. W. Rutland. "Switchable long-range double layer force observed in a protic ionic liquid". en. *Chem. Commun.* 53.3 (2017), pp. 647–650.

[254] P. Gaddam and W. Ducker. "Electrostatic Screening Length in Concentrated Salt Solutions". *Langmuir* 35.17 (2019), pp. 5719–5727.

[255] B. Rotenberg, O. Bernard, and J.-P. Hansen. "Underscreening in ionic liquids: a first principles analysis". *Journal of Physics: Condensed Matter* 30.5 (2018), p. 054005.

[256] R. M. Adar et al. "Screening length for finite-size ions in concentrated electrolytes". *Physical Review E* 100.4 (2019), p. 042615.

[257] R. Kjellander. "The intimate relationship between the dielectric response and the decay of intermolecular correlations and surface forces in electrolytes". en. *Soft Matter* 15 (June 2019), pp. 5866–5895.

[258] L. X. Dang. en. *J. Am. Chem. Soc.* 117.26 (July 1995), pp. 6954–6960.

[259] I. Kalcher and J. Dzubiella. "Structure-thermodynamics relation of electrolyte solutions". *J. Chem. Phys.* 130 (2009), p. 134507.

[260] H. J. C. Berendsen, J. R. Grigera, and T. P. Straatsma. en. *The Journal of Physical Chemistry* 91.24 (Nov. 1987), pp. 6269–6271.

[261] M. J. Monteiro et al. *J. Phys. Chem. B* 112.7 (Feb. 2008), pp. 2102–2109.

[262] B. Rotenberg, O. Bernard, and J.-P. Hansen. en. *J. Phys.: Condens. Matter* 30.5 (Jan. 2018), p. 054005.

[263] A. M. Smith, A. A. Lee, and S. Perkin. "Switching the Structural Force in Ionic Liquid-Solvent Mixtures by Varying Composition". *Phys. Rev. Lett.* 118.9 (Mar. 2017), p. 096002.

[264] J. M. Caillol, D. Levesque, and J. J. Weis. "Theoretical calculation of ionic solution properties". *J. Chem. Phys.* 85.11 (Dec. 1986), pp. 6645–6657.

[265] C Schröder et al. "On the collective network of ionic liquid/water mixtures. II. Decomposition and interpretation of dielectric spectra". *The Journal of chemical physics* 129.18 (2008), p. 184501.

[266] K. F. Rinne, S. Gekle, and R. R. Netz. "Dissecting ion-specific dielectric spectra of sodium-halide solutions into solvation water and ionic contributions". *J. Chem. Phys.* 141.21 (Dec. 2014), p. 214502.

[267] A. Elbourne et al. "Nanostructure of the ionic liquid–graphite stern layer". *ACS nano* 9.7 (2015), pp. 7608–7620.

[268] M. Ricci, P. Spijker, and K. Voïtchovsky. "Water-induced correlation between single ions imaged at the solid–liquid interface". *Nature communications* 5.1 (2014), pp. 1–8.

[269] Y. Avni et al. "Charge regulating macro-ions in salt solutions: screening properties and electrostatic interactions". *Soft Matter* 14.29 (2018), pp. 6058–6069.

[270] Y. Avni, D. Andelman, and R. Podgornik. "Charge regulation with fixed and mobile charged macromolecules". *Current Opinion in Electrochemistry* 13 (2019), pp. 70–77.

[271] Y. Avni, R. M. Adar, and D. Andelman. "Charge oscillations in ionic liquids: A microscopic cluster model". *Physical Review E* 101.1 (2020), p. 010601.

[272] D. Borgis et al. "Computation of pair distribution functions and three-dimensional densities with a reduced variance principle". *Molecular Physics* 111.22-23 (2013), pp. 3486–3492.

[273] S. W. Coles et al. "Computing three-dimensional densities from force densities improves statistical efficiency". *The Journal of Chemical Physics* 151.6 (2019), p. 064124.

[274] S. Schön and R. von Klitzing. "A simple extension of the commonly used fitting equation for oscillatory structural forces in case of silica nanoparticle suspensions". *Beilstein Journal of Nanotechnology* 9.1 (2018), pp. 1095–1107.

[275] A. A. Lee et al. "Casimir force in dense confined electrolytes". en. *Molecular Physics* 116.21-22 (Nov. 2018), pp. 3147–3153.

[276] X. Yu et al. "Direct Observation of the Redistribution of Sulfur and Polysulfides in Li–S Batteries During the First Cycle by In Situ X-Ray Fluorescence Microscopy". *Advanced Energy Materials* 5.16 (2015), p. 1500072.

[277] J. R. Akridge, Y. V. Mikhaylik, and N. White. "Li/S fundamental chemistry and application to high-performance rechargeable batteries". *Solid state ionics* 175.1-4 (2004), pp. 243–245.

[278] S. Xin et al. "Smaller sulfur molecules promise better lithium–sulfur batteries". *Journal of the American Chemical Society* 134.45 (2012), pp. 18510–18513.

[279] X. Yao et al. "High-Performance All-Solid-State Lithium–Sulfur Batteries Enabled by Amorphous Sulfur-Coated Reduced Graphene Oxide Cathodes". *Advanced Energy Materials* 7.17 (2017), p. 1602923.

[280] T.-Z. Hou et al. "Design principles for heteroatom-doped nanocarbon to achieve strong anchoring of polysulfides for lithium–sulfur batteries". *Small* 12.24 (2016), pp. 3283–3291.

[281] W. Li et al. "Understanding the role of different conductive polymers in improving the nanostructured sulfur cathode performance". *Nano letters* 13.11 (2013), pp. 5534–5540.

[282] Z. W. Seh et al. "Sulphur–TiO_2 yolk–shell nanoarchitecture with internal void space for long-cycle lithium–sulphur batteries". *Nature communications* 4 (2013), p. 1331.

[283] Z. Yuan et al. "Powering lithium–sulfur battery performance by propelling polysulfide redox at sulfiphilic hosts". *Nano letters* 16.1 (2016), pp. 519–527.

[284] C.-W. Lee et al. "Directing the lithium–sulfur reaction pathway via sparingly solvating electrolytes for high energy density batteries". *ACS Cent. Sci.* 3.6 (2017), pp. 605–613.

[285] L. Cheng et al. "Sparingly solvating electrolytes for high energy density lithium–sulfur batteries". *ACS Energy Letters* 1.3 (2016), pp. 503–509.

[286] H. Chu et al. "Unraveling the Dual Functionality of High-Donor-Number Anion in Lean-Electrolyte Lithium-Sulfur Batteries". *Advanced Energy Materials* (), p. 2000493.

[287] H. Chu et al. "Achieving three-dimensional lithium sulfide growth in lithium-sulfur batteries using high-donor-number anions". *Nature communications* 10.1 (2019), pp. 1–12.

[288] H. Farber and S. Petrucci. "Kinetics of complexation of 18-crown-6 ether with lithium perchlorate in solvents of low permittivity. 1, 3-Dioxolane and 1, 2-dimethoxyethane". *J. Phys. Chem.* 85.10 (1981), pp. 1396–1401.

[289] J. Chandrasekhar, D. C. Spellmeyer, and W. L. Jorgensen. "Energy component analysis for dilute aqueous solutions of lithium (1+), sodium (1+), fluoride (1-), and chloride (1-) ions". *J. Am. Chem. Soc* 106.4 (1984), pp. 903–910.

[290] D. Horinek, S. I. Mamatkulov, and R. R. Netz. "Rational design of ion force fields based on thermodynamic solvation properties". *J. Chem. Phys.* 130.12 (2009), p. 124507.

[291] J. Wang et al. "Development and testing of a general amber force field". *J. Comput. Chem.* 25.9 (2004), pp. 1157–1174.

[292] D. Van Der Spoel et al. "GROMACS: fast, flexible, and free". *Journal of computational chemistry* 26.16 (2005), pp. 1701–1718.

[293] L. Martínez et al. "PACKMOL: a package for building initial configurations for molecular dynamics simulations". *J. Comput. Chem.* 30.13 (2009), pp. 2157–2164.

[294] B. Hess et al. "LINCS: A Linear Constraint Solver for Molecular Simulations". *J. Comput. Chem.* 18.12 (1997), pp. 1463–1472.

[295] L. L. Missoni et al. "A LiMn2O4-polypyrrole system for the extraction of LiCl from natural brine". *Journal of The Electrochemical Society* 163.9 (2016), A1898–A1902.

[296] C. H. Giammanco, P. L. Kramer, and M. D. Fayer. "Ionic Liquid versus Li+ Aqueous Solutions: Water Dynamics near Bistriflimide Anions". *The Journal of Physical Chemistry B* 120.37 (2016), pp. 9997–10009.

Acknowledgements

I would first like to thank my supervisor Prof. Dr. Joachim Dzubiella, who has influenced my professional and personal life. As I had very little experience with simulation at the beginning, his patience and guidance had motivated me to push my abilities and scientific goals. His critical ideas, insight and enthusiasm for research have stimulated me to tackle the scientific challenges. I am fortunate enough to have his great support and guidance.

I would like to thank my adviser, Dr. Matej Kanduč for his guidance and advises. His critical insight and suggestions have consolidated my skills and scientific knowledge. He made time for me to discuss my research, whenever I had questions about our projects. With his advises, I could develop my research.

I would like to thank Dr. Wonkyu Kim for his advises and supports. Whenever I had difficulties concerning my research, presentations or personal issues, he was willing to discuss with me. His caring and advises helped me to go through my time at HZB.

I would like to thank Prof. Dr. Matthias Ballauff, Prof. Dr. Benjamin Rotenberg, Prof. Dr. Yan Lu, Prof. Dr. Mathieu Salanne, Dr. Michaël Deschamps, Prof. Dr. Annie Colin, Dr. Sebastian Risse, Dr. Sebastien Groh, Dr. Alexis Grimaud, Dr. Victor Ruiz, Dr. Samuel W. Coles, Dr. Zhujie Li, Richard Chudoba, Rohit Nikam, Arne Ronneburg, Nicolas Dubouis and Soufiane Abdelghani-Idrissi. I was grateful to have the opportunity to work and discuss fruitful project discussions.

I would like to thank Dr. Matej Kanduč, Dr. Karol Palczynski and Dr. Kek Boon Goh who helped me proofread and whose guidance helped to improve this thesis.

The time I sent at the Wannsee campus could not have been more enjoyable without my officemates, Sebastian Milster, Yi-chen Lin, Mila Miletic, Holger-Dietrich Saßnick and Yannik Schütze.

Finally, I would like to express my deep gratitude and love to Jungsook, Jane and my parents. I owe them all an immense debt of their love, care and patience. Sincerely

thank you.

Declaration of Independent work

I declare that I have completed the thesis independently using only the aids and tools specified. I have not applied for a doctor's degree in the doctoral subject elsewhere and do not hold a corresponding doctor's degree. I have taken due note of the Faculty of Mathematics and Natural Sciences PhD Regulations, published in the Official Gazette of Humboldt-Universität zu Berlin no. 126/2014 on 18/11/2014.

Potsdam, 10 June 2020

.....

Chanbum Park